CLAS ANALYSIS NOTE 2007-XXX
Version 2.0 July 30, 2008

Analysis of $\pi^+\pi^-$ production from the g11 data set.

M. Battaglieri[a], R. De Vita[a]
L. Bibrzycki[b],L. Lesniak[b]
A. Szczepaniak[c]

[a] Istituto Nazionale di Fisica Nucleare, Genova - Italy
[b] H. Niewodniczanski Institute of Nuclear Physics PAN, Krakow - Poland
[c] Physics Department and Nuclear Theory Center, Indiana University, Bloomington - Indiana

Abstract :

We performed a complete partial wave analysis of the reaction $\gamma p \to p\pi^+\pi^-$ in the range 3.0 GeV $< E_\gamma <$ 3.8GeV and momentum transfer 0.4 GeV^2 $< -t <$1.0 GeV^2 using the $g11$ data set. As a check of the data quality and photon flux normalization, a *standard* analysis, similar to the procedure used to analyze $g6$ data set, was performed deriving the differential cross section $d\sigma/dt$for the reaction $\gamma p \to p\rho^0$. The partial wave analysis was performed in different ways in order to evaluate the systematic of the procedure and the effect of the approximations. Again, to check the PWA results, the cross section for the dominant channel $\gamma p \to p\rho^0$ was extracted and found to be in good agreement with the results of the *standard* analysis. As a final result, moments of the di-pion angular distributions and differential cross sections for S, P, and D wave were derived. In particular, in the S-wave, we found a clear evidence of the $f_0(980)$ scalar meson. This is the first time this resonance has been measured in a photoproduction experiment.

Introduction

Photo-production has only recently become a powerful tool in investigations of meson spectroscopy. Most of our knowledge on the light quark meson spectrum comes from hadron induced reactions, using typically π, K, p or $\bar{p}$ beams. In contrast there have been very few comprehensive programs exploring photo-production. The typical data sets from existing photo-production experiments in the energy range below 20 GeV (typical for meson spectroscopy experiments) have tens of thousands of events and only a few topologies have been studied [1, 2, 3] . In contrast the data samples from the $g11$ run, in many channels exceed the existing sets by at least an order of magnitude and with several reconstructed topologies enable a comprehensive study.
This study will focus on:

- photo-production mechanisms of some well established resonances, ρ, $f_2(1270)$ and extraction of photo-couplings of resonances,
- measurements of cross-sections of less known states like the $f_0(980)$,
- study of non-resonant, coherent production of meson pairs with emphasis on threshold production.
- understanding of partial wave analysis in presence of both baryon and meson resonances.

This analysis is part of a wider program that includes other two-meson topologies as $K\bar{K}$ and $\pi^0\pi$ in the final state.
The theoreical analysis will follow closely that of [5, 6].
At center of mass energies $\sqrt{s} <$ few GeV, which are still large compared to other invariants, in particular to the momentum transfered to the target, according to Regge theory, the hadronic production amplitudes factorize into amplitude for meson production off a reggion and an amplitude for the reggion coupled to the nucleon [4]. In quasi-elastic production Regge theory can be used to provide the mechanism of both resonance production and for the production of coherent backgrounds. Resonance parameters will then be extracted and compared with lattice computations or used to test models of QCD.

Photo-production opens a new window in this respect. On one side it is complementary to hadro-production. Through VMD photon can be decomposed into a sum over vector mesons. This seems to saturate rapidly thus can be described in terms of regge amplitudes for vector meson nucleon scattering. On the other side quark-hadron duality and the point-like-nature of the photon coupling makes it possible to describe photo-hadron interactions at the QCD level. For example, radiative decays of resonances, which directly probe the QCD structure of hadrons may be accessible through photo-production, provided the resonance production mechanisms can be isolated from coherent backgrounds. Extraction of resonance parameters from the data thus requires amplitude analysis and understanding of background processes. Even though CLAS is not ideal for these type of analysis due to a limited acceptance in the forward direction and the available energy sets a rather low upper limit of photon energy, high statistics, availability of several channels and spread in photon energy, may enable to verify the applicability of regge parametrizations, and thus provide a viable model for the background and direct resonance production.

Photo-production can also access a different part of meson spectrum as compared with reactions initiated by hadron beams. This is related to the helicity structure of the photon-quark interactions and the point-like nature of the photon and can be studied via partial wave analysis. It is also qute possible that resonances suppressed in photo-production could be easier accessed in photo-production. For example photo-production of $K\bar{K}$ pairs near threshold is dominated by the ϕ meson. Interference of the ϕ decay products and with the coherently produced scalar waves can be used to investigate scalar resonances and in particular the enigmatic, $f_0(980)$ [5].

The properties of the $f_0(980)$ depend crucially on the low-energy meson-meson interactions that test effective chiral theories [7] .

In this note we report about $\pi^+\pi^-$ production, focusing on the production of low spin partial waves to investigate production mechanisms of the σ, ρ, $f_0(980)$ and $f_2(1270)$. This is the first step of a coupled channel analysis which involves all relevant decay channels.

Contents

Chapter 1

Data analysis

In this section we will briefly show the main features of the data, the systematic controls of their quality and reliability and the cuts used to identify the particles and the channel.

To identify the channel $\gamma p \rightarrow p\pi^+\pi^-$ two different final state topologies were analyzed: 1) $p\pi^+$ detected and π^- not detected; 2) $p\pi^+\pi^-$ detected. Due to the different correlation between the produced particles and the different CLAS efficiencies, each topology mainly covers different kinematical regions.

The final state was selected identifying two (three) charged particles and reconstructing the π^- (no other particles) by missing mass technique. The peaks of identified particles and known background states were selected (or cut) fitting the peaks and applying a 3σ cut. This analysis was performed using the whole $g11$ data set covering the energy range from 3.0 GeV up to 3.8 GeV corresponding to a total integrated luminosity of ~ 18 pb^{-1}. If not explicitely said, figures refer to the whole statistics.

1.1 General cuts

For both topologies the main steps of the analysis are the following: particle identification(p, π^+, π^-); channel identification with missing mass technique.
Data were corrected for energy loss (standard *Eloss* package with updated $g11$ geometry), tagger and CLAS momentum distortions (derived from the kinematic fitting procedure of $g11$ data as described in [39]). The experimental masses for known hadrons after correction, are reported in Appendix A compared to the PDG values: a maximum discrepancy of 1.5 MeV was observed.

1.2 Particle and channel identification of $\gamma p \rightarrow p\pi^+(\pi^-)$

For this topology, we selected events with 2 charged particles in the final state. The standard SEB particle ID was used to identify p and π^+. Left panel of Fig. 1.1 shows (β vs. *momentum*) for protons and pions. All particles identified by SEB were retained in the analysis. We identified the π^- looking at the missing mass of the ($p\pi^+$) system. The right panel in Fig. 1.1 shows the π^- peak on a small background we did not subtract. A simple cut of ± 0.06 GeV^2 around the reconstructed squared mass of 0.019 GeV^2 was applied to identify the missing pion.

1.3 Particle and channel identification of $\gamma p \rightarrow p\pi^+\pi^-$

For this topology, we selected events with 3 charged particles in the final state. The standard SEB particle ID was used to identify p and π^+ and π^-. The left panel in Fig. 1.2 shows (β vs. *momentum*) for proton and pions. The right panel in Fig. 1.2 shows the missing mass of the

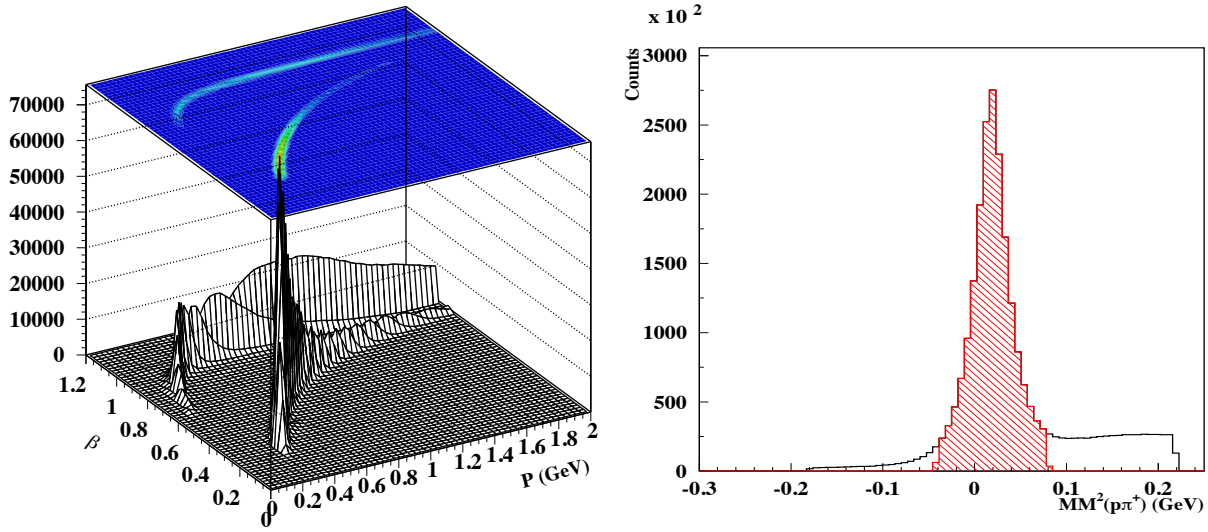

Figure 1.1: $p\pi^+(\pi^-)$ topology. The left panel shows the proton and pion lines in the β versus p plane. The right panel shows the missing π^- mass (the hatched area corresponds to the reteined events). Only 4% of the whale statistics is shown.

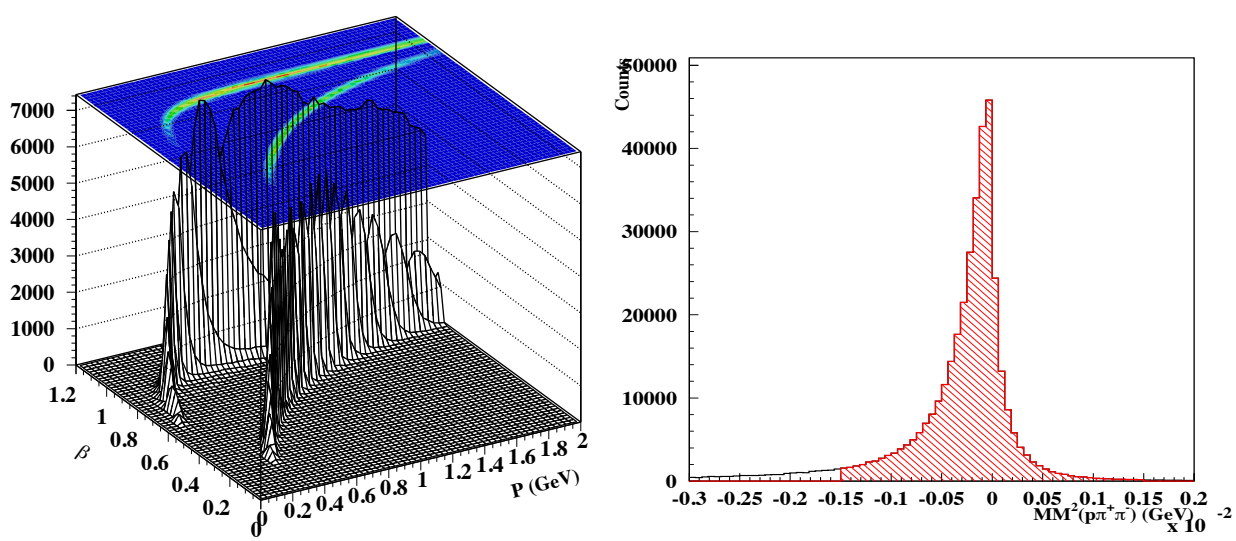

Figure 1.2: $p\pi^+\pi^-$ topology. The left panel shows the proton and pion lines in the β versus p plane. The right panel shows the missing mass of the system $(p\pi^+\pi^-)$ (hatched area correspond to the reteined events). Only 4% of the whale statistics is shown.

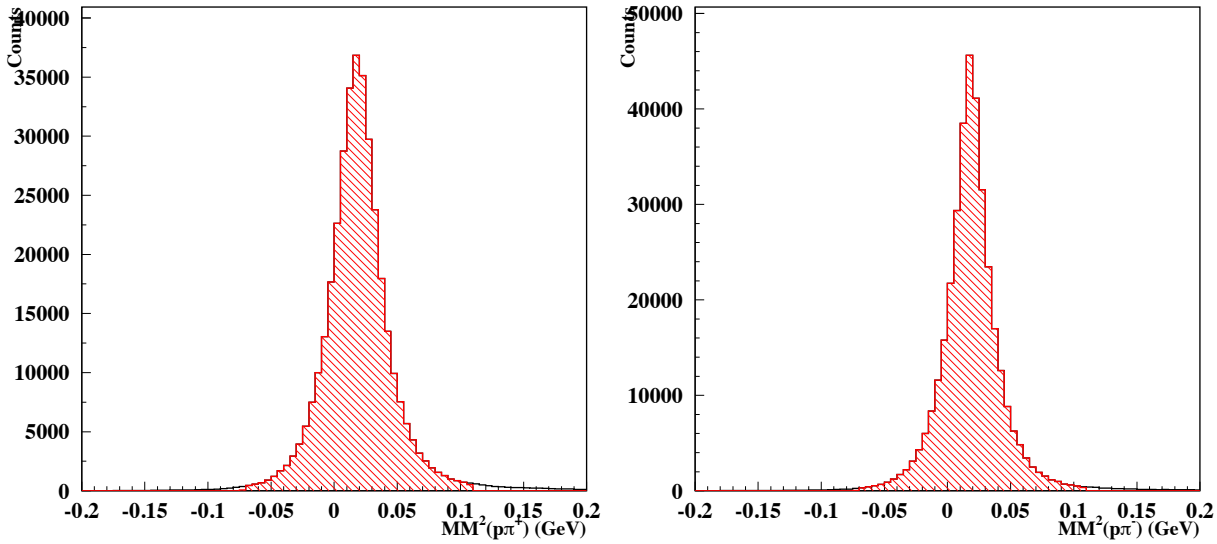

Figure 1.3: $p\pi^+\pi^-$ topology. The left panel shows the reconstructed π^- mass (hatched area correspond to the reteined events) derived from the measured $(p\pi^+)$ system. The right panel shows the same for the π^+. Only 4% of the whale statistics is shown.

system $(p\pi^+\pi^-)$ when all the three particles are detected. A cut of ± 0.0015 GeV^2 around the squared missing mass was applied to identify the 2π final state. A loose cut (± 0.09 GeV^2 around the reconstructed squared mass of 0.019 GeV^2) was also applied to the reconstructed π^- (π^+) mass derived from the measured $p\pi^+$ $(p\pi^-)$ system. Figure 1.3 shows the two MM$(p\pi)$ spectra before and after the cut. Since all three particles were detected, the multi-pion background is almost absent.

1.4 Fiducial cuts

In this analysis we applied fiducial cuts on minimum hadron momenta and minimum and maximum hadron angles. DC holes and bad TOF paddles were removed at cooking level and in GPP. Fiducial cuts were derived from the comparison of the Single Particle Acceptance (SPE's) derived from the real data and from the Monte Carlo Simulations. More details on SPEs are reported in Par. 2.1.3.
Here is the detailed list of cuts applied (all variables are in the Lab system).

Proton:

- $p > 0.32$ GeV: cut on minimum proton momentum;
- $\theta > 10°$: cut on minimum proton angle;
- $NOT(p < 0.45$ GeV AND $\theta < 35°)$: this cut removes a specific kinematic region where the discrepancy between SPE from data and MC was more than 10%.

π^+:

- $p > 0.125$ GeV: cut on minimum proton momentum;
- $\theta > 10°$ AND $\theta < 120°$: cut on minimum and maximum π^+ angles;

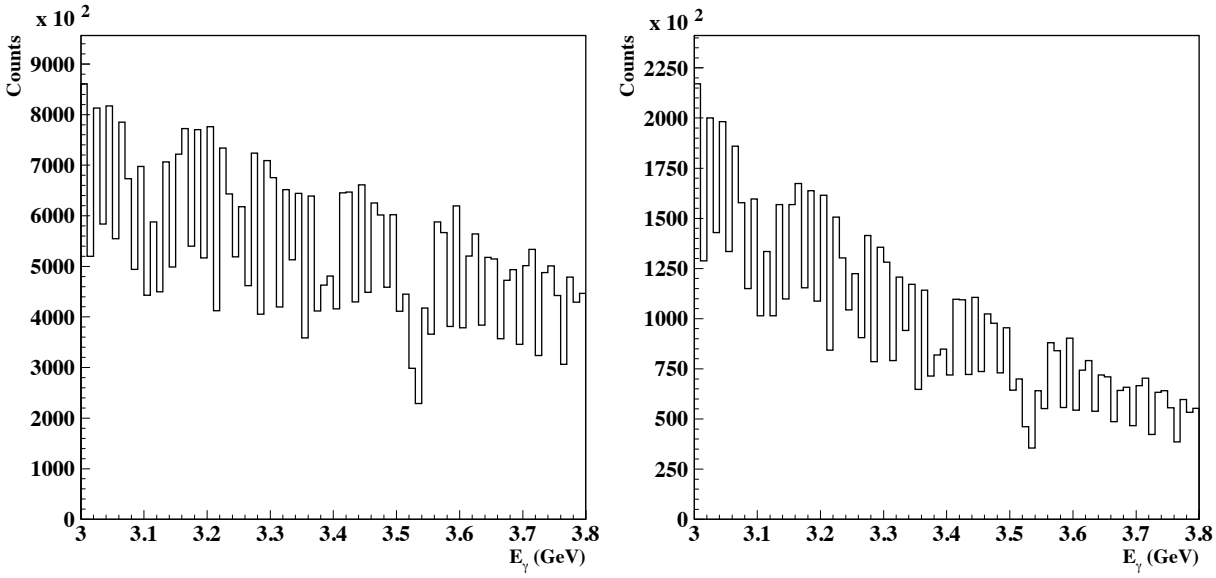

Figure 1.4: Photon energy spectrum after the selection. Left, $p\pi^+(\pi^-)$ topology; right, $p\pi^+\pi^-$ topology.

- SEC1: $\theta < 90°$, SEC3: $\theta < 70°$, SEC5: $\theta < 80°$: specific sector dependent cuts.

π^-:

- $p > 0.125$ GeV: cut on minimum proton momentum;
- $\theta > 10°$ AND $\theta < 120°$: cut on minimum and maximum π^- angles;
- SEC1: $\theta < 100°$, SEC3: $\theta < 90°$, SEC5: $\theta < 90°$, SEC6: $\theta < 110°$: specific sector dependent cuts.

After applying all cuts yields reduce from 46M to 41M events and from 8.5M to 7.5M events for the first and second topoly respectively. Fiducial cuts were applyied to data and MC simulations. In this way the corresponding efficiency takes into account the different conditions compensating for possible holes or bad detector regions. The same set of cuts was used to extract different known cross sections involving different particles and their combination. More details are reported in dedicated notes [40, 41].

1.5 Photon flux normalization and multiple hits correction

For this analysis only the highest part of the photon energy spectrum was used ranging from 3.0 GeV to 3.8 GeV. Figure 1.4 shows the photon energy spectrum after all cuts described above were applied.

To be able to extract an absolute cross section, some cuts were applied from the very beginning. These mainly deal with the proper identification of the incident photon and with the photon flux normalization. We required one and only one photon present in the tagger within a certain time window between CLAS and the tagger itself. The window was chosen to be $\pm$ 2 ns after checking the consistency of the cross sections extracted from the $g11$ data sample with the world data [40]. We also excluded from the analysis all the events associated to beam trips [1]. These

[1] The photon normalization code, GFLUX, evaluates the number of incoming photons only for the time intervals, defined by subsequent scaler events, when the beam intensity and DAQ rate were stable. All events that do not belong to such "good" time intervals are marked as bad and should not be used in the analysis if the final goal is the extraction of an absolute cross section. The beam trip information is stored in dedicated text files available on the silo in */mss/clas/g11a/production/pass1/v1/trip*.

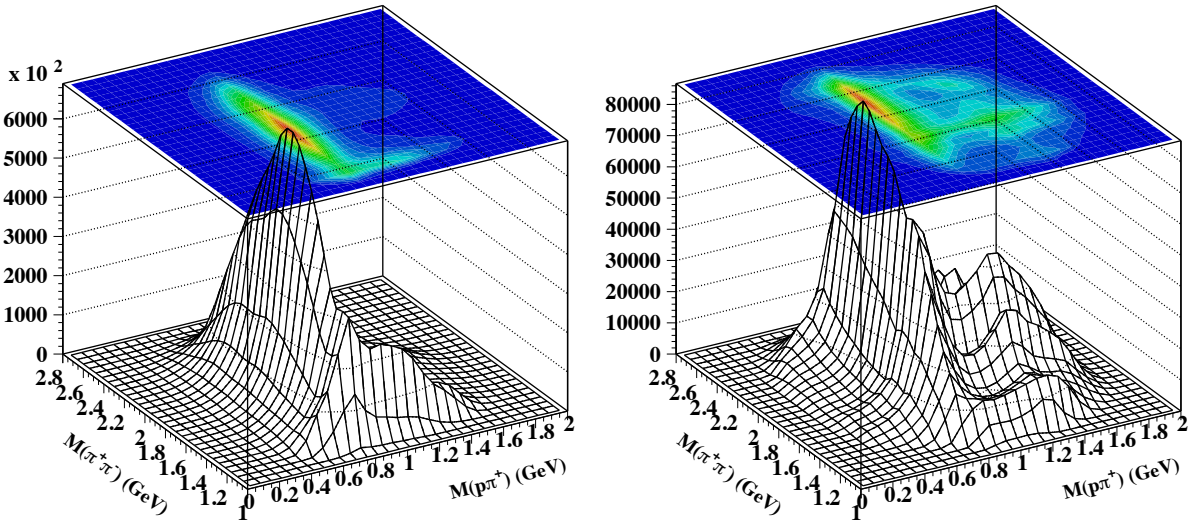

Figure 1.5: Bidimensional plot of $(\pi^+\pi^-)$ invariant mass versus $(p\pi^+)$ invariant mass. Left, $p\pi^+(\pi^-)$ topology; right, $p\pi^+\pi^-$ topology.

cuts reduce the data sample by ∼10-15%.

1.6 Other corrections

Detailed studies performed by the $g11$ run group and independently by the CMU group derived some corrections that have to be applied to the raw yilds in order to obtain the cross sections. More details are reported in dedicated Notes [47, 48]; below we summarize the correction factors used in this analysis.

- Time window correction: 1.06;
- Multiple hit cut correction: ∼1.15 (calculated and applied for each E-counter);
- Current dependent correction cut: 1.187;
- Trigger inneficiency (topology 1 only): 1.15

All values reported above multiply the raw yields.

1.7 Cuts summary

The applied cuts are summarized below.

General:

- $|TAG_{time} - ST_{time}| < 2$ ns: usual timing cut;
- $|N_{photon\ in\ time}| = 1$, to reject multiple hits;
- $TRIG\_CLAS$ =0, to cut events taken during beam trips;
- the *proton*, as identified by SEB, is always required.

- 3.0 GeV $< E_\gamma <$ 3.8 GeV;

Particle and channel id: $p\pi^+(\pi^-)$ topology 1

- N_{π^+}=1, N_{π^-}=0; only one positive pion detected;
- $|MissingMass^2_{(p\pi^+)} - 0.019|$ <0.06 GeV^2: π^- missing mass.

Particle and channel id: $p\pi^+\pi^-$ topology 2

- N_{π^+}=1, N_{π^-}=1; exactly one positive and one negative pion detected;
- $|MissingMass^2_{(p\pi^+)} - 0.019|$ <0.09 GeV^2: consistent π^- missing mass;
- $|MissingMass^2_{(p\pi^-)} - 0.019|$ <0.09 GeV^2: consistent π^+ missing mass;
- $|MissingMass^2_{(p\pi^+\pi^-)}|$ <0.0015 GeV^2: no other particle in the final state.

After all cuts the two data samples have a total of ∼41M and ∼7.5M events respectively. Figure 1.5 shows the bidimension plot of $(\pi^+\pi^-)$ $(p\pi^+)$ invariant masses for the two topologies. The unidimensional projections, $(\pi^+\pi^-)$, $(p\pi^+)$ and $(p\pi^-)$, are shown in fig. 1.6. The $(\pi^+\pi^-)$ angular distribution in the center of mass system, as well as the $-t$ distribution for the two topologies is shown in fig. 1.7. While the first shows an acceptance cut around $-t \sim 0.1$ GeV^2, the second is clearly deforemed by the CLAS acceptance up to $-t \sim 0.5 - 0.6$ GeV^2. Since for this study we are interested in the low $-t$ kinematic domain, only the first topology will be further analyzed.

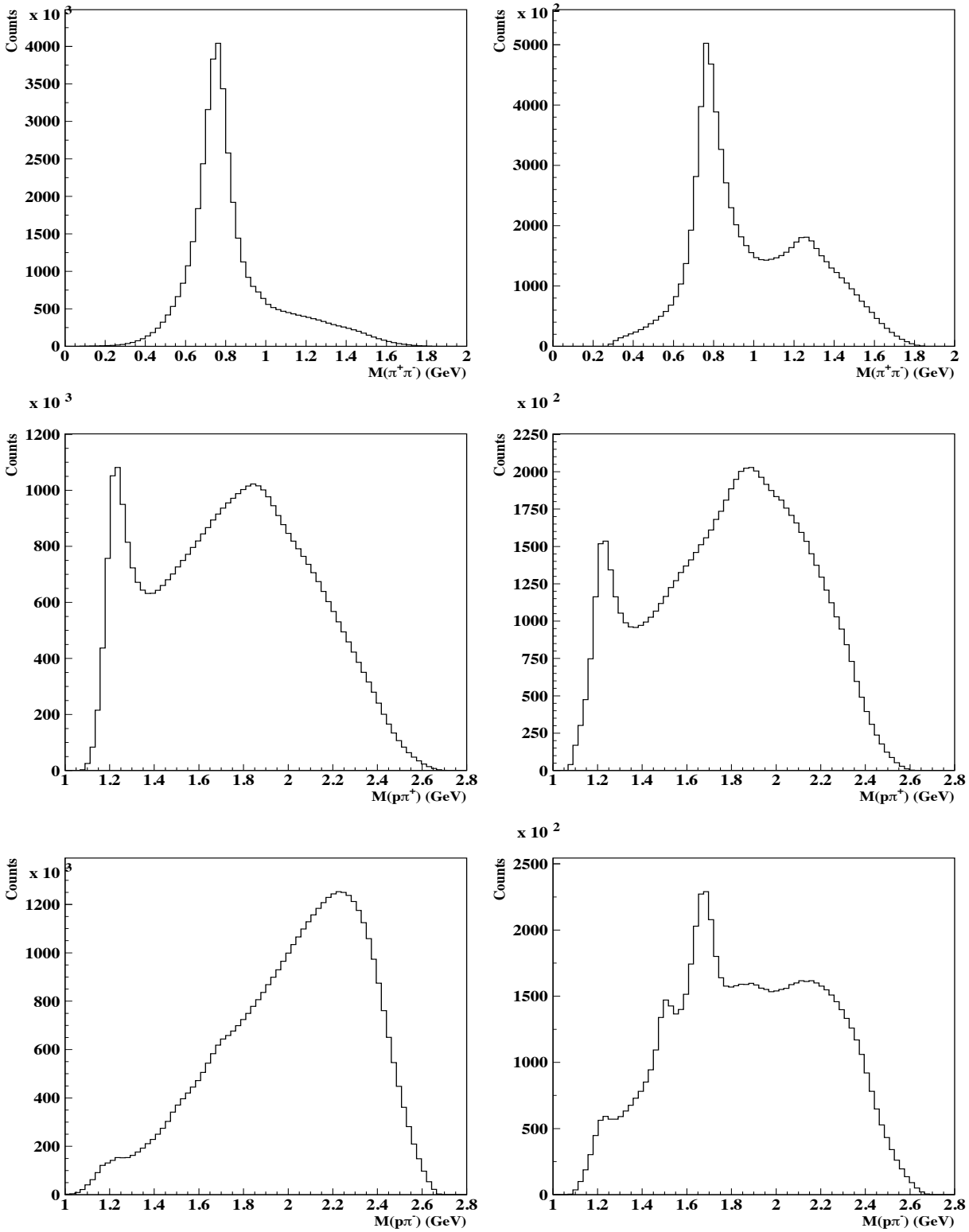

Figure 1.6: Invariant masses obtained from the two topologies: left $p\pi^+(\pi^-)$; right $p\pi^+\pi^-$.

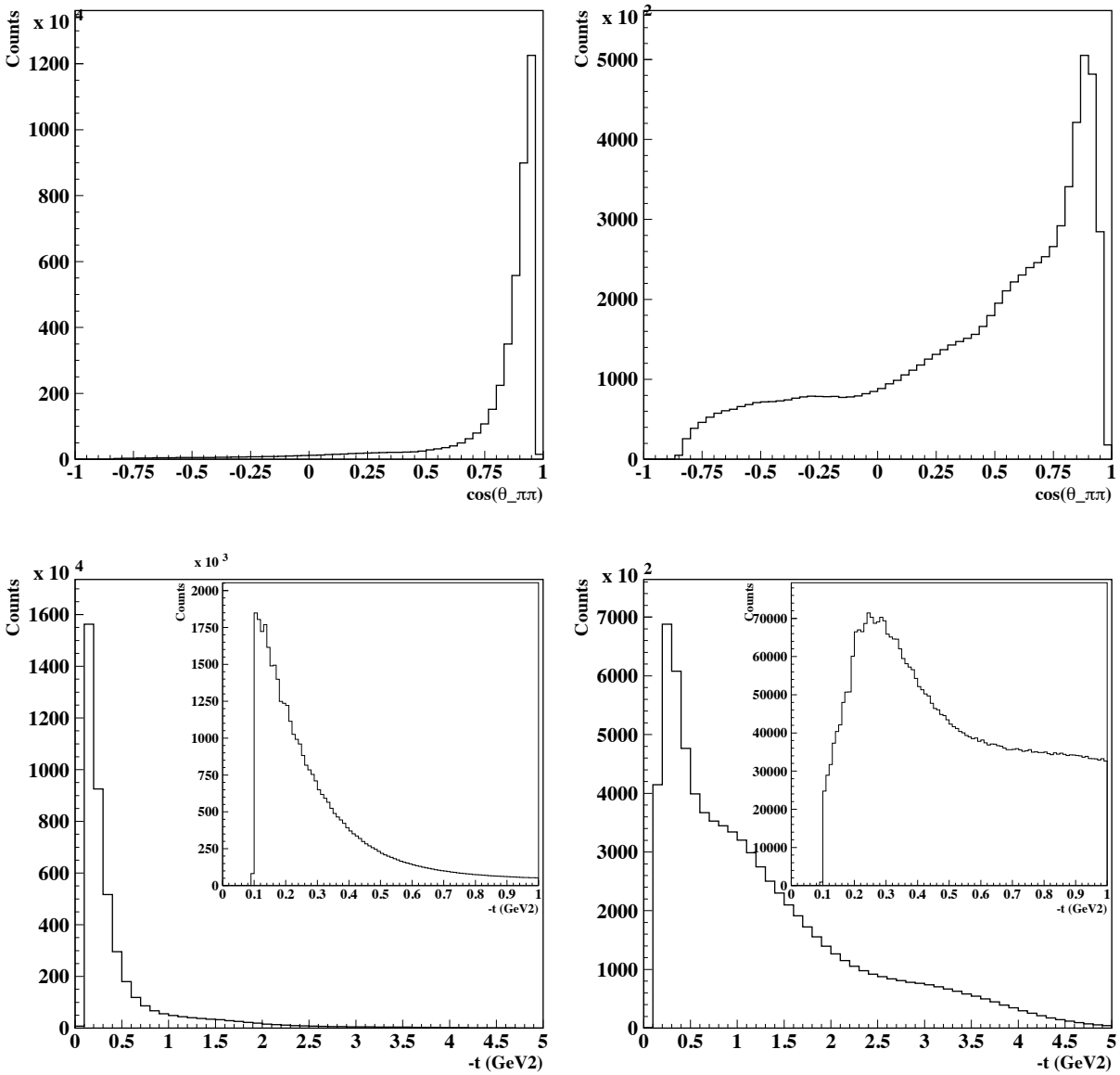

Figure 1.7: Upper panel: $\cos\theta^{CM}_{\pi^+\pi^-}$ distribution in the center of mass system. Lower panel: $-t$ distribution zooming in the $-t < 1$ GeV^2 region (insert). Left, $p\pi^+(\pi^-)$ topology; right, $p\pi^+\pi^-$ topology.

Chapter 2

The $\gamma p \to p\pi^+\pi^-$ and the $\gamma p \to p\rho^0$ cross section: standard analysis

In this Chapter we described procedure to derive the $\gamma p \to p\pi^+\pi^-$ total cross section and the $\gamma p \to p\rho^0$ differential cross section. This analysis is similar to what performed on CLAS $g6a$ data set CLAS pubblished in ref. **??** and ref. **??**. The main difference is that here we only derive an integrated CLAS efficiency (no binning in the 5-dimension phase space) using a realistic event generator for the reaction $\gamma p \to p\pi^+\pi^-$. Therefore the derived cross sections may still have a weak model-dependence. Since the main goal of this analysis is to perform the partial wave analysis on the $\pi^+\pi^-$ system (see next Chapter), the cross section deirved here are intended as a check of the data quality and systematics.

2.1 Monte Carlo simulations

2.1.1 The event generator

To evaluate the CLAS efficiency we used a realistic event generator [Co94]. Since the missing mass cuts (for each detected topology) keeps the contamination of more-than-two-pions production at some % level simulations only include reactions with the $p\pi^+\pi^-$ final state. The channels included in the simulation were: $\gamma p \to p\rho$, $\gamma p \to \Delta^{++}\pi^-$, $\gamma p \to \Delta^0\pi^+$, $\gamma p \to pf_2(1225)$ and $\gamma p \to p\pi^+\pi^-$ (phase space). Each channel was weighted by the relative total cross sections in the energy range of the experiment (62%, 10%, 4% 20% and 4% respectively) The code interpolates the available measured angular distributions (production and deacy) for ρ, Δ's and $f_2(1225)$ while the phase space was assumed to have a 3-body uniform distribution in the hadronic center of mass system. Fig. 2.1 shows the generated distributions of: E_γ, $-(t - t_{min})$ and $\cos\theta^{CM}_{\pi^+\pi^-}$ in the energy range $3 - 3.8$ GeV. Fig. 2.2 shows the reconstructed $(\pi^+\pi^-)$ invariant mass spectra as obteined from the $p\pi^+(\pi^-)$ and $p\pi^+\pi^-$ topologies. The event vertex was extracted uniformly over a realistic long target, z in the range (-30:+10) cm, with x and y in a 0.5 cm radius corresponding to the photon beam spot. The generated events were processed by the code simulating CLAS (GSIM), post processed using GPP and reconstructed using the same version of reconstruction code (RECSIS) used to reconstruct the real data. In this way the geometrical acceptance of CLAS as well as the hardware/software efficiency should be taken into account. The same set of cuts was applied to the simulated data (missing mass, minimum momentum cut, fiducial cuts) in order to have a realistic estimation of the overall efficiency of the whole analysis procedure.

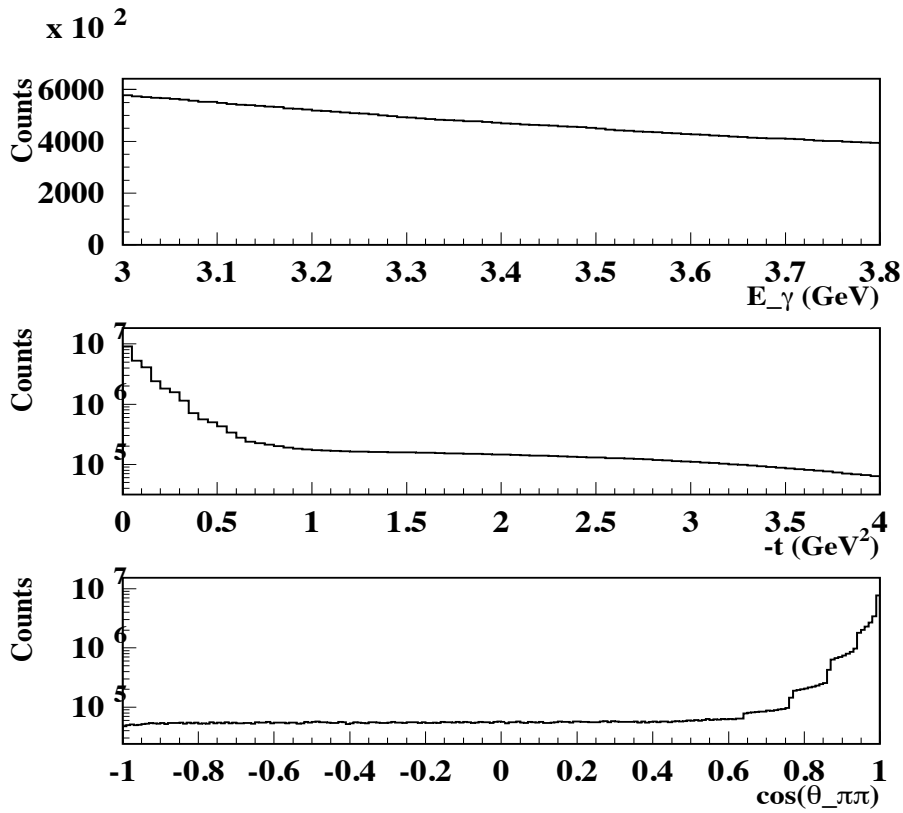

Figure 2.1: MC generated events: E_γ (top), $-(t - t_{min})$ (middle), and $\cos\theta^{CM}_{\pi^+\pi^-}$ (bottom) distributions.

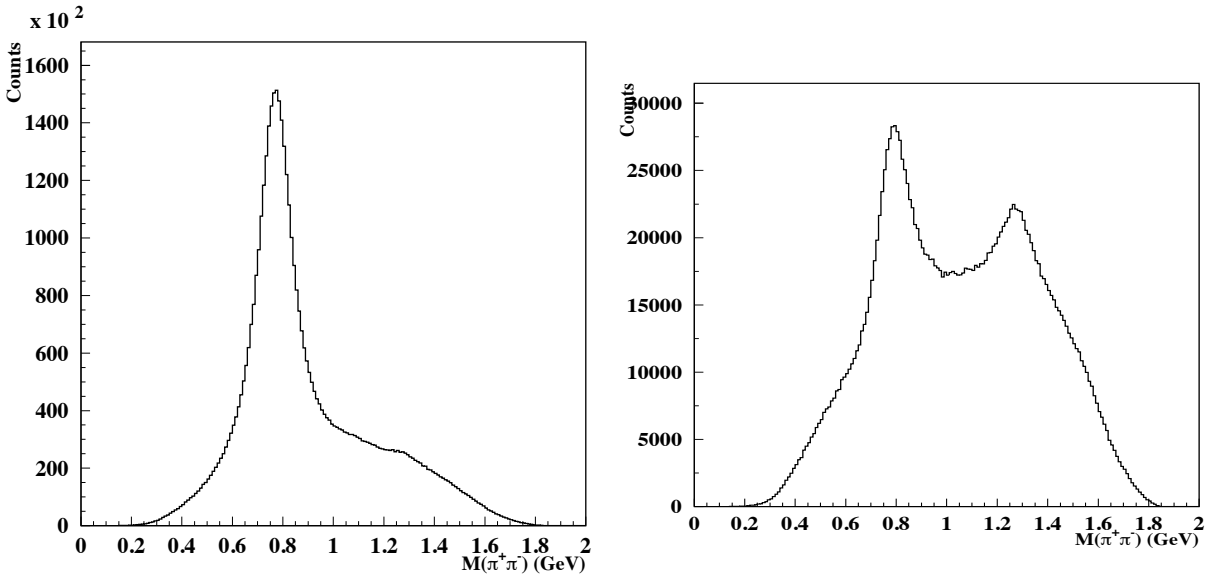

Figure 2.2: MC reconstructed events: $(\pi^+\pi^-)$ invariant mass spectra as obteined from the $p\pi^+(\pi^-)$ (left) and $p\pi^+\pi^-$ (right) topologies.

Variable	Range	N bins
E_γ	3.0:3.8 GeV	4
$M_{\pi^+\pi^-}$	0:2.0 GeV	40
$-t$ ($\cos\theta^{CM}_{\pi^+\pi^-}$)	0-1.0 GeV (-1.0:1.0)	20 (30)

Table 2.1:

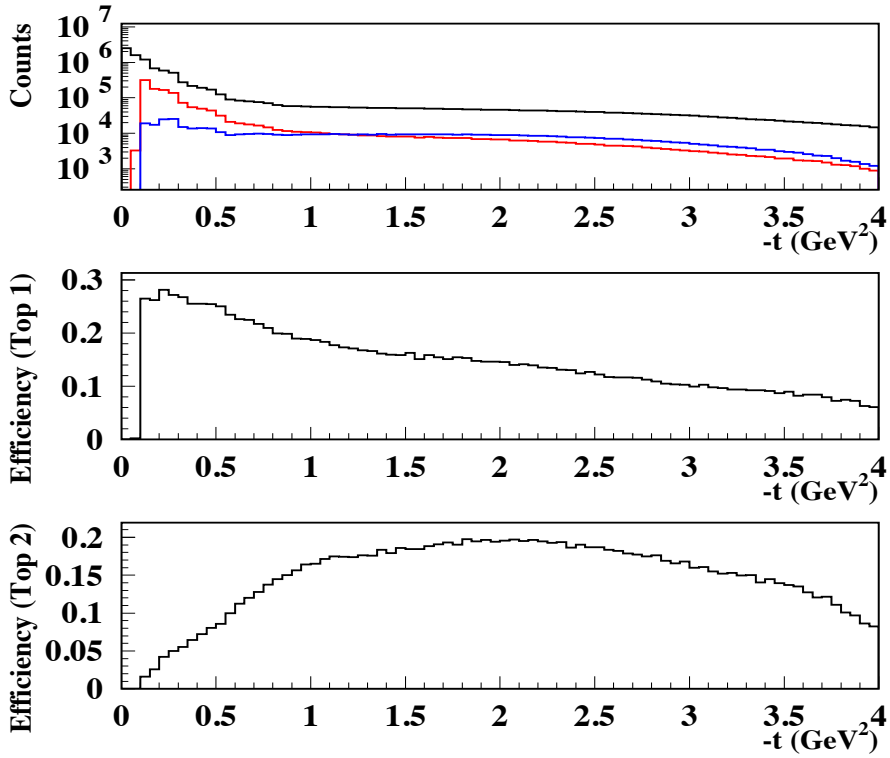

Figure 2.3: CLAS efficiency as a function of $-t$. Top: generated (black), reconstructed $p\pi^+(\pi^-)$ (red) and reconstructed $p\pi^+\pi^-$ (blue) events.The corresponding efficiency for $p\pi^+(\pi^-)$ (middle) and $p\pi^+\pi^-$ (bottom) topologies.

2.1.2 The CLAS efficiency using GSIM

The efficincy was defined in the standard way:

$$CLAS \quad Efficiency = \epsilon = \frac{N_{Reconstructed}}{N_{Generated}} \tag{2.1}$$

To minimise the model dependency, all data (both generated and reconstructed) were binned in 3 independent kinematical variables: E_γ, $(\pi^+\pi^-)$ invariant mass, and $-t$ (or $\cos\theta^{CM}_{\pi^+\pi^-}$). The number of bin for each variable was chosen to be compatible with CLAS resolution and sensitive to the efficiency variations. Tab. 2.1.2 shows the binning and the range of each variable. A total of 38M events were generated.

Fig. 2.3 shows the $-t$ generated and reconstructed distributions and the corresponding efficiency for the two topologies in the first energy bin (3.0 - 3.2 GeV). The same as a function of $\cos\theta^{CM}_{\pi^+\pi^-}$, is shown in fig. 2.4. Since the topology with all trhee hadrons detected shows a detection efficincy one order of magnitude smaller in the forward region ($0< -t < 1$ GeV^2) where the most part of the total cross section is concentred and where the interest of this analysis is focused, what follows is only derived from the first topology ($p\pi^+$ detected).

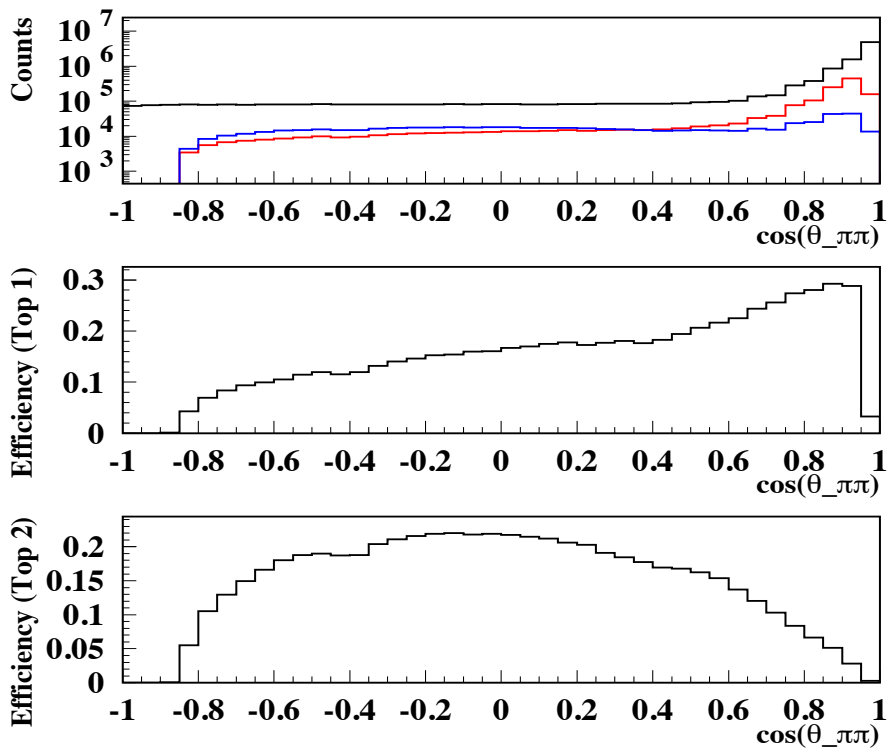

Figure 2.4: CLAS efficiency as a function of $\cos\theta^{CM}_{\pi^+\pi^-}$. Top: generated (black), reconstructed $p\pi^+(\pi^-)$ (red) and reconstructed $p\pi^+\pi^-$ (blue) events.The corresponding efficiency for $p\pi^+(\pi^-)$ (middle) and $p\pi^+\pi^-$ (bottom) topologies.

2.1.3 Single particle efficiency

To check the reliability of the CLAS simulation (GSIM), a second procedure to extract the detection efficiency was defined. This is a self-consistent method using the measured data to extract the efficiency. The main idea is that having a 3 hadrons final state ($p\pi^+\pi^-$) it is possible to use the different topologies (all particle detected and 1 particle missing) to define a single particle efficiencies inside the fiducial cuts. Assuming each particle to be independent, the number of event seen in one defined topology is in fact:

$$N(p\pi^+ detected, \pi^- notdetected) = N_0 \epsilon_p \epsilon_{\pi^+}(1-\epsilon_{\pi^-}) \tag{2.2}$$

where the ϵ_{part} is the single particle efficiency and (1-ϵ_{part}) is the inefficiency to detect the particle. The ϵ_{part} related to the number of events with detected and missing particles as:

$$\epsilon_{\pi^+} = \frac{N_{p\pi^+\pi^- detected}}{N_{p\pi^- detected,\pi^+ missing}} \qquad \epsilon_{\pi^-} = \frac{N_{p\pi^+\pi^- detected}}{N_{p\pi^+ detected,\pi^- missing}} \qquad \epsilon_p = \frac{N_{p\pi^+\pi^- detected}}{N_{\pi^+\pi^- detected,p missing}} \tag{2.3}$$

The single particle efficiency were derived, as a function of momentum and theta in the LAB system in each CLAS sector, $\epsilon_{part}(\theta^{Lab}, p^{Lab}, sector)$. We did not use the SPE as main efficiency evaluation for some reasons:

- formula 2.2 does not take into account correlations between particles: the probability to detect one particle is not affected by the detection of another particle;
- the kinematical domain of each topology can be concentrated in an area where the single particle efficiency (for some of the particles), is not well determined; in fact, while to get the proton efficiency one has to use the topologies containing ($p\pi^+\pi^-$ detected) and

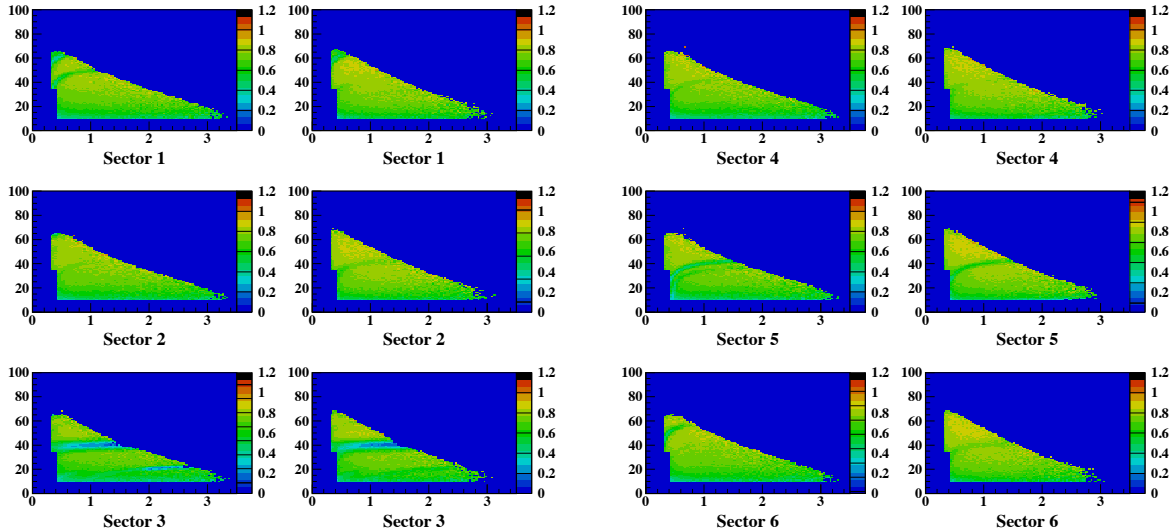

Figure 2.5: Proton SPE (within fiducial cuts) obtained from data (left) and simulations (right). The efficiency is shown as a function of particle momentum vs lab angle for each sector.

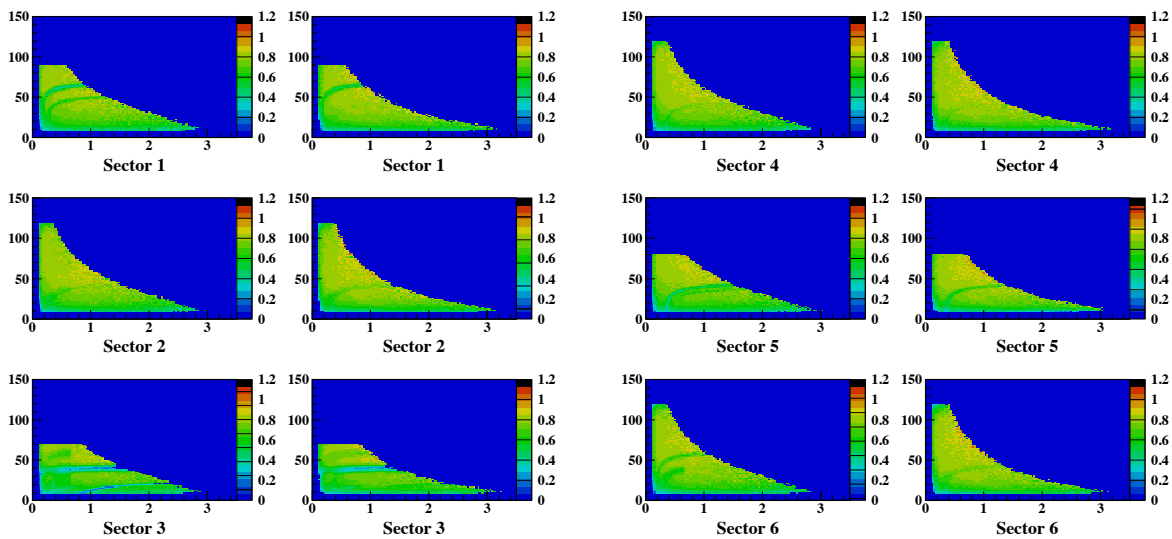

Figure 2.6: Positive π SPE (within fiducial cuts) obtained from data (left) and simulations (right). The efficiency is shown as a function of particle momentum vs lab angle for each sector.

($\pi^+\pi^-$detected,$p$missing) that involve some specific kinematic for the involved protons, the resulting SPE would be used to correct all the other topologies that, can have the proton in different kinematical domains;

- it is not clear how to take into account a possible bias introduced by the trigger.

Nevertheless, the SPEs can be defined both for the real data and for the simulations (passed trough the whole analysis chain) and then used for comparison. Because we are using a realistic event generator and a realistic description of CLAS (GSIM), the data and the simulation should give the same SPEs. Figures 2.5, 2.6, and 2.7 show the SPEs for *proton*, π^+ and π^- obtained from data and pseudo-data (simulations). Fig. 2.8 shows the SPEs data/sim ratio for the three hadrons.

From the comparison it results that the two SPEs well agree at 5-10% level within fiducial cuts demonstrationg that GSIM reproduce the CLAS features in detail.

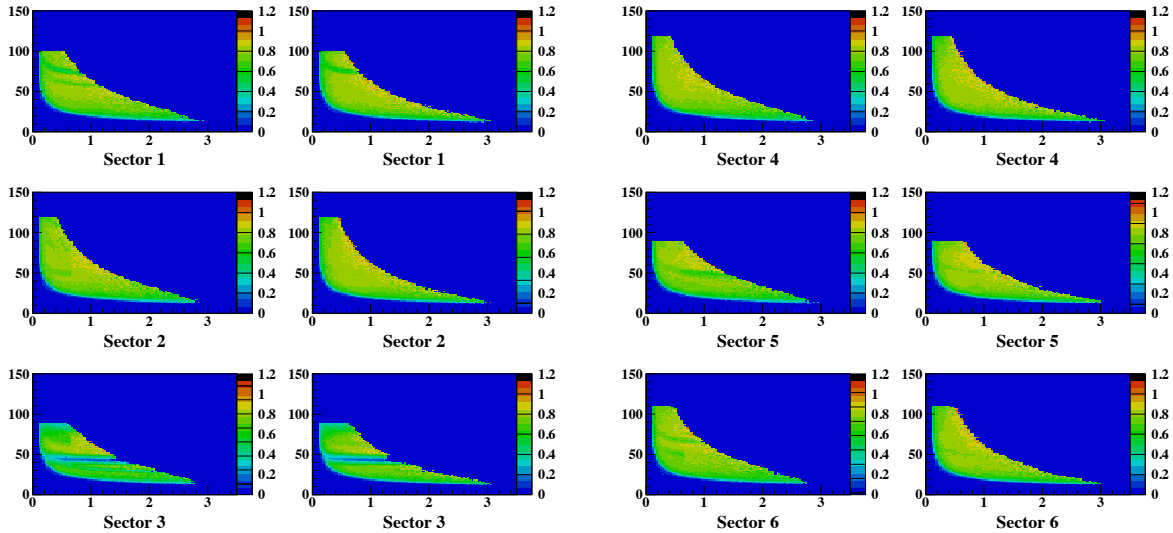

Figure 2.7: Negative π SPE (within fiducial cuts) obtained from data (left) and simulations (right). The efficiency is shown as a function of particle momentum vs lab angle for each sector.

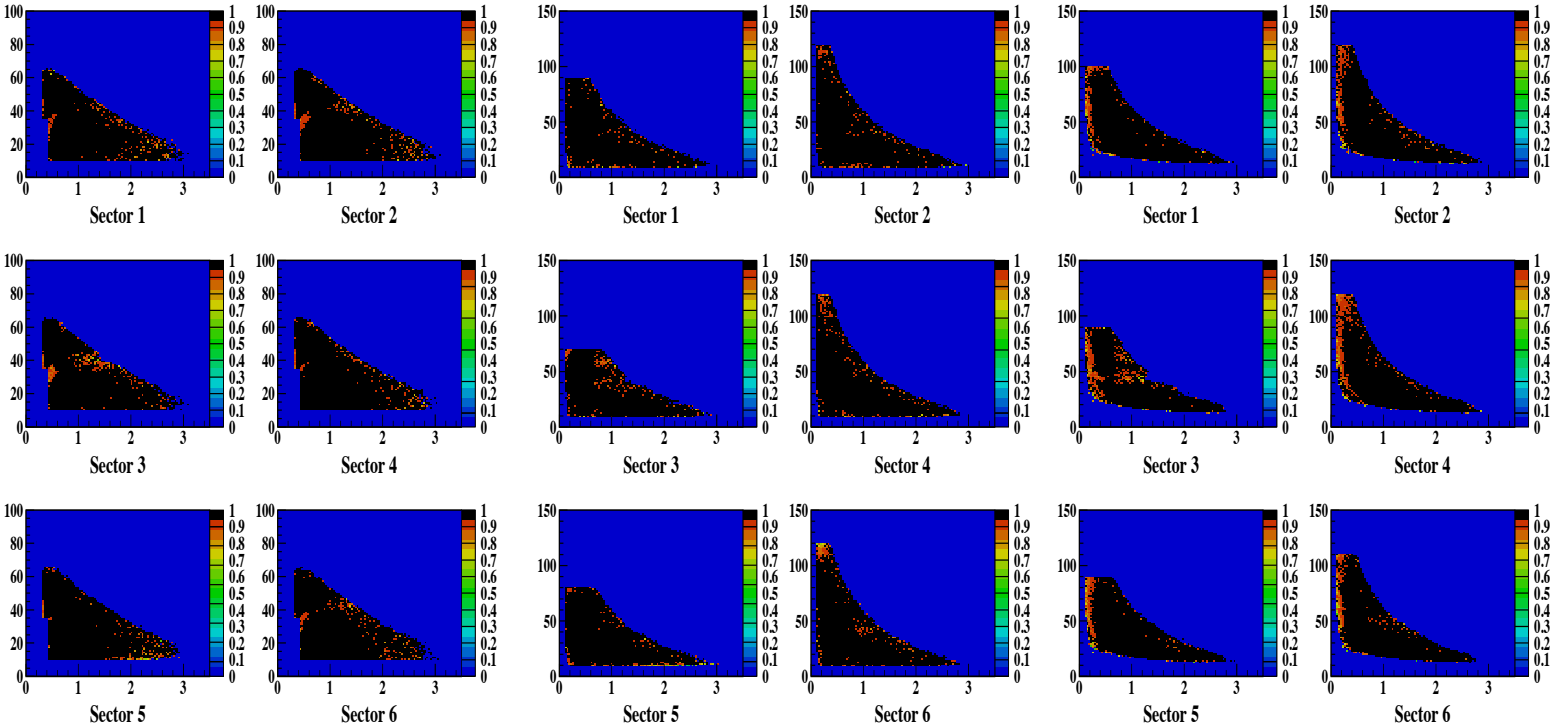

Figure 2.8: Ratio of SPE obtained from data and simulations for proton (left), π^+, and π^-.

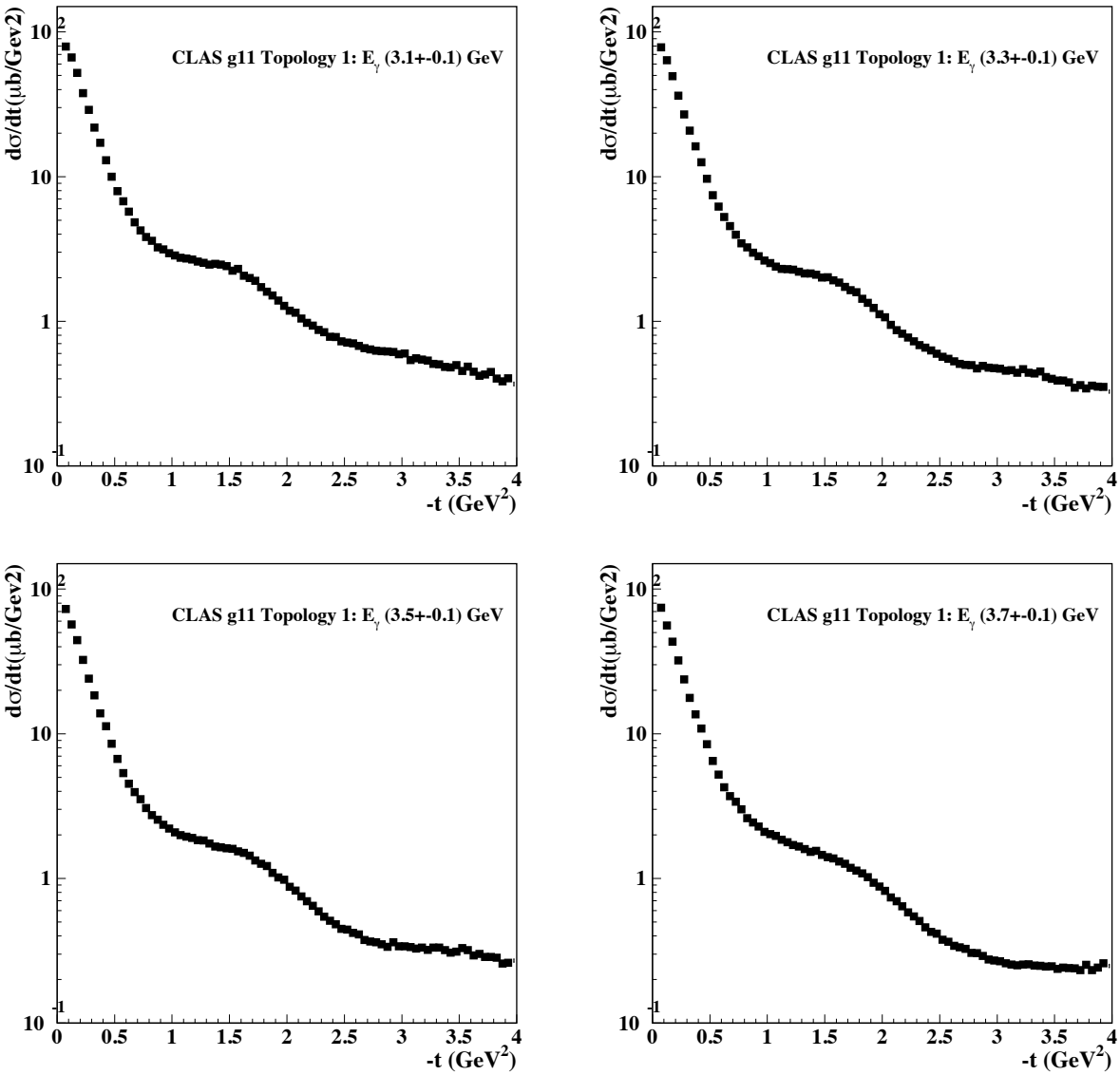

Figure 2.9: Differential cross section $d\sigma/dt$ for the reaction $\gamma p \to p\pi^+\pi^-$ in the 4 energy bins. Errors are statistical only.

2.2 The $\gamma p \to p\pi^+\pi^-$ cross section

The first result of our analysis is the differential cross section $d\sigma/dt$ (or $d\sigma/d\cos\theta^{CM}_{\pi^+\pi^-}$) for the reaction $\gamma p \to p\pi^+\pi^-$. Fig. 2.9 and fig. 2.10 show the differential cross sections in the 4 energy bins derived from the $p\pi^+$ topology. Total cross sections, resulting from the integration over $-t$ and over $cos\theta^{CM}_{\pi^+\pi^-}$ of the corresponding differential cross section are shown in fig. 2.11. The very forward region corresponding to $-t \sim 0$ or $\cos\theta^{CM}_{\pi^+\pi^-} \sim 1$ is strongly affected by the CLAS acceptance reduced to small values or even to zero in the very first bins. The extrapolation of the $-t$ and angular distributions in the unmeasured kinematic domain explains the difference between the two sets of points giving an estimate of the related systematic error. The good agreement with the existing data [33] confirms the quality of our data set and the validity of our procedure.

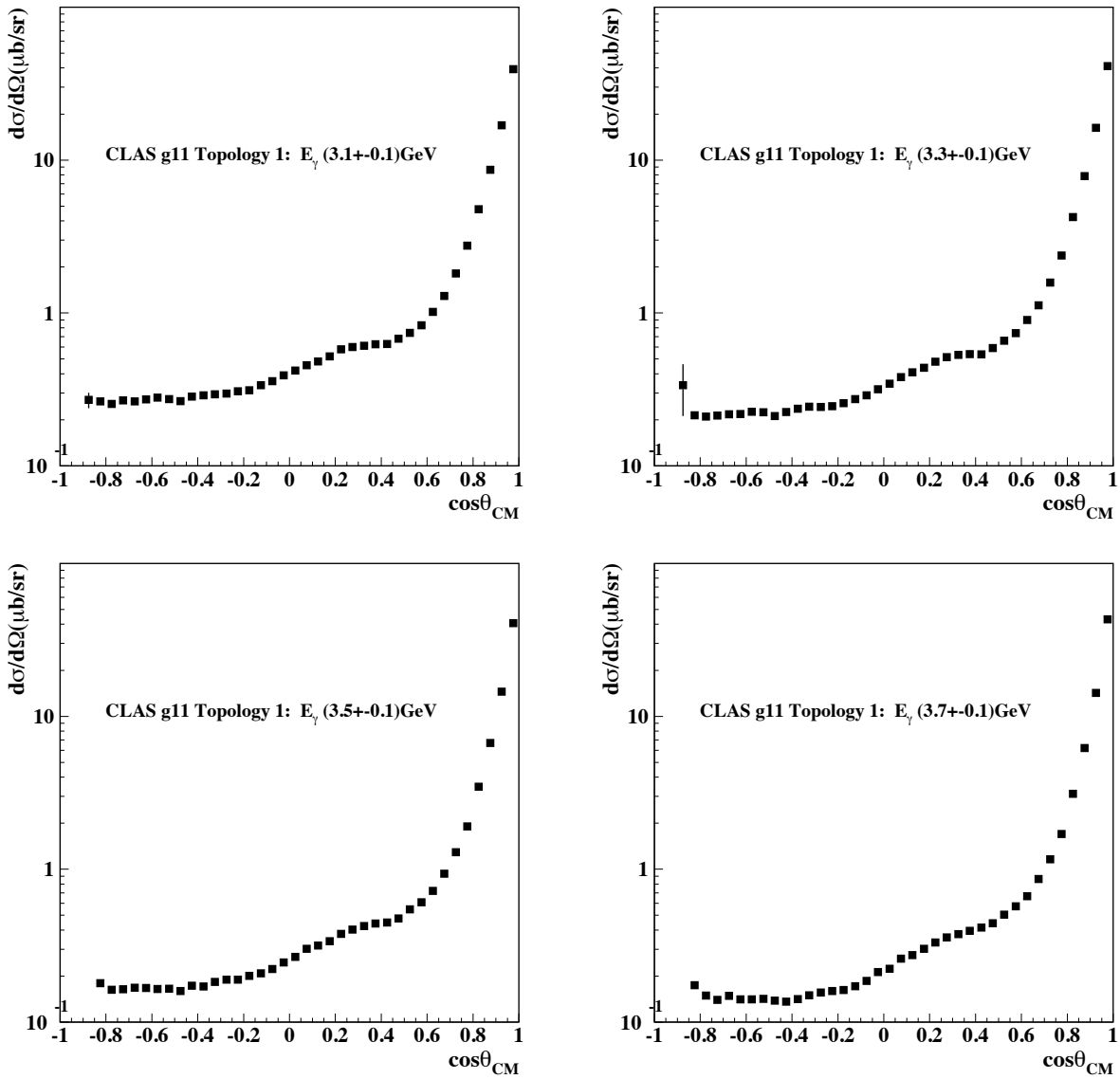

Figure 2.10: Differential cross section $d\sigma/dcos\theta^{CM}_{\pi^+\pi^-}$ for the reaction $\gamma p \rightarrow p\pi^+\pi^-$ in the 4 energy bins. Errors are statistical only.

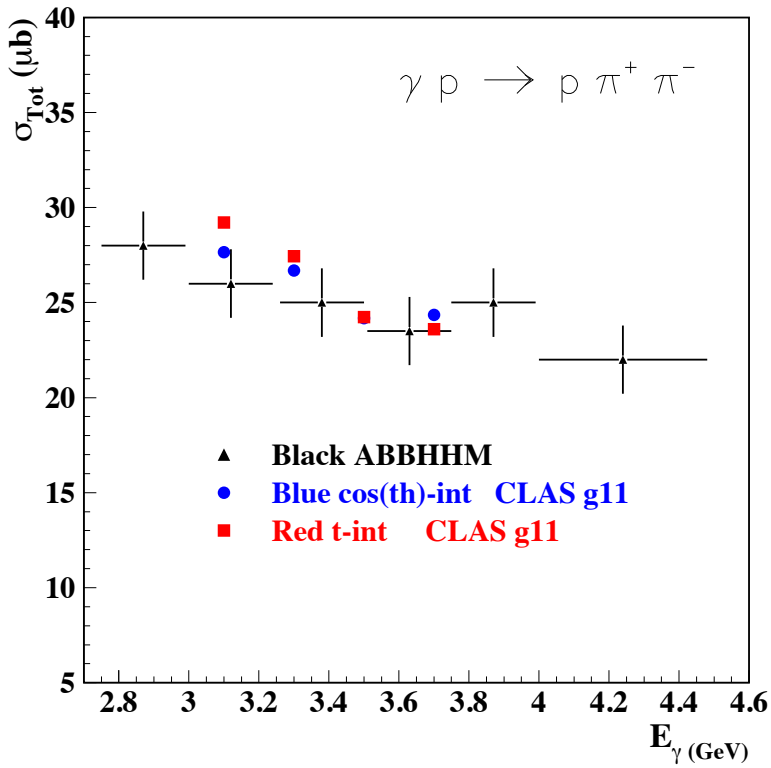

Figure 2.11: Total cross section for the reaction $\gamma p \to p\pi^+\pi^-$. Errors are statistical only.

2.3 The $\gamma p \to p\rho^0$ cross section

To disentangle the different channels contributing to the $p\pi^+\pi^-$ we used the same same approach used in the ABBHHM data analysis [33] and more recently used to analyse the ZEUS data [34]. The $(\pi^+\pi^-)$ invariant mass distribution was fitted using the following formula:

$$\frac{d\sigma}{dt\ dM(\pi^+\pi^-)} = A^2|(Breit{-}Wigner)_\rho + B/A + C(Breit{-}Wigner)_{f_2}|^2 + Pol(3^{th}order : D, E, F, G) \tag{2.4}$$

where $(Breit - Wigner)_X$ is the Breit-Wigner amplitude for the X-mass resonance with momentum dependent width $\Gamma_X(M_{\pi^+\pi^-})$ given in ref. [35] and A, B, C, D, E, F and G the free parameters in the fit. In this way the interference between the Breit-Wigner and the non resonant $(\pi\pi)$ production is taken into account. Figures 2.12, 2.13, and 2.14 show results of the fit for some selected and $-t$ and photon beam energy bins.

According to the analysis of *g6a* data set, the Breit-Wigner fit is close to what obtained using a realistic model that describes the 2-pions production as superposition of quasi-two-body channels and the following decay of the intermediate state [36] [1]. From that analysis, the model dependence was estimated to be within 10-20%. The resulting $d\sigma/dt$ for $\gamma p \to p\rho$ is reported in fig. 2.15 in the 4 photon energy bins.

[1] The reactions included in the model and the main mechanisms are: 1) $\gamma p \to p\rho$: described by the Pomeron exchange, the f2(1270) Regge trajectory exchange, the s-channel exchange (all known resonances), a phenomenological u-channel exchange; 2) $\gamma p \to \Delta^{++}(1232)\pi^-$: described by reggeized Born terms (contact, π-in-flight, ...) and s-channel exchange (all known resonances); 3) $\gamma p \to pf_2(1270)$: described by a phenomenological contact term and an s-channel form factor; 4) $\gamma p \to heavy - \Delta^{++}\pi^-$: phenomenological Breit-Wigner shape coming from the superposition of many $\Delta - states$; 5) $\gamma p \to p\pi^+\pi^-$: a phase space as a complex number, function of $C(W, t)$.

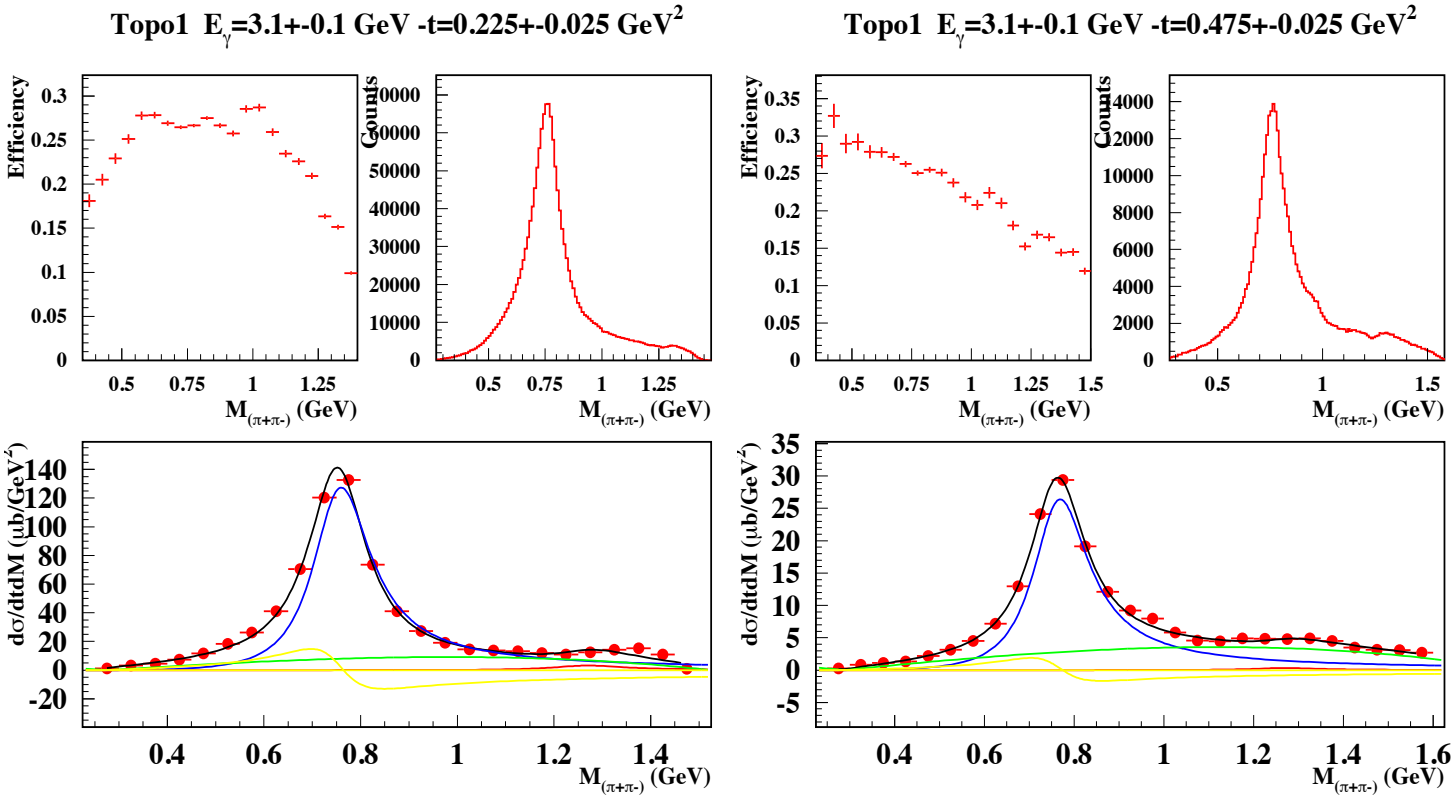

Figure 2.12: CLAS efficiency as a function of $M_{\pi^+\pi^-}$ (top-left), $M_{\pi^+\pi^-}$ raw distribution (top-right). Bottom: fit of $d\sigma/dtdM_{\pi^+\pi^-}$ (black line) with separated contributions (rho in blue, phase space in green, $f_2(1270)$ in red and interference term in yellow.

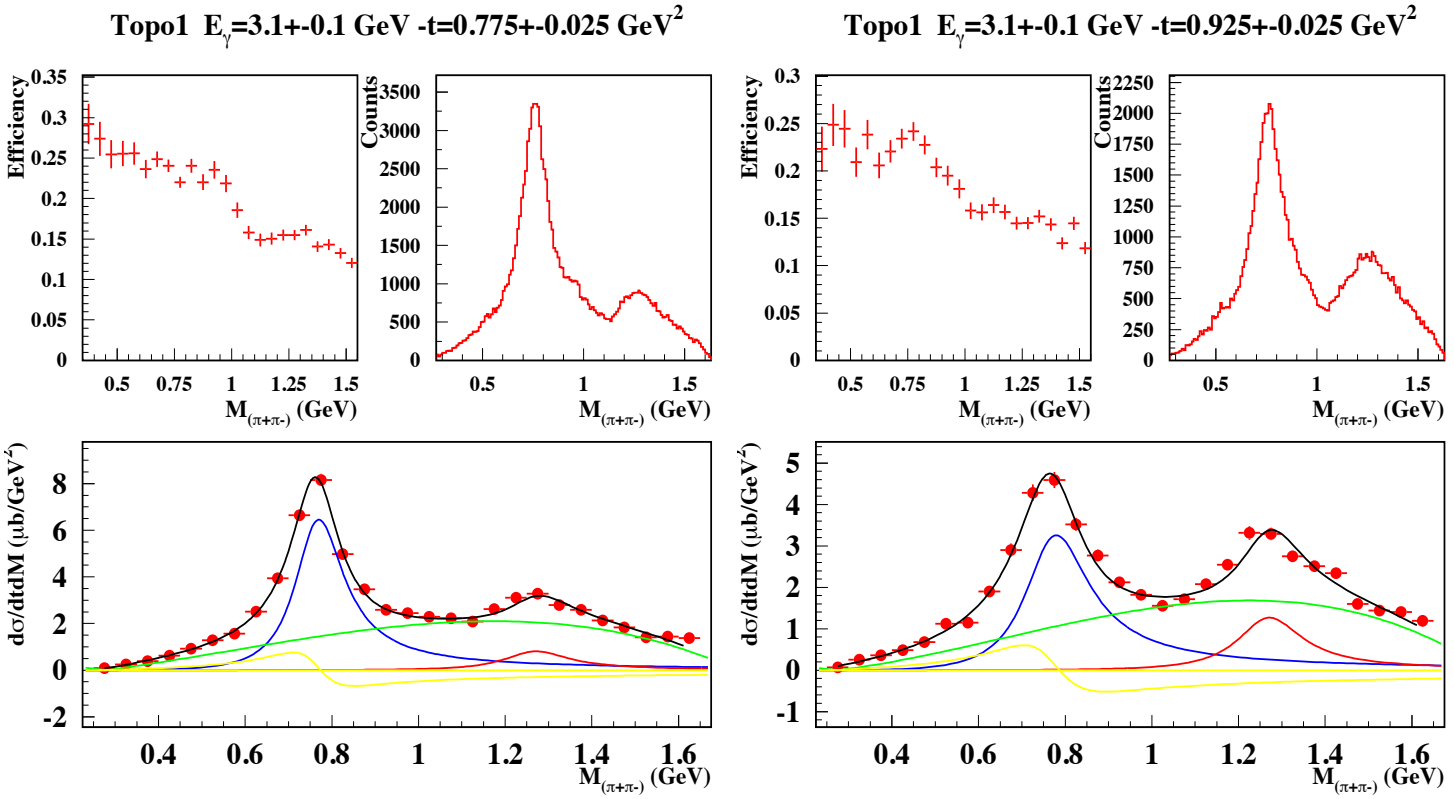

Figure 2.13: CLAS efficiency as a function of $M_{\pi^+\pi^-}$ (top-left), $M_{\pi^+\pi^-}$ raw distribution (top-right). Bottom: fit of $d\sigma/dtdM_{\pi^+\pi^-}$ (black line) with separated contributions (rho in blue, phase space in green, $f_2(1270)$ in red and interference term in yellow.

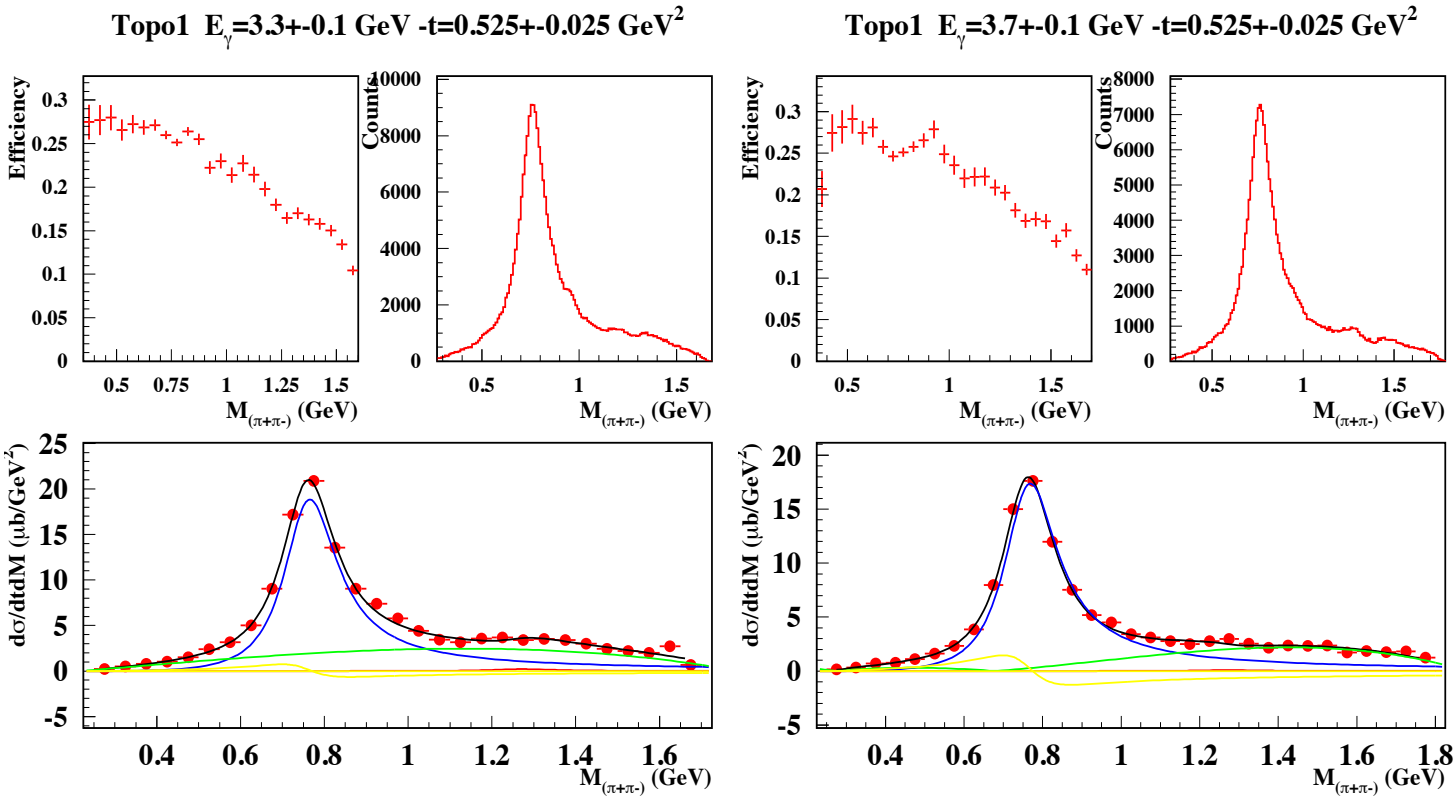

Figure 2.14: CLAS efficiency as a function of $M_{\pi^+\pi^-}$ (top-left), $M_{\pi^+\pi^-}$ raw distribution (top-right). Bottom: fit of $d\sigma/dtdM_{\pi^+\pi^-}$ (black line) with separated contributions (rho in blue, phase space in green, $f_2(1270)$ in red and interference term in yellow.

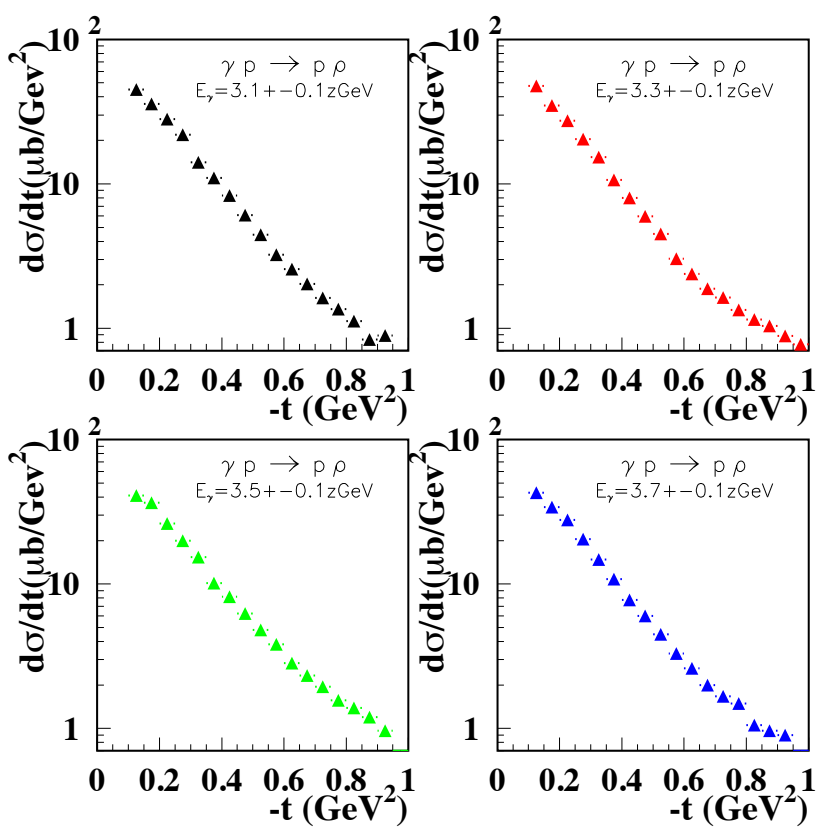

Figure 2.15: Differential cross section $d\sigma/dt$ for $\gamma p \to p\rho$ in the 4 photon beam energy bins.

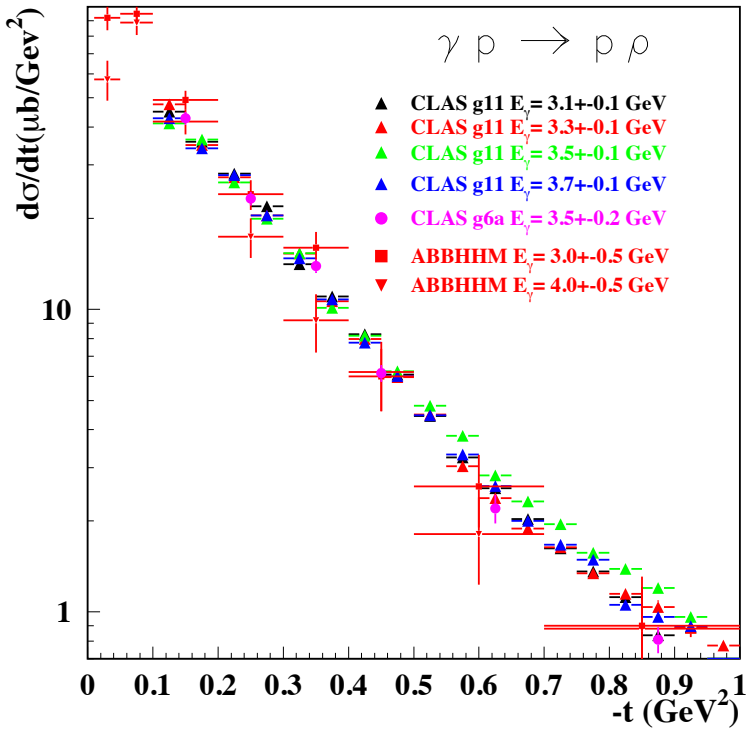

Figure 2.16: Differential cross section $d\sigma/dt$ from $g11$ compared to existing data. Errors are statistical only.

2.3.1 Comparison with previous experiments

Results from this analysis have been compared in fig. 2.16 to the previous measurement done by CLAS g6a data set [**?**] and ABBHHM Collaboration [33]. The similar photon energy range, the similar experimental procedure (identify the rho production through the measurement of the full final state) and the similar analysis procedure (especially the invariant masses fits) make the comparison between the three experiments particularly meaningful. Nevertheless, we have to remind some advantages of our experiment respect to the even in this dynamical domain (low -t): - tagged photons in place of bremmstralhung spectra subtraction; - better statistical and systematic error; The only disadvantage of CLAS is the poor rho-forward-produced coverage that do not allow to measure at $-t < 0.1$ GeV$^2/c^2$. As a check, we tried to derive the differential cross section from the topology $p\pi^+\pi^- detected$ but, as guessed in Par. **??**, the value obtained is sistematically lower than what derived using the first topology. Data points start to agree with the other set for $-t > 1$ GeV$^2/c^2$, where the corresponding efficiency start to be flat and comparable to the first topology.

Chapter 3

Partial wave analysis of $\gamma p \to p\pi^+\pi^-$

In this section we consider analysis of moments of di-pion angular distribution defined in equation 3.1 [1].

$$\langle Y_{\lambda\mu}\rangle(E_\gamma, t, M) = \frac{1}{\sqrt{4\pi}} \int d\Omega_\pi \frac{d\sigma}{dtdMd\Omega_\pi} Y_{\lambda\mu}(\Omega_\pi) \tag{3.1}$$

These moments are expressed as bilinear in terms of partial waves which are analyzed in Chapter 4. Extraction of moments requires that the measured angular distribution is corrected by acceptance. We study three methods for implementing acceptance corrections. The first one is to bin the data and MC in all kinematical variables and divide data by acceptance. The advantage of this method is that it enables theoretical analysis of the data without having to deal with the large MC files. It is, however, expected not to be reliable in bins where acceptance is small or vanishing. In the other two methods moments are expanded in a model-independent way in a set of basis functions and after weighting with MC, are compared to the data by maximizing the likelihood function. The first of these two parametrizes the theory in terms of *amplitudes* while the second uses directly *moments* as defined above. The approximations in these methods have to do with the choice of the basis and depend on the number of basis functions used. We study the systematic effects of such truncations. Here we exclusively focus on the $p\pi^+(\pi^-)$ topology binning data in 4 photon energy bins, 9 bins in momentum transfer $-t$ and 100 bins in the di-pion invariant mass. The binning definition is given in Table 2.1.2. In comparing the three fitting methods we use data without fiducial cuts and photon flux normalization. Once the optimal fitting strategy is established all subsequent fits are done after the cuts are being applied and data are properly normalized. For the definition of the angles in the di-pion system we follow the convention of Ballam *et al.* [1]. In the helicity system the $\pi^+\pi^-$ are at rest, the z-axis is chosen anti-parallel to the direction of the recoiling nucleon and the y-axis is parallel to $\mathbf{q} \times \mathbf{p}$ where $\mathbf{q}$ is the photon momentum in the lab and $\mathbf{p}$ is the di-pion momentum in the lab frame. The y-axis is invariant under the Lorentz boost relating the lab and the di-pion rest frames. The x-axis is obtained from $\mathbf{x} = \mathbf{y} \times \mathbf{z}$. The decay angles $\Omega_\pi = (\theta_\pi, \phi_\pi)$ are the polar and azimuthal angles of the π^+ flight direction in the helicity frame.

Unlike in the analysis described earlier in the document the MC simulations needed for extraction of moments are generated from a flat distribution in the $p\pi^+\pi^-$ phase space at given photon energy. The details of MC generation is described below. This is followed by the discussion of the three analysis methods.

[1] We show in Chapter 4 that moments are real thus we need only to consider $\mathrm{Re}Y_{\lambda\mu}$.

Bin number	Photon energy range ($E_{min} - E_{max}$) in GeV
1	3.0 - 3.2
2	3.2 - 3.4
3	3.4 - 3.6
4	3.6 - 3.8
Bin number	Negative of momentum transfer range ($\|t\|_{min} - \|t\|_{max}$) in GeV^2
1	0.1 - 0.2
2	0.2 - 0.3
3	0.3 - 0.4
4	0.3 - 0.5
5	0.5 - 0.6
6	0.6 - 0.7
7	0.7 - 0.8
8	0.8 - 0.9
9	0.9 - 1.0
Bin number	Di-pion mass range ($M_{min} - M_{max}$) in GeV
1	0.400 - 0.410
2	0.410 - 0.420
3	0.420 - 0.430
:	:
98	1.370 - 1.380
99	1.380 - 1.390
100	1.390 - 1.400

Table 3.1: Bin definitions.

3.1 Monte Carlo simulations

3.1.1 Generated events

Raw MC was generated according to three-particle phase space with a photon beam Bremsstrahlung energy spectrum defined as:

$$\frac{dN}{dEdtdMd\Omega_\pi d\phi_{cm}} \propto \frac{\rho(E)}{\sqrt{s}p_L}\sqrt{\frac{M^2}{4} - m_\pi^2} \propto \frac{\rho(E)}{E}\sqrt{\frac{M^2}{4} - m_\pi^2}. \tag{3.2}$$

Here $s = m_p^2 + 2Em_p$ is the square of the center of mass energy and $p_L = (s - m_p^2)/(2\sqrt{s})$ is the γp relative momentum in the center of mass frame. ϕ_{cm} is the azimuthal angle of the di-pion system in the center of mass frame with the z axis along the photon beam and the y axis perpendicular to the production plane. Ω_π is the π^+ decay solid angle as discussed above. Finally $\rho(E) \sim 1/E$ describes the photon spectrum. A sample of $1M$ raw events generated in the energy range ($3.0 < E_\gamma < 3.8$) GeV and covering the allowed kinematic range in t and $M_{\pi\pi}$ yields ~164k events in the $M_{\pi\pi}$ and $-t$ ranges of interest (0.4 GeV $< M_{\pi\pi} <$ 1.4 GeV , 0.1 GeV$^2 < -t <$ 1.0 GeV^2). The distributions restricted to these M and t bins are shown in Figs. 3.1.

The distribution of di-pion mass is shown in Fig. 3.2 for 4 energy bins and two bins in momentum transfer.

3.1.2 Reconstructed events

As an example, from 1M Monte Carlo generated events in the ($3.0 < E < 3.8$) GeV energy range approximately 164k events are reconstructed. Restriction to ($0.1 < -t < 1.0$) GeV^2 and (0.4

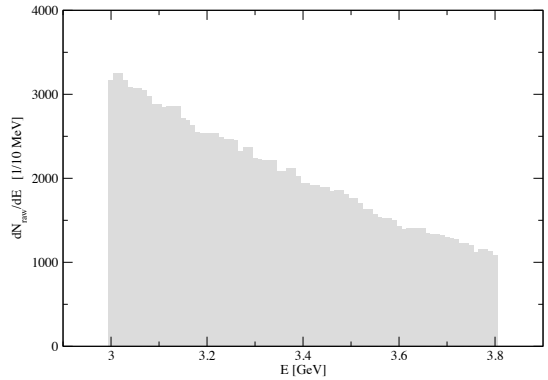

(a)

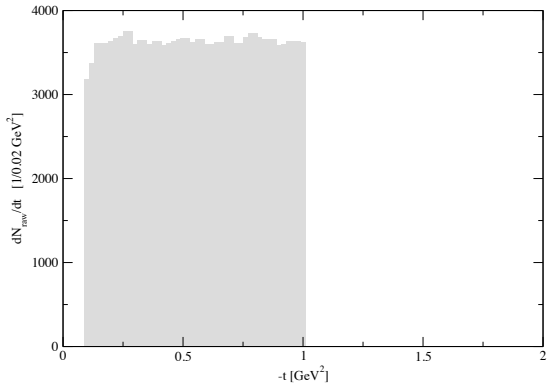

(b)

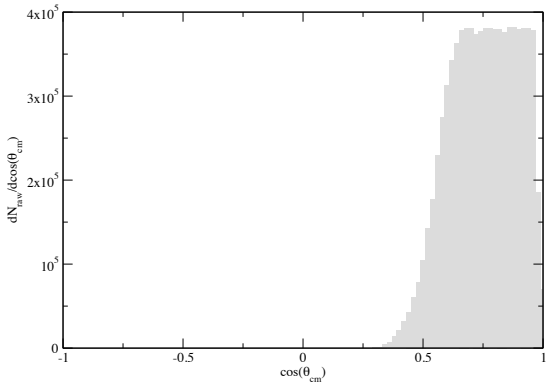

(c)

Figure 3.1: Generated distribution from 1M events in the t and M ranges considered in the analysis ($0.4 < M[\text{ GeV}] < 1.4, 0.1 < -t[\text{ GeV}^2] < 1.0$). a) Photon energy distribution, b) Momentum transfer distribution, c) distribution of the center of mass scattering angle (events are generated flat in $\cos\theta^{CM}_{\pi^+\pi^-}$ and restricted to $0.1 < -t$ GeV$^2 < 1.0$) in the analysis.

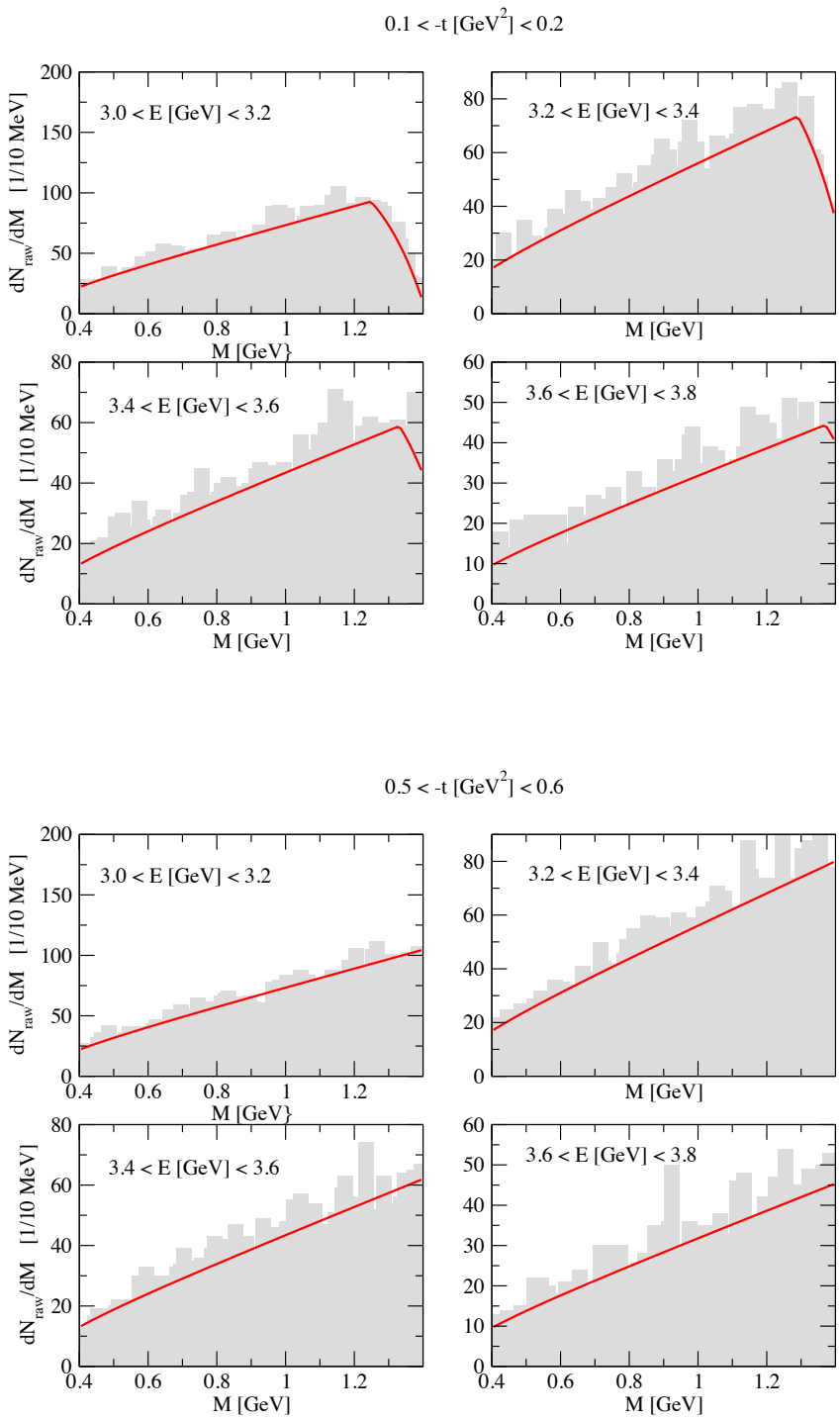

Figure 3.2: Raw distribution of di-pion mass generated from 1M events compared with theoretical curve representing the distribution given by Eq. 3.2.

$< M_{\pi\pi} < 1.4$) GeV reduces the yield to 41k events. The distributions of this event sample are shown in Fig. 3.3 as function of photon energy, momentum transfer $-t$, $\cos\theta^{CM}_{\pi^+\pi^-}$, and di-pion decay angles, respectively.

In this analysis a total of 4.03G events were generated corresponding to 660M reconstructed events

3.2 Extraction of moments of the di-pion angular distribution

In this section we describe the three procedures used to extract moments, we compare the results and we combine some of them to provide the final experimental moments.
As already mentioned, in the first method, acceptance corrections are applied to the data while in the other two corrections are applied to the theoretical parametrization of the data.

3.2.1 Un-normalized moments

For a given E_γ, t and di-pion mass M moments are defined by eq. 3.1, so that $\langle Y_{00}\rangle$ corresponds to the normalized di-pion production double differential cross section $d\sigma/dtdM$. In the following we refer to the $(E_i, t_j, M_k, \cos\theta_{\pi,l}, \phi_{\pi,m})$ bin as (i, j, k, l, m). We also define the un-normalized moments (not corrected for luminosity and bin size) as follow:

$$\langle\tilde{Y}_{\lambda\mu}\rangle_{data} = \sqrt{4\pi}\sum_{l,m}^{\Delta N_{data}(i,j,k)} \mathrm{Re}Y_{\lambda\mu}(\Omega_\pi) \tag{3.3}$$

where $\Delta N_{data}(i, j, k)$ is the number of data events in the (i, j, k) energy, momentum transfer $-t$, di-pion mass bin, $\Delta N_{data}(i, j, k) = \sum_{l,m} \Delta N_{data}(i, j, k, l, m)$ Thus the moments $\langle\tilde{Y}_{\lambda\mu}\rangle_{data}$ are normalized to the yield in the given (E_γ, t, M) bin so that

$$\frac{\langle\tilde{Y}_{00}\rangle_{data}}{0.1\ \mathrm{GeV}^2 10\ \mathrm{MeV}} = \frac{\Delta N_{data}(E, t, M)}{\Delta t\Delta M} \tag{3.4}$$

Finally we define $\langle\tilde{Y}_{\lambda\mu}\rangle$ moments by

$$\langle\tilde{Y}_{\lambda\mu}\rangle = \sqrt{4\pi}\sum_{l,m}^{\Delta N_{th(i,j,k)}} \mathrm{Re}Y_{\lambda\mu}(\Omega_\pi) \tag{3.5}$$

where $\Delta N_{th}(i, j, k)$ is the predicted *i.e.* corrected for acceptance, number of events in the particular energy (i), momentum transfer (j) and di-pion mass (k) bin. The ratio of the $\langle Y_{\lambda\mu}\rangle$ defined in Eq. 3.1 and $\langle\tilde{Y}_{\lambda\mu}\rangle$ involves the photon flux.

3.2.2 Absolute normalization

Moments defined above are not corrected for luminosity and bin size incorporating only the correction for the CLAS acceptance. In particular, the $\langle\tilde{Y}_{00}\rangle$ moment is normalized to the fitted number of events *i.e.* number of data events corrected by acceptance.

The normalized cross section is therefore given by

$$\frac{\Delta\sigma}{\Delta t\Delta M}(i, j, k) = \frac{\Delta N_{th}}{\Delta t\Delta M}(i, j, k)I^{-1}(E_i) = \frac{\langle\tilde{Y}_{00}\rangle(i, j, k)}{0.1\mathrm{GeV}^2 \times 10\mathrm{MeV}}(i, j, k)I^{-1}(E_i) \tag{3.6}$$

where $I(E_i)$ is the luminosity in units $1/\mu b$ tabulated in Table 3.2 .
The single-differential cross section is given by

$$\frac{\Delta\sigma}{\Delta t}(i, j) \quad = \quad \sum_{k=M_{min}}^{M_{max}} \frac{\langle\tilde{Y}_{00}\rangle(i, j, k)}{0.1\ \mathrm{GeV}^2} I^{-1}(E_i) \tag{3.7}$$

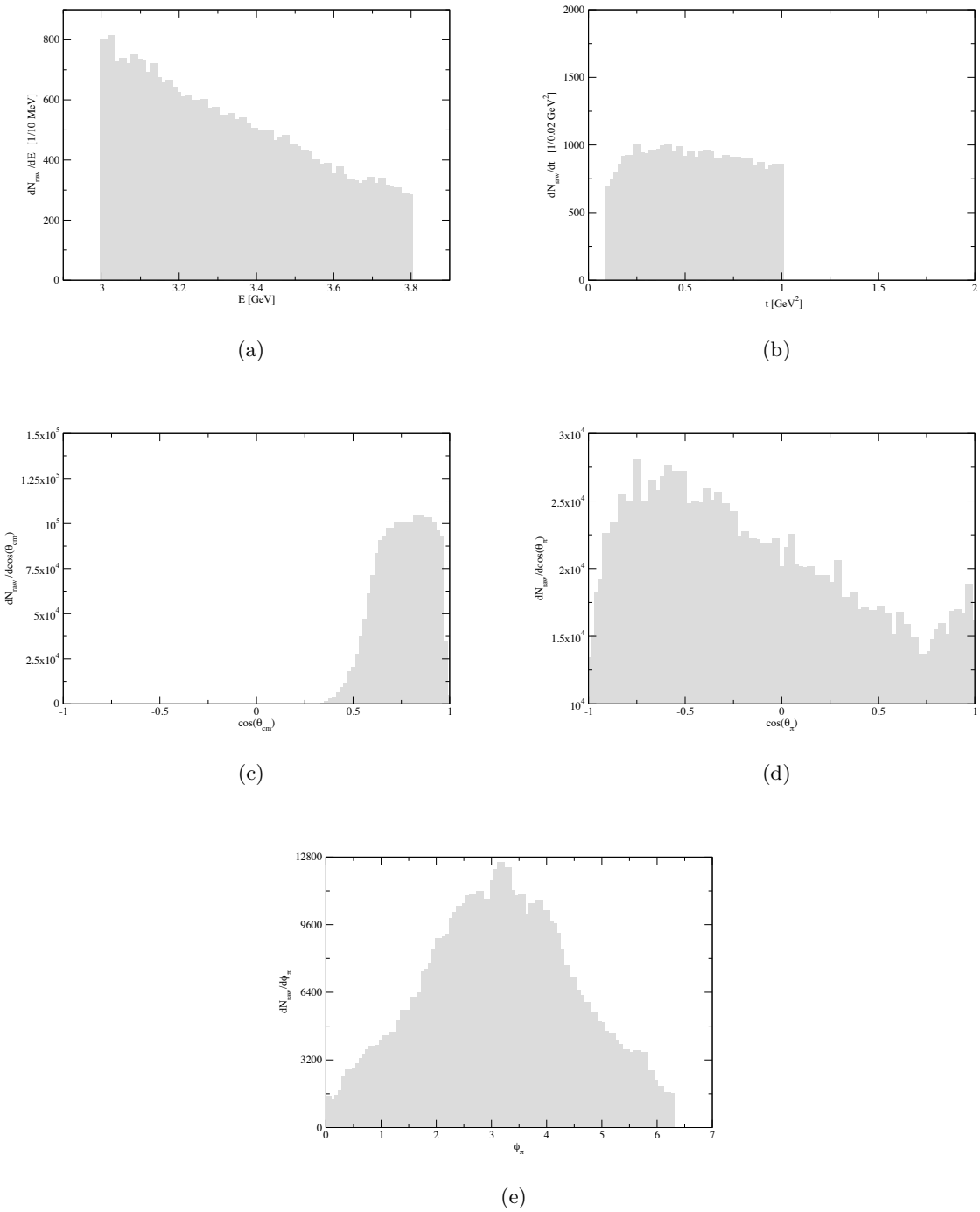

Figure 3.3: Reconstructed events from a sample of 1M generated with $-t$ and M in the range considered in the analysis ($0.4 < M[\text{ GeV}] < 1.4, 0.1 < -t[\text{ GeV}^2] < 1.0$). a) Photon energy, b) momentum transfer $-t$, c) $\cos\theta^{CM}_{\pi^+\pi^-}$, d) polar angle of the π^+ in the helicity frame, e) azimuthal angle of the π^+.

Bin number	Photon energy range ($E_{min} - E_{max}$) in GeV	$I(E_i)[\mu b]^{-1}$
1	3.0 - 3.2	2.97031×10^6
2	3.2 - 3.4	2.77892×10^6
3	3.4 - 3.6	2.78193×10^6
4	3.6 - 3.8	2.64611×10^6

Table 3.2: Luminosity as a function of photon energy. As reported in Par. 1.5, the photon flux error is dominated by the systematic uncertainties related to the corrections on the raw photon yields estimated to be in the range of 10 %.

Sytematic error on photon flux evaluation is estimated to be of the order of 10% (see par. 1.5). This value was added in quadrature to the statistical error of each moment.

3.2.3 First method: moments of efficiency corrected data

The acceptance correction is performed as follows. While the binning in E_γ, $-t$ and M was chosen as reported in Tab. 3.1, three different combinations of $\cos(\theta_\pi)$ and ϕ_π binning were tested: A) $(n_\theta, n_\phi) = (25, 25)$, B) $(n_\theta, n_\phi) = (10, 25)$, and C)$(n_\theta, n_\phi) = (10, 10)$. For each choice, the CLAS acceptance is defined as:

$$\eta(i,j,k,l,m) = \frac{\Delta N_{rec.}(i,j,k,l,m)}{\Delta N_{gen.}(i,j,k,l,m)} \tag{3.8}$$

where $\Delta N_{gen.}(i,j,k,l,m)$ and $\Delta N_{rec.}(i,j,k,l,m)$ are the number of generated and reconstructed events in the given bin. The expected (acceptance corrected) number of events is then given by:

$$\Delta N_{th}(i,j,k,l,m) = \frac{\Delta N_{data}(i,j,k,l,m)}{\eta(i,j,k,l,m)} \tag{3.9}$$

with the error estimated by:

$$\delta\Delta N_{th}(i,j,k,l,m) = \Delta N_{th}(i,j,k,l,m)\sqrt{\left[\frac{\delta[\Delta N_{data}(i,j,k,l,m)]}{\Delta N_{data}(i,j,k,l,m)}\right]^2 + \left[\frac{\delta[\Delta N_{rec.}(i,j,k,l,m)]}{\Delta N_{rec.}(i,j,k,l,m)}\right]^2} \tag{3.10}$$

and

$$\delta[(\Delta N_{data}(i,j,k,l,m)] = \sqrt{\Delta N_{data}(i,j,k,l,m)} \tag{3.11}$$

$$\delta[\Delta N_{rec.}(i,j,k,l,m)] = \sqrt{\Delta N_{rec.}(i,j,k,l,m)} \tag{3.12}$$

In Fig. 3.4 we plot acceptance in a single E, $-t$ and M bin for a few bins in ϕ_π as a function of $\cos(\theta_\pi)$. The plots clearly show holes in acceptance. An example of the expected number of events is shown in Fig. 3.5. Points are missing where acceptance vanishes preventing computation of ΔN_{th} in the full range of the angular variables. Finally in Fig. 3.6 we show acceptance integrated over the helicity angles and the di-pion mass *i.e*,

$$\eta(i,j) = \frac{\sum_{k,l,m} N_{rec.}(i,j,k,l,m)}{\sum_{k,l,m} N_{gen.}(i,j,k,l,m)} \tag{3.13}$$

On average acceptance is about 25%.

The expected number of events $\Delta N_{data}(i,j,k,l,m)$ is related to moments defined above as:

$$\Delta N_{th}(E,t,M,\theta_\pi,\phi_\pi) = \sqrt{4\pi}\sum_\lambda \sum_{\mu=0}^{\lambda} \frac{\langle \tilde{Y}_{\lambda\mu}\rangle(E,t,M)}{\epsilon_\lambda}\, \mathrm{Re}Y_{\lambda\mu}(\theta_\pi,\phi_\pi) \tag{3.14}$$

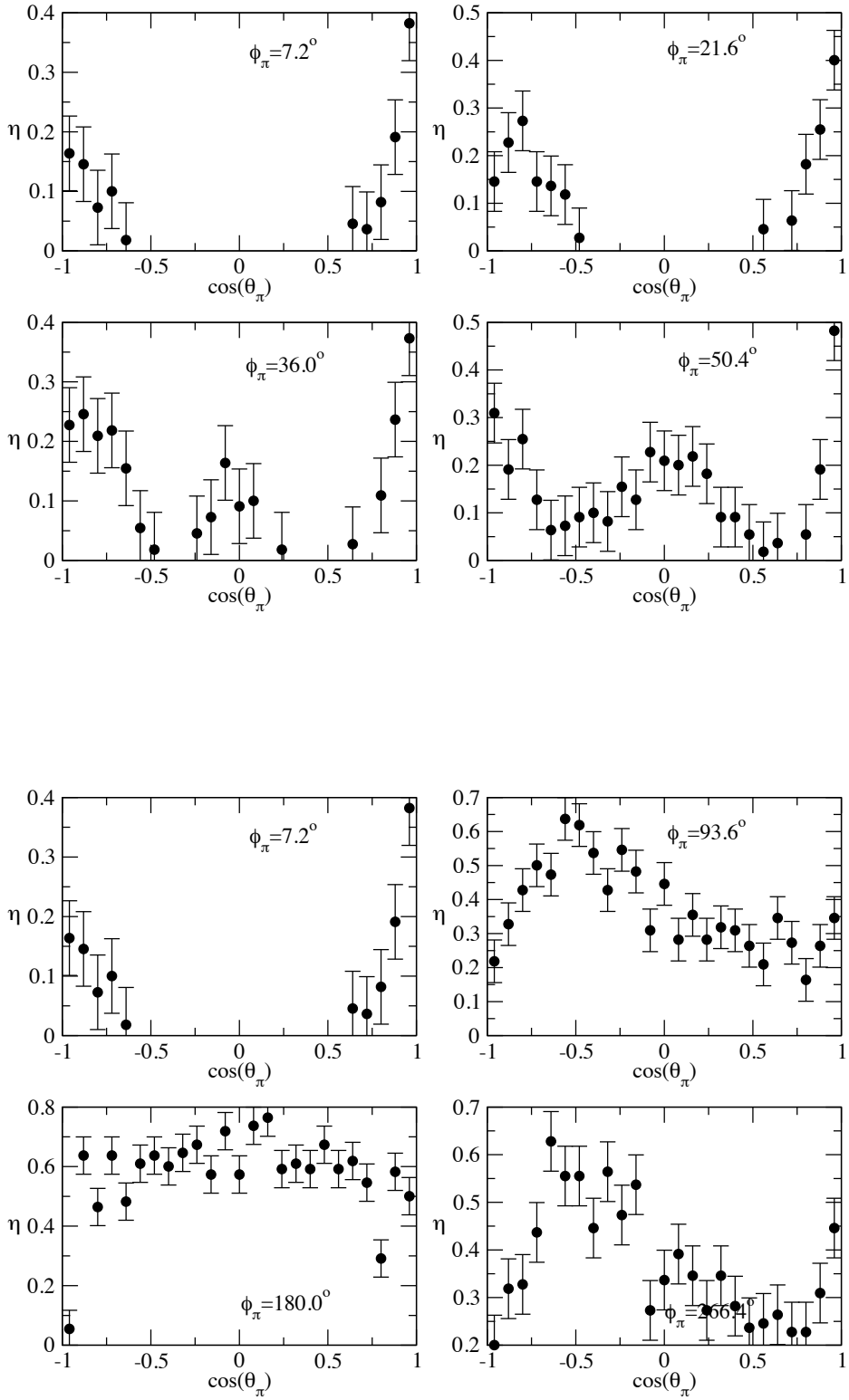

Figure 3.4: Acceptance η as a function of the π^-, $s-$channel polar angle for $3.4 < E < 3.6$, $0.5 < -t < 0.6$ and $M = 0.775$ GeV

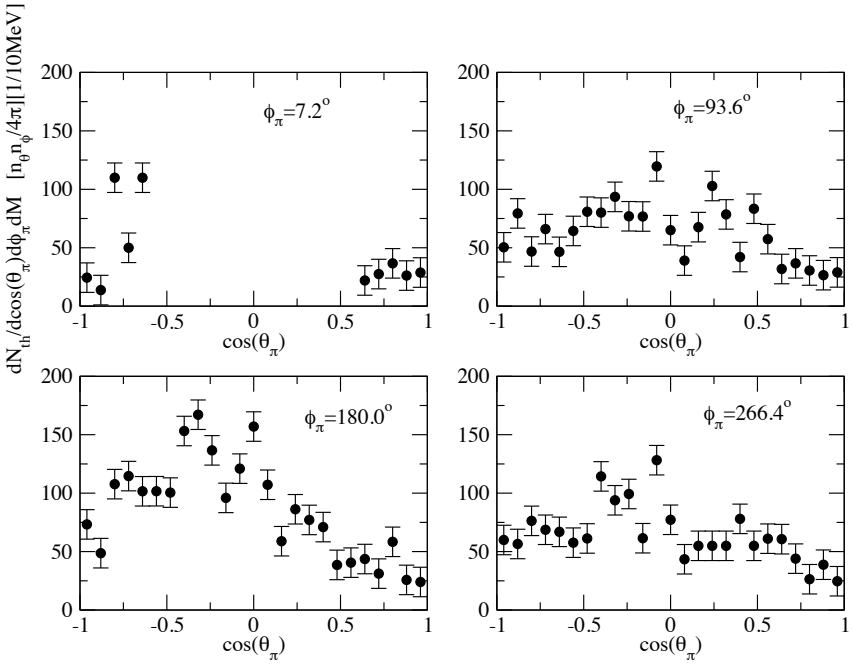

Figure 3.5: Number of events corrected for acceptance for ($n_\theta n_\phi = 625$).

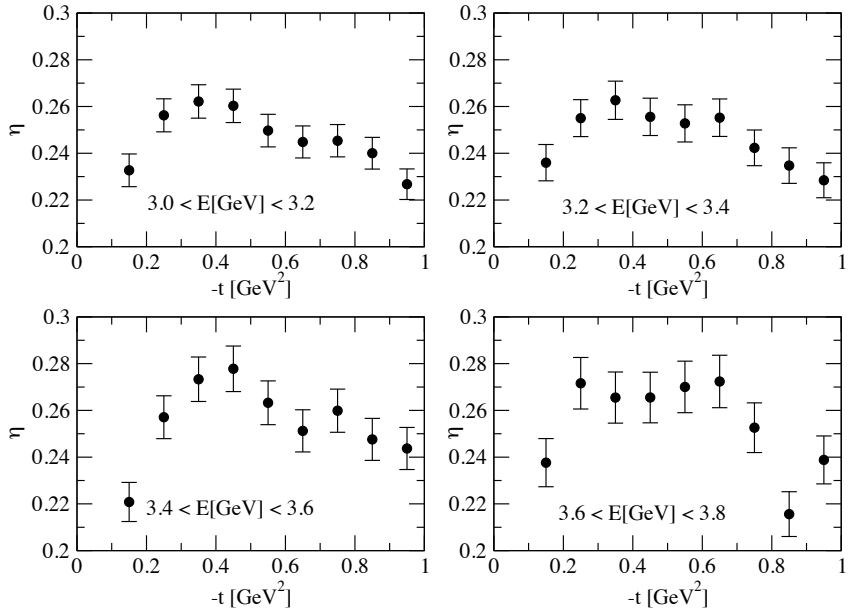

Figure 3.6: Acceptance as a function of momentum transfer in the four photon energy bins.

where $\epsilon_\lambda = 1$ for $\lambda = 0$ and 1/2 for all other $(\lambda\mu)$. Only positive values of M are used since moments are real. The inversion procedure is not exact since the sum of $(\lambda\mu)$ is typically restricted to $\lambda \leq \lambda_{max}$ $(\mu < \lambda)$. The expected (acceptance corrected) angular moments

$$\langle \tilde{Y}_{\lambda\mu} \rangle_{data}(E, t, M) \to \langle \tilde{Y}_{\lambda\mu} \rangle(i, j, k) \tag{3.15}$$

are computed by minimizing, in each (i, j, k) bin independently, the χ^2 defined by

$$\chi^2(i,j,k) = \sum_{l=1}^{n_\theta} \sum_{m=1}^{n_\phi} \frac{\left[\Delta N_{th}(i,j,k,l,m) - \frac{\sqrt{4\pi}}{n_\theta n_\phi} \sum_{\lambda=0}^{\lambda_{max}} \sum_{\mu=0}^{\lambda} \langle \tilde{Y}_{\lambda\mu} \rangle(i,j,k) \ \mathrm{Re} Y_{\lambda\mu}(\cos(\theta_{\pi,l}), \phi_{\pi,m})\right]^2}{\delta^2_{ijk}} \tag{3.16}$$

where δ_{ijk} is the statistical error on ΔN_{data} integrated over pion angles (l, m).

In Appendix A we show the details of the systematics study performed on the fit varying the number of bins in the helicity angle and λ_{max}. We concluded that the fits are reasonable stable for low moments and the higher moments are clearly needed to describe the low $p\pi$ mass region but those cannot be constrained by this method of fitting. The best compromise was obtained with $n_\theta = (25, 25), n_\phi = (25, 25)$ and $\lambda_{max} = 4$. Fig. 3.7 show the resulting normalized moments in one E and t bin, $(3.2 < E < 3.4,\ 0.5 < -t < 0.6)$. When the fit results are compared to the data, see fig. A.2, the difference remains within 15-20% showing that this methods is not optimal.

3.2.4 Second and third methods: moments derived using efficiency-corrected fitting function

For these methods corrections are applied to the theoretical parametrization of the data. The theoretical expected yield is parametrized in terms of appropriate physics functions: production amplitudes in one case and moments of the cross section in the other. This yield, corrected for acceptance, is then compared to the measured yield (uncorrected). Parameters are extracted by maximizing the likelihood function defined as:

$$\mathcal{L} \sim \Pi_{a=1}^{n} \left[\frac{\eta(\tau_a) I(\tau_a)}{\int d\tau \eta(\tau) I(\tau)} \right]. \tag{3.17}$$

Here a represents a data event, $n = \Delta N_{dat}(i, j, k)$ is the number of data events in a given (E_γ, t, M) bin, *i.e.* the fit is done independently in each bin, τ_a represents the set of kinematical variables of the a-th event, $\eta(\tau_a)$ is the corresponding acceptance and $I(\tau_a)$ it the theoretical function representing expected events distribution. The measure $d\tau$ includes the phase space factor and the likelihood function is normalized to the expected number of events in the bin

$$\bar{n} = \int d\tau \eta(\tau) I(\tau) \tag{3.18}$$

The advantage of this approach lies in avoiding the data binning and the large uncertainties related to the correction in the regions with vanishing efficiencies. Comparison of the results of the two different parameterizations of the theory allow one to access systematic errors. In the following, we describe in more details the two approaches.

Method 2: parametrization with amplitudes

The theoretical expected yield in each bin is described as:

$$I(\tau_a) = I(E, M, t, \theta_\pi, \phi_\pi) \to I(i, j, k; \theta_\pi, \phi_\pi) = 4\pi \left| \sum_{\lambda=0}^{\lambda_{max}} \sum_{m=-\lambda}^{\lambda} a_{\lambda\mu}(i, j, k) Y_{\lambda\mu}(\theta_\pi, \phi_\pi) \right|^2 \tag{3.19}$$

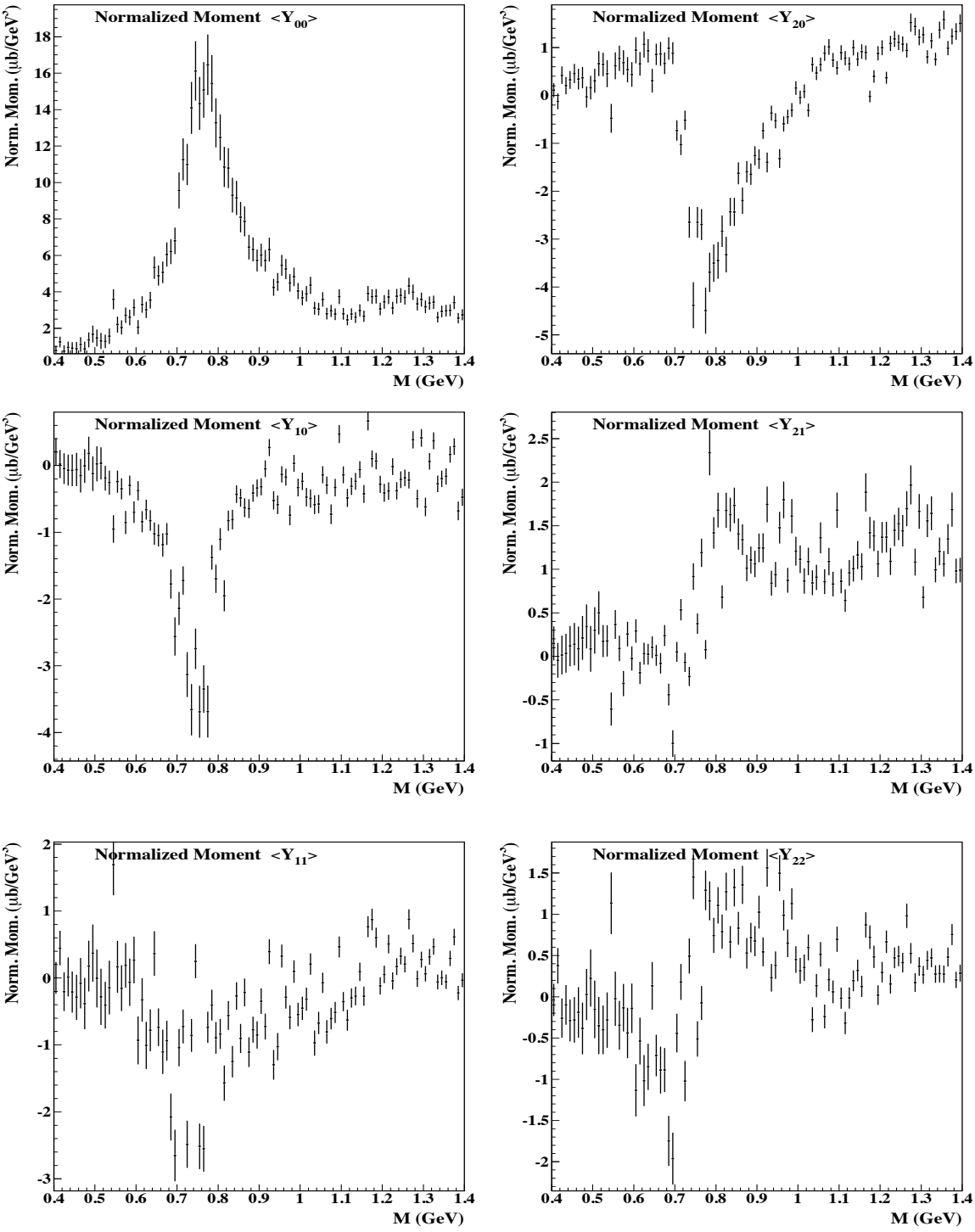

Figure 3.7: Normalized moments in $3.4 < E < 3.6$, $0.5 < -t < 0.6$ bins using the first method. Errors include the systematic uncertainty on the absolute normalization and moment extraction procedure.

The advantage of this parametrization is that the intensity function $I(\tau_a)$ is by construction positive. However it can lead to ambiguous results since it has more parameters than can be determined from the data. In addition, for practical reasons, the parametrization involves a cutoff, λ_{max}, in the maximum number of amplitudes. We also note that these amplitudes are not the same as the partial wave amplitudes in the common sense of a di-pion photoproduction amplitude since the later depend on the nucleon and photons spins.
The fit is performed minimizing the function (removing the irrelevant constants):

$$-2\ln\mathcal{L} = -2\sum_{a=1}^{\Delta N_{data}(i,j,k)} \ln\eta(\tau_a)I(\tau_a) + 2\Delta N_{data}(i,j,k)\ln\sum_{\lambda'\mu';\lambda\mu}\tilde{a}^*_{\lambda'\mu'}(i,j,k)\tilde{a}_{\lambda\mu}(i,j,k)\Psi_{\lambda'\mu';\lambda,\mu}(i,j,k) \tag{3.20}$$

where we introduced the rescaled amplitudes, $\tilde{a}_{\lambda\mu}(i,j,k)$ defined by

$$\tilde{a}_{\lambda\mu}(i,,j,k) = \sqrt{\eta(i,j,k)}a_{\lambda\mu}(i,j,k) \tag{3.21}$$

and the acceptance matrix Ψ is computed using the reconstructed MC as

$$\eta(i,j,k)\Psi_{\lambda'\mu';\lambda\mu}(i,j,k) = \frac{4\pi}{\Delta N_{gen.}(i,j,k)}\sum_{a=1}^{\Delta N_{rec.}(i,j,k)} Y^*_{\lambda'\mu'}(\theta_\pi,\phi_\pi)Y_{\lambda\mu}(\theta_\pi,\phi_\pi) \tag{3.22}$$

Resealing of the coefficients leads to the condition:

$$\sum_{\lambda=0}^{\lambda_{max}}\sum_{\mu=-\lambda}^{\lambda}|a_{\lambda\mu}(i,j,k)|^2 = 1 \tag{3.23}$$

which is checked at the end of each fit. After the coefficients $a_{\lambda\mu}$ are determined by maximizing the log-likelihood, moments are computed as:

$$\langle\tilde{Y}_{\lambda\mu}\rangle(i,j,k) = \frac{1}{\sqrt{4\pi}}\int d\Omega_\pi I(i,j,k,\theta_\pi,\phi_\pi)\ \mathrm{Re}Y_{\lambda\mu}(\Omega_\pi) = \sum_{\lambda_1\mu_1;\lambda_2\mu_2}\sqrt{\frac{(2\lambda_1+1)(2\lambda+1)}{2\lambda_2+1}}$$
$$\times\ \langle\lambda_1 0;\lambda 0|\lambda_2 0\rangle\frac{1}{2}\left[\langle\lambda_1\mu_1;\lambda\mu|\lambda_2,\mu_2\rangle + (-1)^\mu(\mu\to-\mu)\right]a_{\lambda_1\mu_1}(i,j,k)a^*_{\lambda_2,\mu_2}(i,j,k) \tag{3.24}$$

Fits are done using MINUIT with the analytical expression for the gradient, and using the SIMPLEX procedure followed by MIGRAD. After each fit covariance matrix is checked and if not positive definite the fit is restarted with random input parameters. At the end errors are computed from the full covariance matrix.

As shown in Appendix A, see fig. A.6, this method is superior over the first analysis method described in previous section (moments extracted from efficiency corrected data). For $\lambda_{max} \geq 2$ the low moments are already stable. Fig. 3.8 show the resulting normalized moments for $\lambda_{max} = 2$ in the same E and t bin as in the previous paragraph ($3.4 < E < 3.6$, $0.5 < -t < 0.6$).

Method 3: parametrization with moments

The theoretical expected yield in each bin is described as:

$$I(\tau_a) = I(E,M,t,\theta_\pi,\phi_\pi) \to I(i,j,k;\theta_\pi,\phi_\pi) = \sqrt{4\pi}\sum_{\lambda=0}^{\lambda_{max}}\sum_{m=0}^{\lambda}\langle\tilde{Y}_{\lambda\mu}\rangle(i,j,k)\ \mathrm{Re}Y_{\lambda\mu}(\Omega_\pi) \tag{3.25}$$

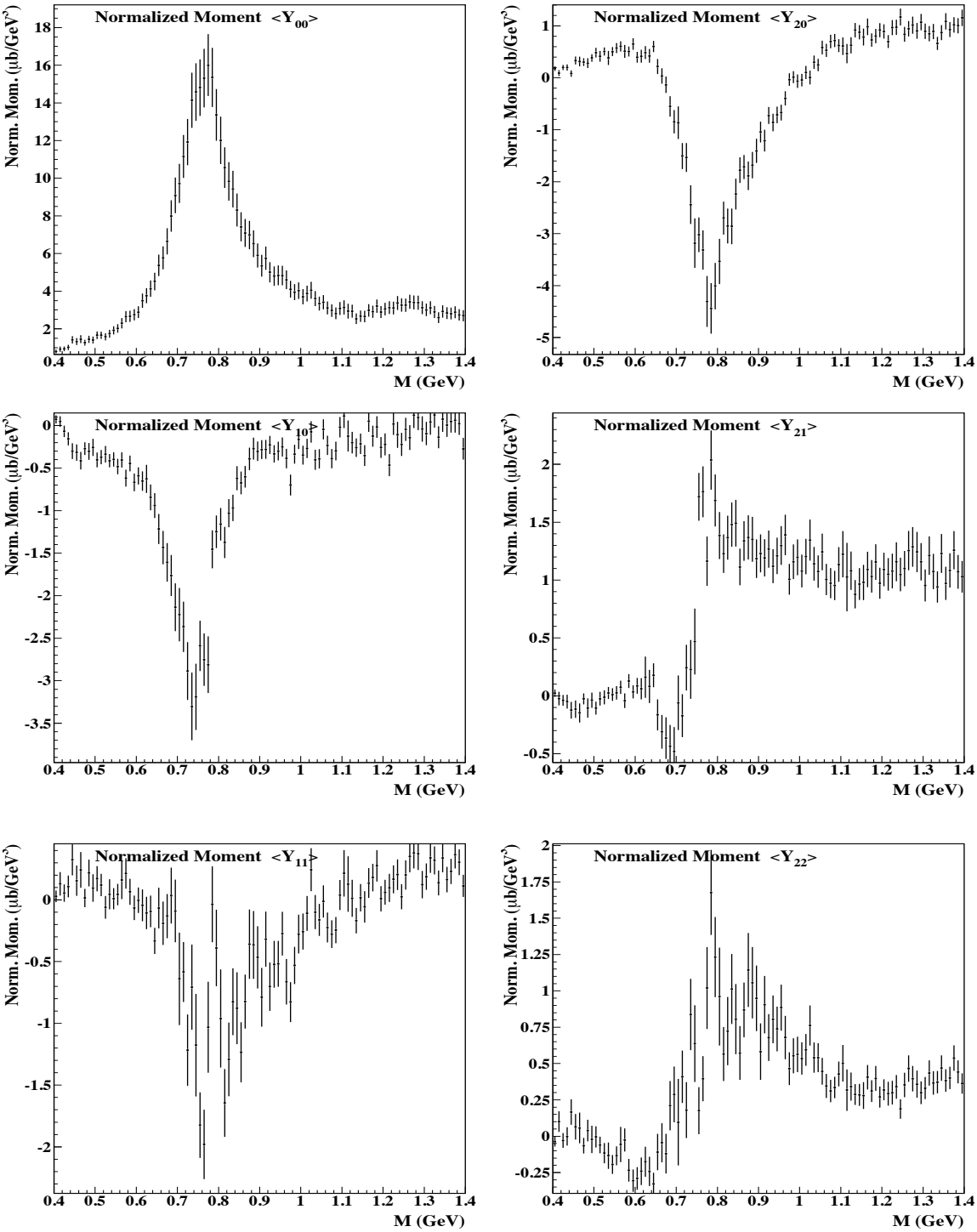

Figure 3.8: Normalized moments in $3.4 < E < 3.6$, $0.5 < -t < 0.6$ bins using the second method (parametrization with amplitudes). Errors include the systematic uncertainty on the absolute normalization and moment extraction procedure.

The parametrization in terms of the moments directly gives the quantities we are interested in (moments $\langle\tilde{Y}_{\lambda\mu}\rangle$). However the fit has to be restricted to make sure the intensity is positive. As in the previous case, a cutoff, λ_{max}, in the maximum number of moments has to be used. As shown in Appendix A as the number of angular momentum basis states (λ_{max}) is increased the moments with low λ, are unchanged and the fit simply starts populating higher moments. The implement the constraint on normalization of $\langle\tilde{Y}_{00}\rangle$ to the predicted number of events we follow Ref. [13] The relation between acceptance corrected I_{th} and measured distribution I_{data} is given by

$$I_{data}(\tau_a) = \eta(\tau_a) I_{th}(\tau_a) \tag{3.26}$$

The I_{th} and the acceptance function are expanded in the angular basis

$$\begin{aligned} I_{th}(\tau_a) &= \sqrt{4\pi}\sum_{\lambda\mu}\langle\tilde{Y}_{\lambda\mu}\rangle\ \mathrm{Re}Y_{\lambda\mu}(\Omega_\pi) \\ \eta(\tau_a) &= \sqrt{4\pi}\sum_{\lambda\mu}\eta_{\lambda\mu}\ \mathrm{Re}Y_{\lambda\mu}(\Omega_\pi) \end{aligned} \tag{3.27}$$

The normalization condition

$$4\pi\Delta N_{data}(i,j,k) = \int d\Omega_\pi I_{data}(\tau) \tag{3.28}$$

gives

$$\Delta N_{data}(i,j,k) = \sum_{\lambda\mu}\eta_{\lambda\mu}\epsilon_\lambda\langle\tilde{Y}_{\lambda\mu}\rangle \tag{3.29}$$

and enables to eliminate $\langle\tilde{Y}_{00}\rangle$

$$\langle\tilde{Y}_{00}\rangle = \frac{\Delta N_{data}(i,j,k)}{\eta_{00}} - \sum_{\lambda>0,\mu}\eta_{\lambda\mu}\epsilon_\lambda\langle\tilde{Y}_{\lambda\mu}\rangle \tag{3.30}$$

The expected (acceptance corrected) distribution is than given by:

$$I_{th}(\tau_a) = \sqrt{4\pi}\frac{\Delta N_{data}(i,j,k)}{\eta_{00}}Y_{00}(\Omega_\pi) + \sqrt{4\pi}\sum_{\lambda>0,\mu}\left[\ \mathrm{Re}Y_{\lambda\mu}(\Omega_\pi) - \frac{\eta_{\lambda\mu}}{\eta_{00}}\epsilon_0 Y_{00}(\Omega_\pi)\right]\langle\tilde{Y}_{\lambda\mu}\rangle \tag{3.31}$$

The function to be minimized with respect to $\langle\tilde{Y}_{\lambda\mu}\rangle$ ($\lambda > 0$) is than given by

$$-2\ln\mathcal{L} = -2\sum_{a=1}^{\Delta N_{data}(i,j,k)}\ln I_{th}(\tau_a) \tag{3.32}$$

with the coefficients $\eta_{\lambda\mu}$ computed using the accepted MC events

$$\eta_{\lambda\mu}(i,j,k) = \frac{\sqrt{4\pi}}{\Delta N_{gen.}(i,j,k)}\sum_{i}^{\Delta N_{rec.}(i,j,k)}\frac{\mathrm{Re}Y_{\lambda\mu}(\Omega_i)}{\epsilon_\lambda} \tag{3.33}$$

The plot of the normalized moments with $\lambda_{max} = 4.$ in shown in Fig. 3.9. Results are similar to what obtained with the second method showing the same stability against l_{max} truncation and a similar goodness of the fit (see fig. A.9 in Appendix A).

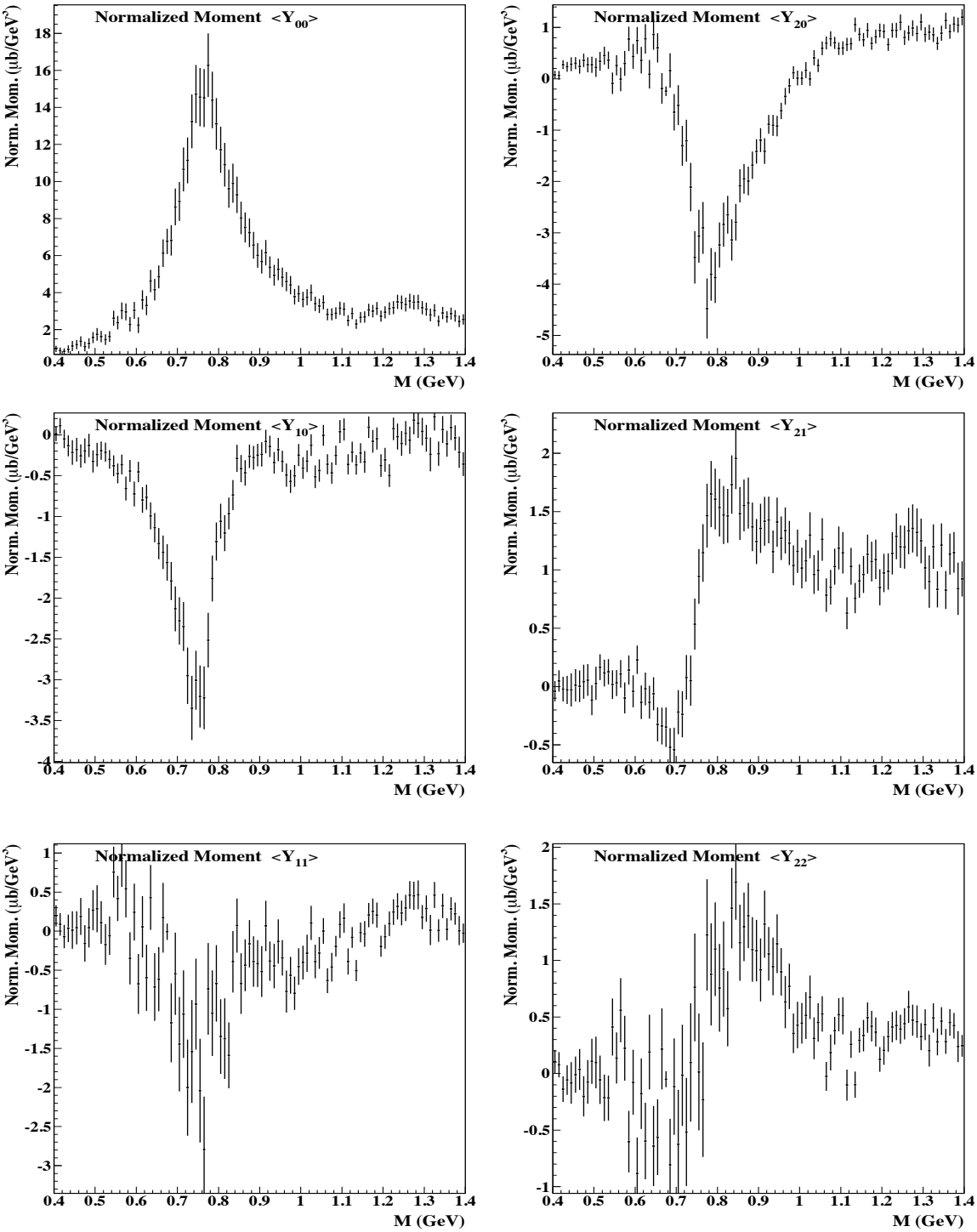

Figure 3.9: Normalized moments in $3.4 < E < 3.6$, $0.5 < -t < 0.6$ bins using the third method (parametrization with moments). Errors include the systematic uncertainty on the absolute normalization and moment extraction procedure.

3.2.5 Method comparison and final results

Figures 3.10 and 3.11 show the superposition of the moments extracted by using the three methods. From these, we conclude that qualitatively they all lead the same results. Moments with $\mu \neq 0$ are less stable then μ=0, reflecting the azimuthal anisotropy of the CLAS detector. Out of the three methods the most stable results are obtained by using log-likelihood fit with the parametrization with amplitudes although we do find occasionally large bin-to-bin fluctuations. Moreover for the third method the likelihood fit was performed initiating parameters in three different ways (see Appendix A for more details). Therefore the final results will be given as the average of the second (parametrization with amplitudes) and the third method (parametrization with moments) with the three fit initializations:

$$Y_{final} = \sum_{i=1,4\,Methods} \frac{Y_i}{4} \tag{3.34}$$

$$\tag{3.35}$$

The total error on the final moments was evaluated adding in quadrature the statistical error, δ_{MINUIT} as given by MINUIT, and two systematic error contributions: $\delta Y_{syst\ fit}$ related to the moment extraction procedure, and $\delta Y_{syst\ norm}$, the systematic error associated to the photon flux normalization.

$$\delta Y_{final} = \sqrt{\delta^2_{MINUIT} + \delta^2_{syst\ fit} + \delta^2_{syst\ norm}} \tag{3.36}$$

with:

$$\delta Y_{syst\ fit} = \sqrt{\sum_{i=1,4\,Methods} \frac{(Y_i - Y_{final})^2}{3}} \tag{3.37}$$

$$\delta Y_{syst\ norm} = 10\% \cdot Y_{final} \tag{3.38}$$

$$\tag{3.39}$$

For the most part of the data points, systematic incertainties dominate over the statistical error. A sample of final experimental moments are shown in figures 3.12 and 3.13 .

3.3 The $\gamma p \to p\rho^0$ cross section

To check the whole procedure, in this paragraph we compare the results of the 'standard' analysis presented in Chap. 2.3 with what obtained by the angular moment analysis (method 3) described in this Chapter. As pointed out in the previous paragraph, the $\langle Y_{00} \rangle$ moment can be directly connected to the differential cross section. In the ρ region this can also be written as:

$$\frac{d\sigma}{dtdM} = \frac{2}{\pi}\left[\frac{d\sigma}{dt}\right]_\rho \frac{m_\rho M\Gamma(M)}{(m_\rho^2 - M^2)^2 + m_\rho^2\Gamma^2(M)} + polynomial \tag{3.40}$$

and

$$\Gamma(M) = \Gamma_\rho \left(\frac{q}{q_\rho}\right)^3 \frac{D_2(q_\rho R)}{D_2(qR)} = \Gamma_\rho \left(\frac{q}{q_\rho}\right)^3 \frac{(q_\rho R)^2 + 1}{(qR)^2 + 1} \tag{3.41}$$

where $R = 1/0.2GeV$ and the background under the prominent ρ peak is described by a first order polynomial $(A^2 + B^2 M)$.

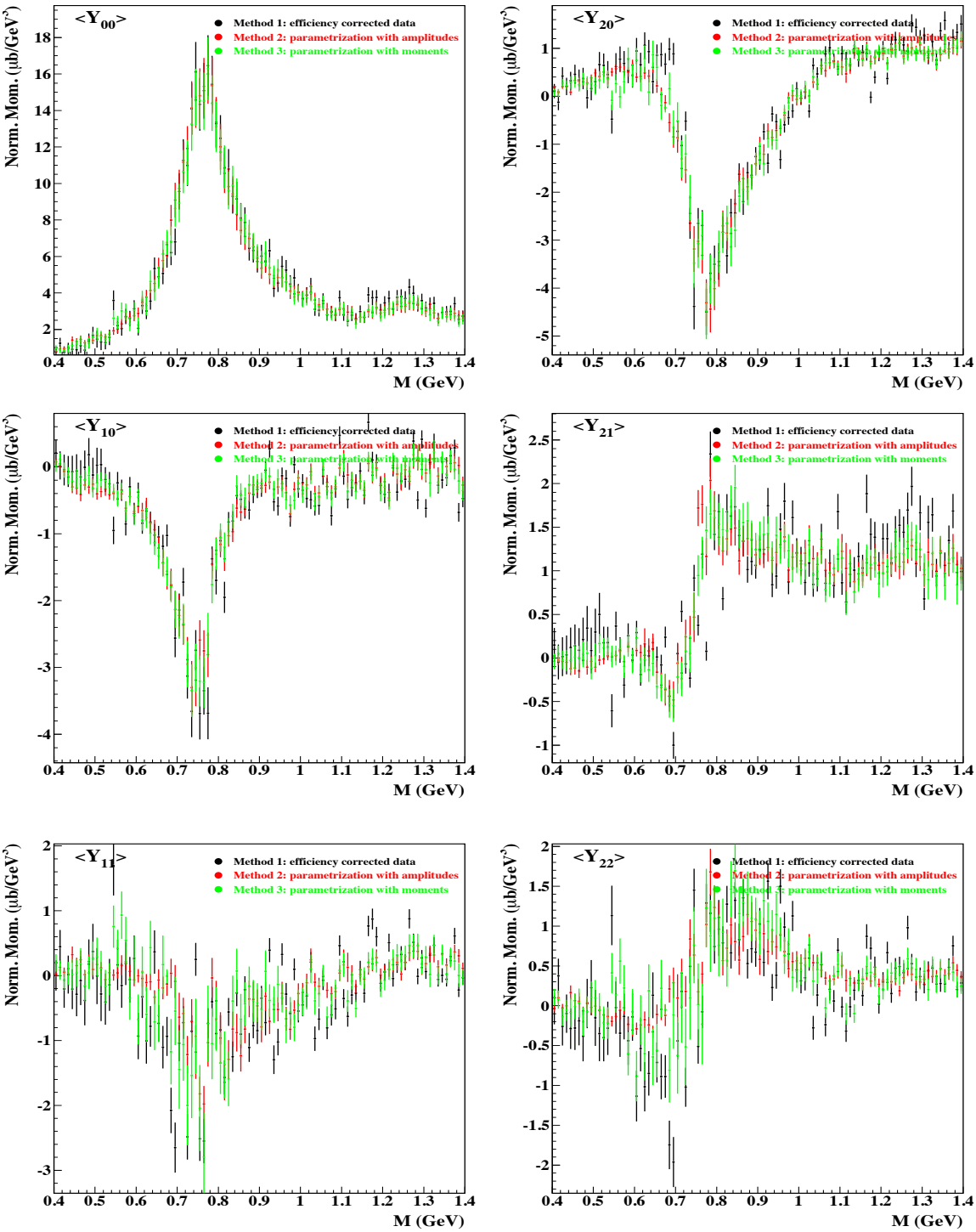

Figure 3.10: Comparison of normalized moments in $3.4 < E < 3.6$ GeV and $0.5 < -t < 0.6\text{GeV}^2$ bins, obtained by the three methods: efficiency corrected data (black), parametrization with amplitudes (red) and parametrization with moments (green). Errors include the systematic uncertainty on the absolute normalization and moment extraction procedure.

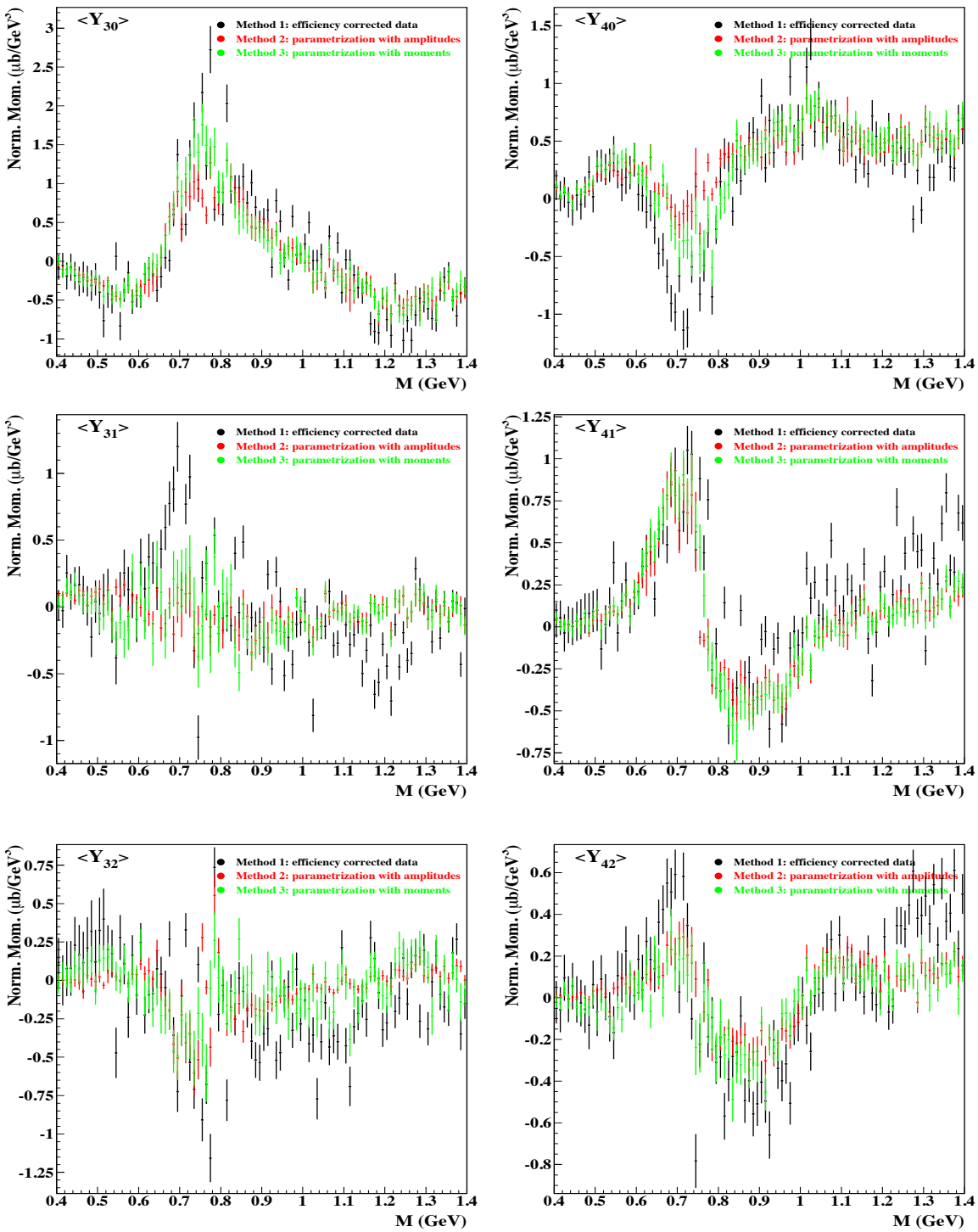

Figure 3.11: Comparison of normalized moments in $3.4 < E < 3.6$ GeV and $0.5 < -t < 0.6$ GeV^2 bins, obtained by the three methods: efficiency corrected data (black), parametrization with amplitudes (red) and parametrization with moments (green).

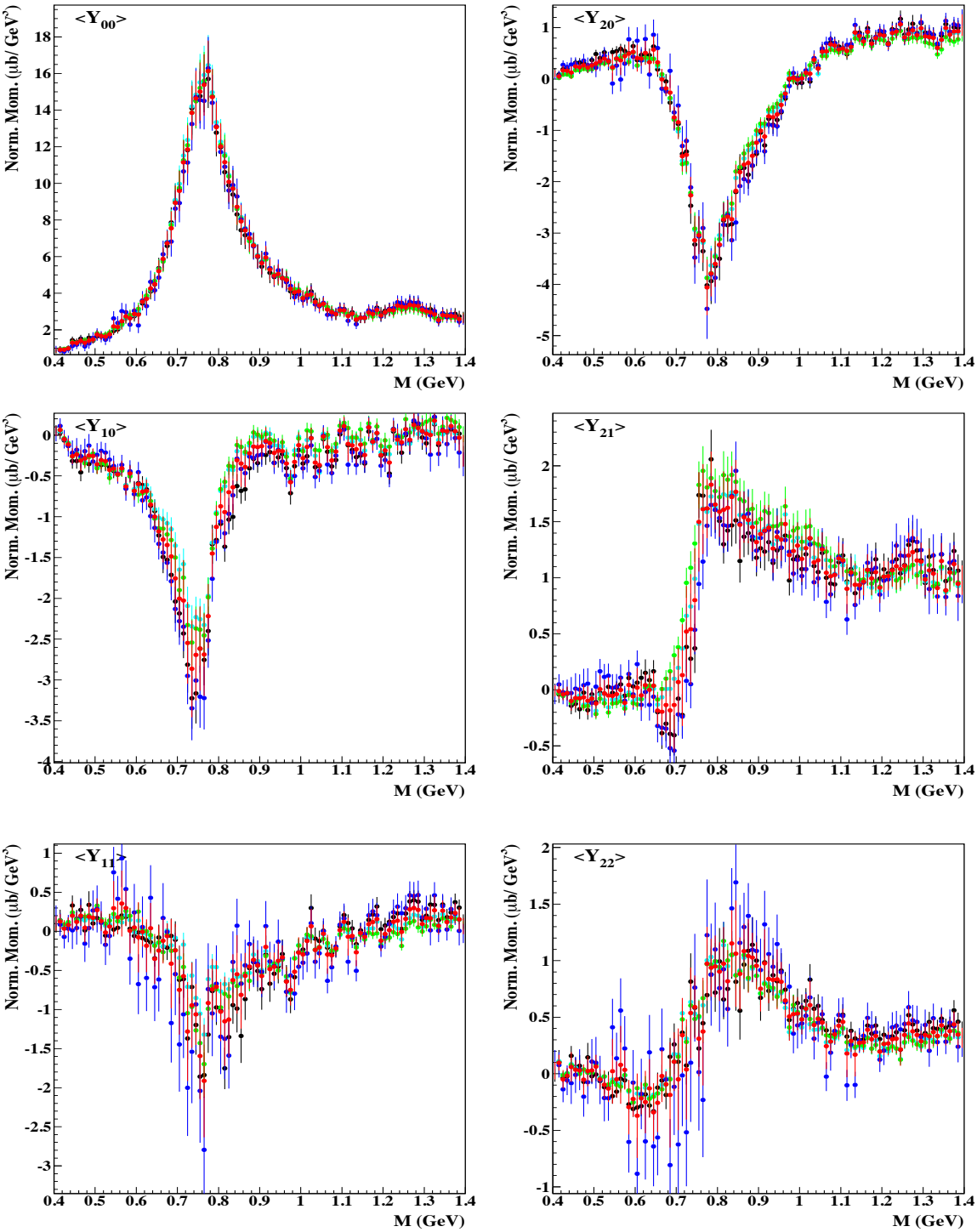

Figure 3.12: Final experimental moments (in red) in $3.4 < E < 3.6$ GeV and $0.5 < -t < 0.6$ GeV^2 bins as average of different extraction methods.

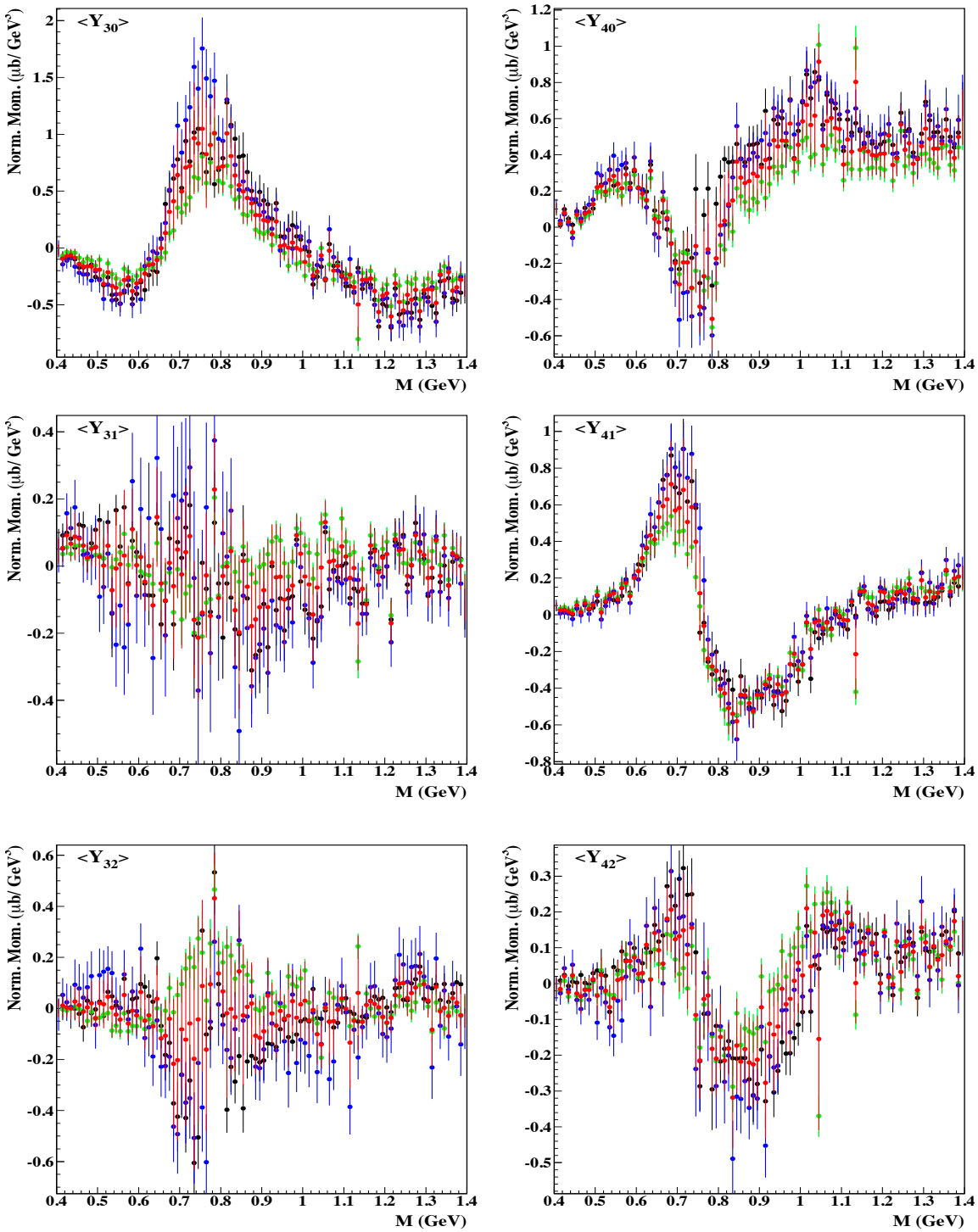

Figure 3.13: Final experimental moments (in red) in $3.4 < E < 3.6$ GeV and $0.5 < -t < 0.6$ GeV^2 bins as average of different extraction methods.

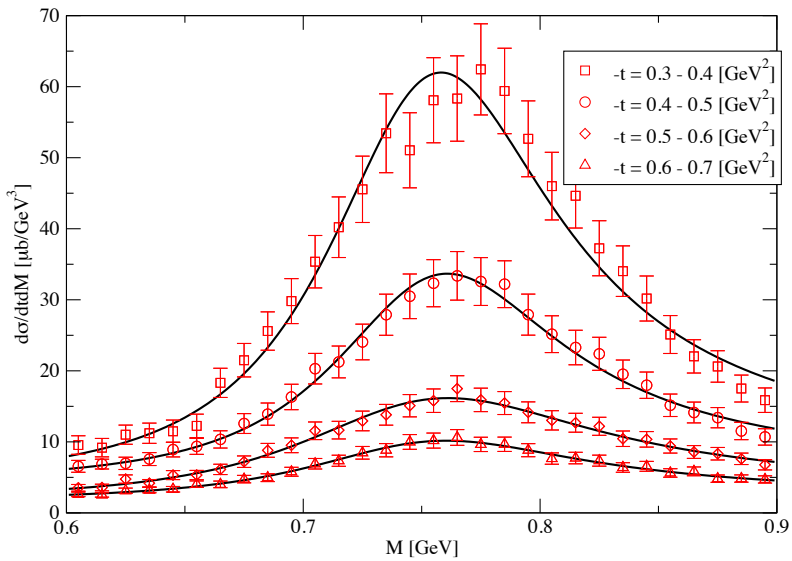

Figure 3.14: Fit of the mass dependence of the $\langle Y_{00} \rangle$ moment in the mass range $0.6 < M < 0.9$ GeV and $E = 3.2 - 3.4$.

In each energy and $-t$ bin, the mass dependence of the differential cross section obtained from the $\langle Y_{00} \rangle$ moment was fit to extract $\left[\frac{d\sigma}{dt}\right]_\rho$. The parameters of the fit were: $\Gamma_\rho, m_\rho, A, B$ and $\left[\frac{d\sigma}{dt}\right]_\rho$. Figure 3.14 shows examples of the fit results for the mass range $0.6 < M < 0.9$ GeV and $E = 3.2 - 3.4$.

In Figs. 3.15 we show the variations of mass and width across the t-bins. The extracted mass of the ρ meson, is systematically lower than the nominal (by $10 - 20$ MeV) this is due to lack of interference effects, in particular with the S-wave in the fitting function and will be taken into account in the analysis of partial waves discussed in the next Chapter.

The extracted cross section for the four energy bins is shown in Fig. 3.16 in comparison with results obtained by the 'standard' analysis as well as the world data.
This result was obtained applying the standard technique to separate a prominent signal from the background (Breit-Wigner fit). It can not be applied to other mesons populating the $\pi\pi$ spectrum ($f_0(980)$ and $f_2(1270)$) since their strength is not big enough and the model dependence in parameterizing the background does not allow to derive reliable results. In the next Chapter we'll derive again the cross section of the ρ, as well as for the other mesons dominating the single waves of the $\pi\pi$ system by implementing the full partial wave analysis.

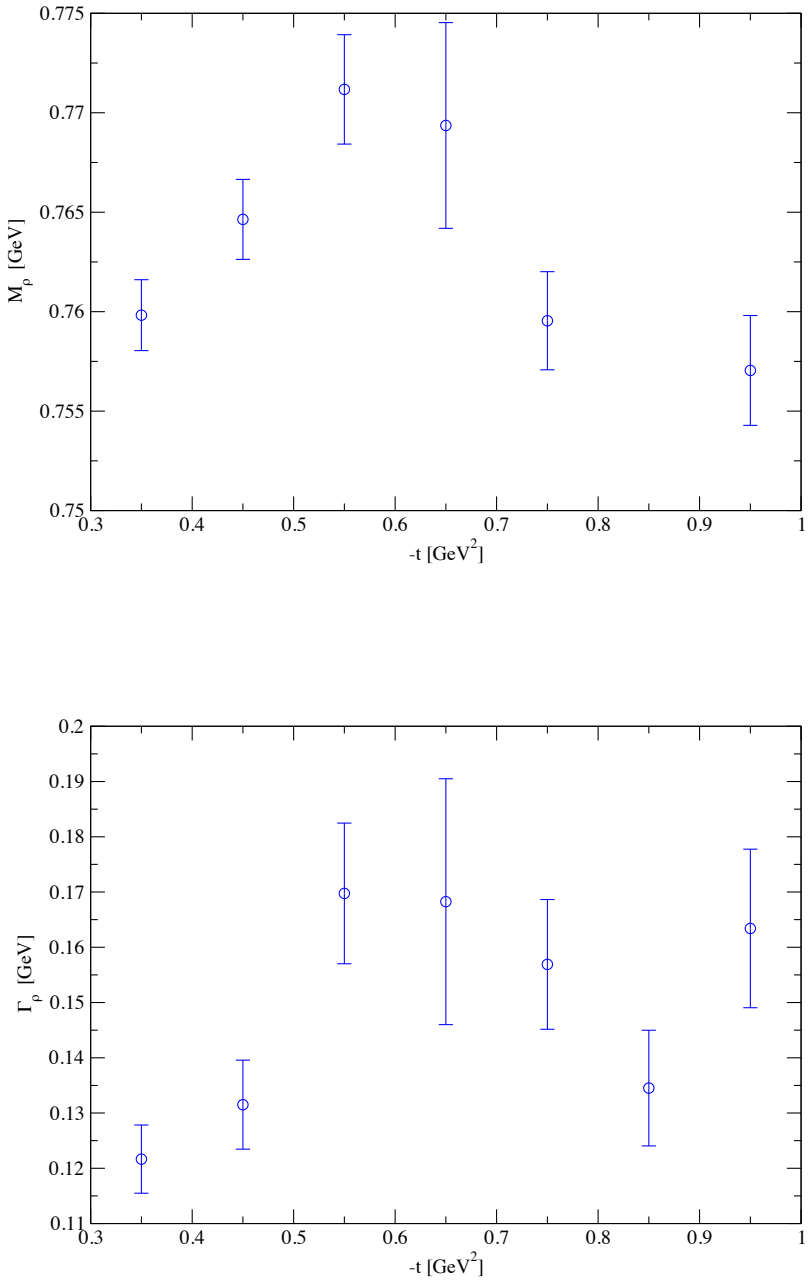

Figure 3.15: Fitted values of m_ρ and Γ_ρ as a function of $-t$.

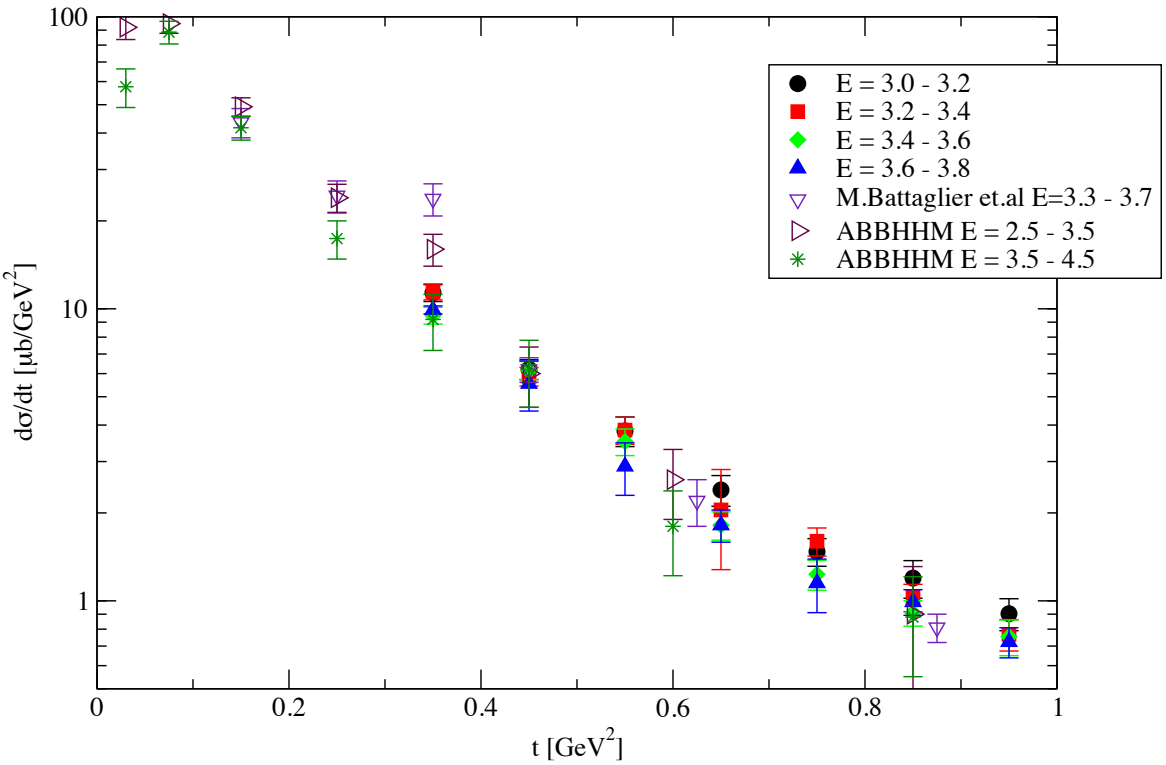

Figure 3.16: Differential cross section for the reaction $\gamma p \rightarrow p\rho$ extracted from the analysis of the angular moments compared to world data.

Chapter 4

Theoretical interpretation

4.1 Introduction

The spectroscopy of scalar mesons is a field of active investigations both on experimental and theoretical sides. Scalar mesons have been observed in hadron-hadron collisions, $\gamma\gamma$ collisions and in decays of various mesons like $\phi, J/\Psi, D$ and B. Their photoproduction cross sections are relatively small as compared to the dominant production of vector mesons. One can extract, however, an information about the S-wave strength in photoproduction processes by performing the partial wave analysis. An interference between the S-wave and the dominant P-wave was discovered in studies of the K^+K^- photoproduction on hydrogen in experiments performed at DESY [9] and Daresbury [10]. The moments of the angular distribution of the photoproduced K^+K^- system obtained in these two experiments contained the information about the S-P wave interference. Using this information the authors of [11] were able to extract the S-wave photoproduction cross section near the K^+K^- threshold. In the present analysis we focus on $\pi^+\pi^-$ photoproduction at photon energies between 3.2 GeV and 3.8 GeV in the range of momentum transfer squared $-t$ between 0.1 GeV^2 and 1 GeV^2 whereas the $\pi^+\pi^-$ effective mass $M_{\pi\pi}$ varies from 0.4 GeV to 1.4 GeV. We are not aware of any previous sightings of scalars in particular $f_0(980)$ in photo-production of pion pairs.

This effective mass region is dominated by the production of the $\rho(770)$ resonance in the P-wave. One can learn, however, from other experiments like pion-nucleon collisions $\pi^-p \to \pi^+\pi^-n$ [13, 14] or nucleon-antinucleon annihilation [15] that in the $\pi\pi$ system the S-wave resonant states can also be formed. These resonances have been neglected in previous experimental analyses of photoproduction and to our knowledge the current analysis is the first one which explicitly takes into account the possibility that the S-wave is produced in the $\pi^+\pi^-$ system. The production of the S-wave results in the emergence of the interference patterns. Former experiments at SLAC [16, 17] and DESY [18, 19] revealed some phenomena accompanying the ρ resonance photoproduction. Among the observed characteristics of this reaction were a shift of the maximum of the $\pi^+\pi^-$ effective mass distribution with respect to the nominal ρ mass and the shape asymmetry as compared to the Breit-Wigner distribution. Moreover, a diffractive nature of the photoproduction process and the shrinkage of the diffractive peak with growing photon energies were observed. It has been shown that while the s-channel helicity is approximately conserved, some deviations are seen, especially at larger effective masses $M_{\pi\pi}$ and larger momentum transfers squared $|t|$. The shift of the mass distribution maximum as compared to the ρ position observed in the hadronic collisions and the asymmetry mentioned above were quite successfully described in terms of the model formulated by Söding [20] and its numerous modifications [21, 22, 23, 24]. In the Söding model these properties are attributed to the interference of the dominating ρ meson production (with its subsequent decay into $\pi^+\pi^-$) described in terms of the Breit-Wigner amplitude and the t-channel pomeron exchange with the amplitudes corresponding to the Drell-type diagrams in which the photon dissociates into

π^+ and π^- and one of the pions is elastically scattered off the proton. This simple picture is somehow distorted by additional production mechanisms namely the s-channel production of baryon resonances Δ^{++} and Δ^0. However, from works [16, 18, 19] as well as from more recent experimental studies, one can infer that the production of baryon resonances dominates at lower incident photon laboratory energies (below 2 GeV). In particular, the data obtained with SAPHIR detector at ELSA for laboratory photon energies between 0.5 GeV and 2.6 GeV show that the contribution of the baryonic resonances to the π^+p and π^-p mass distributions gradually decreases with photon energy [25].

The angular distribution of photoproduced mesons and the observables derived from it like moments of the angular distribution $\langle Y_{LM}\rangle$ and the density matrix elements $\rho^{LL'}_{MM'}$[1] are the best to look for interference patterns. In experiments [16, 17, 18] these observables have been used to analyze the properties of helicity amplitudes describing the photoproduction process. Unfortunately only the dominant spin 1 partial wave of the $\pi^+\pi^-$ pair has been taken into account. No attempt has been made to obtain information about the S-wave amplitude.

More recently, the HERMES group at DESY [26] investigated the interference of the P-wave in the $\pi^+\pi^-$ system with the S- and D-waves in the $\pi^+\pi^-$ electroproduction process showing that such interference effects are measurable. The large photon virtuality Q^2 >3 GeV^2 is, however, a crucial factor which distinguishes this analysis from the photoproduction one.

Theoretical models for the $\pi^+\pi^-$ photoproduction have been investigated in a series of articles. Gomez Tejedor and Oset [28] applied the effective Lagrangian's to construct the photoproduction amplitudes. Their approach, however, is limited to quite low photon energies of 800 MeV and effective masses $M_{\pi\pi}$ smaller than 1 GeV. The model proposed in [27] pursues a two stage approach for the $\pi^+\pi^-$ S-wave photoproduction. First, a set of Born amplitudes is calculated corresponding to photoproduction of the $\pi^+\pi^-$, $\pi^0\pi^0$, K^+K^- and $K^0\overline{K^0}$ pairs. Then the photoproduced meson pairs are subject to the final state interactions to end up with the $\pi^+\pi^-$ system. The Born amplitudes were calculated with two kinds of propagators, namely the normal and Regge type ones. The final state interactions have been parameterized in terms of phase shifts and inelasticities with an application of the coupled channel formalism developed in articles [29, 30, 31]. The coupled channel calculations were separately performed for all isospin I components of the transition matrix, i.e. for I=0 and 1 in case of kaons and I=0 and 2 in case of pions. Thus the S-wave amplitudes in that model can account for the existence of the isoscalar σ, $f_0(980)$ and $f_0(1500)$ and the isovector $a_0(980)$ and $a_0(1450)$ resonances. The coupling of the $K\overline{K}$ isovector channel with the $\pi\eta$ amplitude is described in [32].

One remark is relevant here. Each complete analysis of the $\pi^+\pi^-$ photoproduction should include the S-wave amplitudes in addition to the P-wave. This results in the appearance of additional moments of angular distribution and new density matrix elements. In this analysis we focus on these new elements.

4.2 Partial Wave Analysis

In the Chapter 3 we discussed how moments of the angular distribution of the $\pi^+\pi^-$ system, Y_{LM} were extracted from the data in each bin in photon energy, momentum transfer and di-pion mass. The moments can be written in terms of amplitudes representing di-pion production. In this section we summarize results of theoretical analysis of these amplitudes.

As reported in the previous Chapter, the production cross section is directly related to $\langle Y_{00}\rangle$ moment:

$$\frac{d\sigma}{dtdM} = \int d^2\Omega \frac{d\sigma}{dtdMd^2\Omega} = \langle Y_{00}\rangle \tag{4.1}$$

[1] In this section we switch to a standard notation of angular momentum variables, L, M instead of λ, μ used in the previous Chapter.

while higher moments correspond to:

$$\langle Y_{LM}\rangle = \sqrt{4\pi}\int d^2\Omega Y_{LM}(\Omega)\frac{d\sigma}{dtdMd^2\Omega} \tag{4.2}$$

The differential cross-section for di-pion production, in units of $\mu b/0.1GeV^2 10MeV$ used in Chapter 3 can be written as:

$$\frac{d\sigma}{dtdMd^2\Omega} = \frac{0.3893}{64\pi m_N^2 E_\gamma^2}\frac{\kappa}{2(2\pi)^3}\frac{1}{4}\sum_{\lambda,\lambda'\lambda_\gamma}|A(\lambda,\lambda',\lambda_\gamma,E_\gamma,t,M,\Omega)|^2 \tag{4.3}$$

where all dimension-full quantities given in units of GeV. The di-pion phase space factor is proportional to the breakup momentum $\kappa = \sqrt{M^2/4 - m_\pi^2}$. In terms of partial waves the di-pion production amplitudes A are given by

$$A(\lambda,\lambda',\lambda_\gamma,E_\gamma,t,M,\Omega) = \sum_{lm} a_{lm}(\lambda,\lambda',\lambda_\gamma,E_\gamma,t,M)Y_{lm}(\Omega) \tag{4.4}$$

which leads to the following expression for the moments

$$\begin{aligned}\langle Y_{LM}\rangle &= N\sum_{l'm',lm}(-1)^{m'}\sqrt{\frac{(2l+1)(2l'+1)}{2L+1}}\langle lm,l'-m'|L-M\rangle\langle l0,l'0|L0\rangle \\ &\times \frac{1}{2}\sum_{\lambda,\lambda',\lambda_\gamma} a_{lm}(\lambda,\lambda',\lambda_\gamma,E_\gamma,t,M)a^*_{l'm'}(\lambda,\lambda',\lambda_\gamma,E_\gamma,t,M)\end{aligned} \tag{4.5}$$

where N is the phase space factor. Parity conservation implies

$$a_{lm}(\lambda,\lambda',\lambda_\gamma,E,t,M) = (-1)^{\lambda-\lambda'+\lambda_\gamma+m}a_{l,-m}(-\lambda,-\lambda',-\lambda_\gamma,E,t,M) \tag{4.6}$$

which leads to

$$\begin{aligned}\langle Y_{LM}\rangle &= N\sum_{l'm',lm}(-1)^{m'}\sqrt{\frac{(2l+1)(2l'+1)}{2L+1}}\langle l0,l'0|L0\rangle \\ &\times\frac{1}{2}\left[\langle lm,l'-m'|L-M\rangle + (-1)^M\langle lm,l'-m'|LM\rangle\right]a_{lm}a^*_{l'm'}\end{aligned} \tag{4.7}$$

with the helicity amplitudes involving only the $\lambda_\gamma = +1$ states,

$$a_{lm}a^*_{l'm'} = \sum_{\lambda,\lambda'} a_{lm}(\lambda,\lambda',\lambda_\gamma=+1,E_\gamma,t,M)a^*_{l'm'}(\lambda,\lambda'\lambda_\gamma=+1,E_\gamma,t,M) \tag{4.8}$$

Thus parity implies

$$\langle Y_{LM}\rangle = (-1)^M\langle Y_{L-M}\rangle \tag{4.9}$$

which together with the $Y^*_{LM} = (-1)^M Y_{L-M}$ property of the spherical harmonics also implies that moments are real. The explicit forms of the moments investigated here, with $l = 0(S), 1(P), 2(D), 3(F)$ waves are given in Appendix B.

4.2.1 Parametrization of the partial waves

The role of the nucleon helicity

In each energy and momentum transfer and for each l, m there are four independent partial wave amplitudes for given l, m that are functions of $s = M^2$,

$$a_{lm} = a_{lm}(\lambda,\lambda',\lambda_\gamma=+1,s) \tag{4.10}$$

corresponding to the four combinations of initial and final nucleon helicity. In general it is expected that dominant amplitudes require minimal photon helicity flip, *i.e.*

$$|a_{l1}| > |a_{l0}|, |a_{l2}| > |a_{l-1}| \tag{4.11}$$

corresponding to photon helicity flip by zero, one and two units respectively. In addition, $m = 2$ waves require $l \geq 2$ (D and F waves) which are expected to be small in the mass range considered. We thus restrict the analysis to $|m| \leq 1$.

Without polarization information it is difficult to separate out amplitudes differing by the helicity of the nucleon. The interference between the dominant P waves, in the ρ region seen in the $\langle Y_{21} \rangle$ moments indicates that P_+ and P_0 amplitudes are out of phase. For a single nucleon-helicity amplitude this would imply a difference between the $\langle Y_{11} \rangle$ and $\langle Y_{10} \rangle$ moments, arising primarily from the interference between the S wave and the P_+ and P_0 waves, respectively in the ρ region where the S amplitude does not vary substantially. The data suggests however that both $\langle Y_{11} \rangle$ and $\langle Y_{10} \rangle$ peak near the position of the ρ. To accommodate such behavior at least two nucleon-helicity amplitudes are required.
For example the dominant P_+ amplitude may originate from diffractive, helicity-non-flip amplitude and the P_0 from a nucleon-helicity-flip vector exchange, which is also expected to dominate S-wave production. This would also explains why $\langle Y_{11} \rangle$ and $\langle Y_{10} \rangle$ moments have comparable magnitudes. We will thus keep two nucleon helicity amplitudes.

According to that, the complete set of amplitudes that will be fitted to the moments, in each E_γ and t bin, is given by

$$a_{l,m,i}(s) = a_{lm}(\lambda, \lambda', \lambda_\gamma, s) \tag{4.12}$$

with $i = 1, 2$ for each l, m and $|m| \leq 1$. The two nucleon helicity amplitudes are assumed to correspond to helicity non-flip ($i = 1$) and helicity-flip ($i = 2$).

Analytic properties of amplitudes

Since strong interactions conserve isospin it is convenient to write the $\pi\pi$ amplitudes in the isospin basis. We will use Greek indices to denote the various channels that couple to $\pi\pi$ of given isospin, I in the partial wave l, *e.g.* $\alpha = 1$ corresponds to $\pi\pi$, $\alpha = 2$ to $K\bar{K}$, $\alpha = 3$ to $\eta\eta$ etc. In the subsequent analysis we will restrict the channel space to include the $\pi\pi$ and $K\bar{K}$ channels which are the only channels relevant in the energy range considered. As a function of s partial wave amplitudes have cuts for $s > 4m_\pi^2$ (right hand cut) and for $s < m_\pi^2$ (left hand cut). The right hand cut corresponds to particle production threshold in the reaction $\gamma p \to Xp$ and the left hand cut originates from thresholds in crossed channels (*e.g.* $\pi^- p \to \gamma\pi^- p$). Since thresholds in $\gamma p \to Xp$ are the same as for $\pi^+\pi^- \to \pi^+\pi^-$ the right hand cut discontinuity of $a_{lm,i}(s)$ is the same as for the corresponding $\pi\pi$ scattering amplitude. Optical theorem states that partial wave photo-production amplitudes of good isospin $a^I_{l,m,i,\alpha}(s)$ have discontinuities for positive s proportional to those of the strong interactions scattering amplitudes,

$$a^I_{l,m,i,\alpha}(s^+) - a_{l,m,i,\alpha}(s^-) = -2i \sum_\beta \left[t(s^+)\right]_{\alpha\beta} \rho_{\beta\beta}(s) a^I_{l,m,i,\beta}(s^-) \tag{4.13}$$

Here $t_{\alpha\beta}(s) = t^{l.I}(s)_{\alpha\beta}$ is the scattering amplitude between channels α and β in the l, I partial wave and $\rho(s)_{\alpha\beta} = k_\beta/8\pi\sqrt{s} = \sigma_\beta(s)/16\pi$ is the phase space factor with $\sigma_\beta = \sqrt{1 - 4m_\beta^2/s}$. In the following we will hide the channel index and write equations in a matrix notation in the channel space. We will also drop the indices l, I denoting partial waves and the nucleon helicity label i since these are not mixed by the interactions in the $\pi\pi$ system. Subsequently we define amplitudes $\tilde{a}$ by removing threshold behavior, $\tilde{a} \equiv [k]^{-l} a$ where $[k] = [k]_{\alpha,\beta} = k_\alpha/\sqrt{s}\delta_{\alpha,\beta}$. The new amplitudes satisfy

$$\tilde{a}(s^+) - \tilde{a}(s^-) = -2i[k]^{-l} t(s^+) \rho(s) [k]^l \tilde{a}(s^-) \tag{4.14}$$

For each partial wave (l, m, i) we introduce a function $\tilde{a}^L(s)$ that has the same discontinuity across the left hand cut as the photo-production amplitude $\tilde{a}(s)$, *i.e*

$$\tilde{a}(-s - i\epsilon) - \tilde{a}(-s + i\epsilon) = \tilde{a}^L(-s - i\epsilon) - \tilde{a}^L(-s + i\epsilon) \tag{4.15}$$

but has not right hand cut discontinuity, *i.e.*

$$\tilde{a}^L(s + i\epsilon) - \tilde{a}^L(s - i\epsilon) = 0 \tag{4.16}$$

We also express the scattering amplitudes $t(s)$ as a ratio of two functions (matrices in channel space) $N(s)$ which as only discontinuities for negative s and $D(s)$ which has the discontinuity for positive s that are determined by unitarity,

$$t = [D(s)]^{-1} N(s) \tag{4.17}$$

Finally we define the function,

$$T(s) \equiv D(s) \equiv D(s) [k]^l \left[\tilde{a}(s) - \tilde{a}^L(s)\right] \tag{4.18}$$

From the properties of $\tilde{a}$ and $\tilde{a}^L$ it follows that T has only right hand cut (positive s) discontinuity which is given by,

$$T(s^+) - T(s^-) = -[D(s^+) - D(s^-)][k]^l \tilde{a}^L(s) = -2iN(s)\rho(s)[k]^l \tilde{a}^L(s) \tag{4.19}$$

The last relation follows from unitarity which relates the positive-s discontinuity of $D(s)$ to the scattering amplitude,

$$D(s^+) - D(s^-) = 2iN(s)\rho(s) = 2iD(s^+)t(s)\rho(s) \tag{4.20}$$

Further discussion of the unitarity constraints and properties of $D(s)$ and $N(s)$ functions is presented in the Appendix. Using Cauchy theorem it is now possible to write the following dispersion relation for the photoproduction amplitude which include integration over the positive-s only,

$$\tilde{a}(s) = \tilde{a}^L(s) - \frac{1}{\pi}[k]^{-l} D^{-1}(s) \int_{s_{th}} ds' \frac{N(s')\rho(s')[k']^l \tilde{a}^L(s')}{s' - s} \tag{4.21}$$

and finally

$$\begin{aligned} a(s) &= a^L(s) - \frac{1}{\pi} D^{-1}(s) \int_{s_{th}} ds' \frac{N(s')\rho(s')[k']^l \tilde{a}^L(s')}{s' - s} \\ &= a^L(s) - \frac{1}{\pi} D^{-1}(s) \int_{s_{th}} ds' \frac{N(s')\rho(s') a^L(s')}{s' - s} \end{aligned} \tag{4.22}$$

The amplitudes $\tilde{a}^L(s)$ represent our ignorance about the production process and will be extracted by fitting this formula to the acceptance corrected moments. Relation between moments and the partial waves $a(s) = a_{l,I,i,\pi\pi}$ is given in the Appendix. The important fact about the functions $\tilde{a}^L$ is that they do not have singularities for positive s thus can be expanded in a Taylor series for $s > 0$

$$\tilde{a}^L(s) = \mathcal{A} + \mathcal{B}s + \mathcal{C}s^2 + \cdots \tag{4.23}$$

with $\mathcal{A}, \mathcal{B} \cdots$ being matrix of numerical coefficients to be determined by the fit. This expansion has another physical significance. Suppose $\tilde{a}^L(s)$ has a pole at negative s, $s = -M^2$. Physically it would correspond to an exchange of a particle of mass M in the t channel of the $\pi\pi$ system [2]. For $s > 0$,

$$\tilde{a}^L(s) = \frac{1}{s + M^2} = \frac{1}{M^2}\left[1 - \frac{s}{M^2} + \frac{s^2}{M^4} \cdots\right] \tag{4.24}$$

[2] To be more precise if a mass-M particle is exchanged in the t-channel and s-wave partial wave has a cur rather than a pole for negative-s

thus the magnitude of the coefficients $\mathcal{A}, \mathcal{B}, \cdots$ is related to mass of the exchanged particle in the t channel thus to the physical size of the production region. Further insight into the production process can be inferred by comparing the contribution from the real and imaginary parts of the dispersive integral in Eq. 4.22. These are obtained using

$$\frac{1}{s'-s} = PV\frac{1}{s'-s} + i\pi\delta(s'-s) \tag{4.25}$$

to obtain

$$a(s) = \frac{1}{2}\left[I + S(s)\right]a^L(s) - \frac{1}{\pi}D^{-1}(s)PV\int_{s_{th}} ds'\frac{N(s')\rho(s')a^L(s')}{s'-s} \tag{4.26}$$

Here $S = S_{\alpha\beta}$ is the S-matrix elements between channels $\alpha\beta$ and $I = \delta_{\alpha\beta}$ is the identity matrix in the channel space. The term containing the S-matrix corresponds to the contribution from the on-shell scattering: it represents direct production of $\pi\pi$ or $K\bar{K}$ pairs which later (via S) re-scatter to the final $\pi^+\pi^-$ state. Direct resonance production in the s-channel is described by the principal value (PV) part of the integral. However, resonance contribution can also appears in the on-shell scattering term via re-scattering (or final state interaction). Thus when extracting cross-section for direct resonance production we will only use the PV contribution to the partial wave, even though it is the full expression in Eq. A.3 that is used in fitting the moments.

Using a polynomial expansion for $\tilde{a}^L$ the dispersion relation in Eq. 4.22 has to be subtracted. The specific forms of dispersion relations for individual partial waves and the count of the fit parameters for each partial wave are summarized in the Appendix.

4.3 Results and error evaluation

4.3.1 Fit of the moments

We fit all moments $\langle Y_{LM}\rangle$ with $L < 4$ and $M < 2$ using up to $l = 3(F)$ waves as described above. In figures 4.1 and 4.2 we present a sample of the fit results for $E_\gamma = 3.3$ GeV ($3.2 - 3.4$ GeV energy bin) and t in the range $0.5 < |t| < 0.6$ GeV^2. To properly take into account the error contributions (statistical and systematic) to the experimental moments described in Sec. 3.2.5, the four sets of moments were individually fit and the fit results were averaged obtaining the central value shown by the black line in the figures. The error band, shown as a gray area, was calculated following the same procedure adopted for the experimental moments (Sec.. 3.2.5).

Error evaluation

The final error was computed as the sum in quadrature of the statistical error of the fit, and two systematic error contributions: the first related to the moment extraction procedure, evaluated as the variance of the four fit results; the second associated to the photon flux normalization estimated to be 10%. Central values and errors for all the observables of interest discussed in next sections were derived from the fit results with the same procedure.

4.3.2 Amplitudes

The square of the magnitude of S, P, D and F partial waves summed over nucleon helicities derived by the fit are shown in Fig. 4.3 for a specific energy and $-t$ bin. The three bottom plots show, for each wave with $L \neq 0$, the amplitudes for the three possible values of $\lambda_{\pi\pi}$, the helicity of the di-pion system. Note that we use, as a reference, the wave with photon helicity, $\lambda_\gamma = +1$. Thus $\lambda_{\pi\pi} = 1$ corresponds to no-helicity flip (s-channel helicity conserving) amplitude, which, as expected is the dominant one, and $\lambda_{\pi\pi} = 0, -1$ correspond to one and two units of helicity flip in the "upper" vertex, respectively. The top panel shows the magnitude of the sum of the

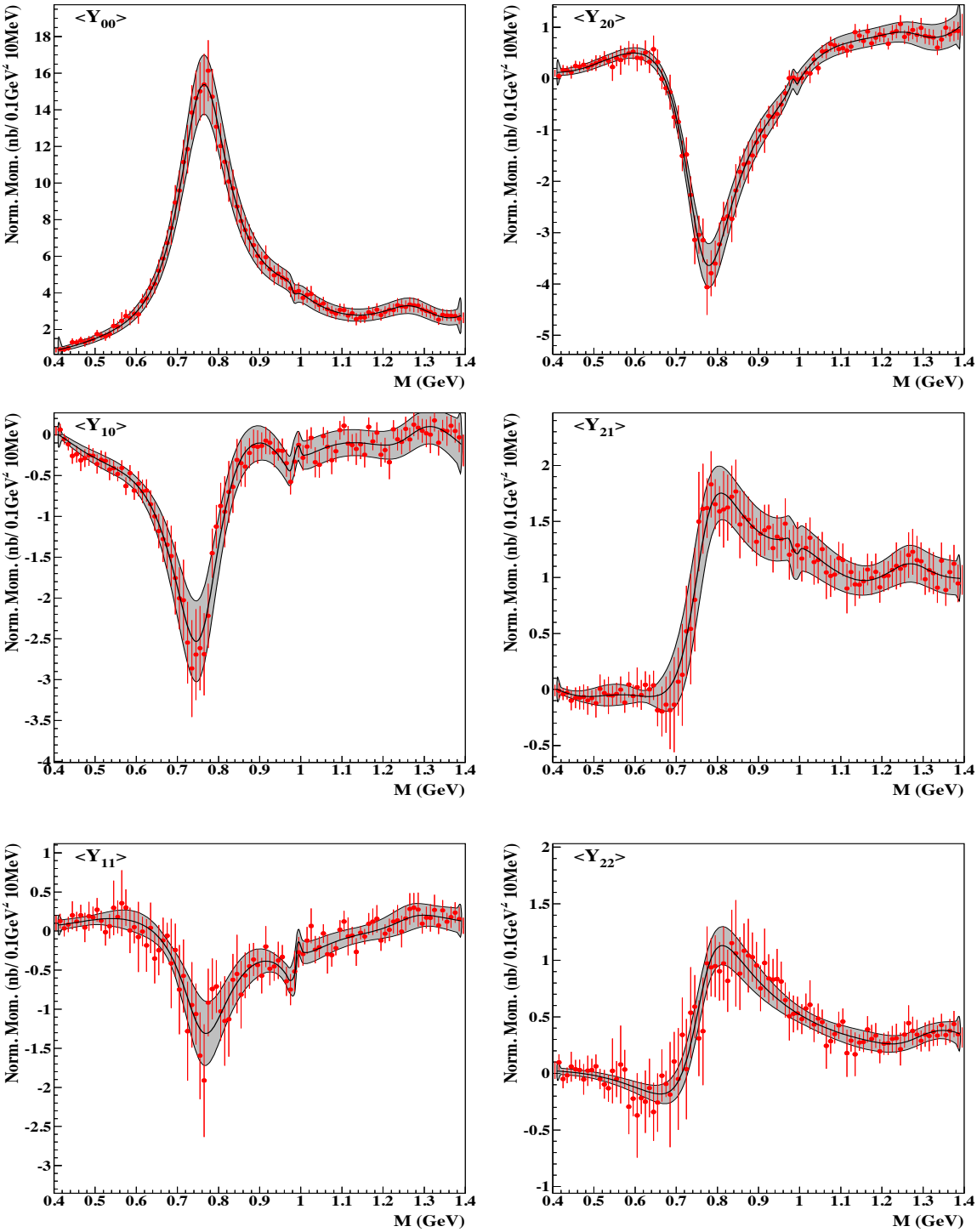

Figure 4.1: Fit result (black line) of the final experimental moments (in red) in $3.4 < E < 3.6$ GeV and $0.5 < -t < 0.6$ GeV^2 bins.

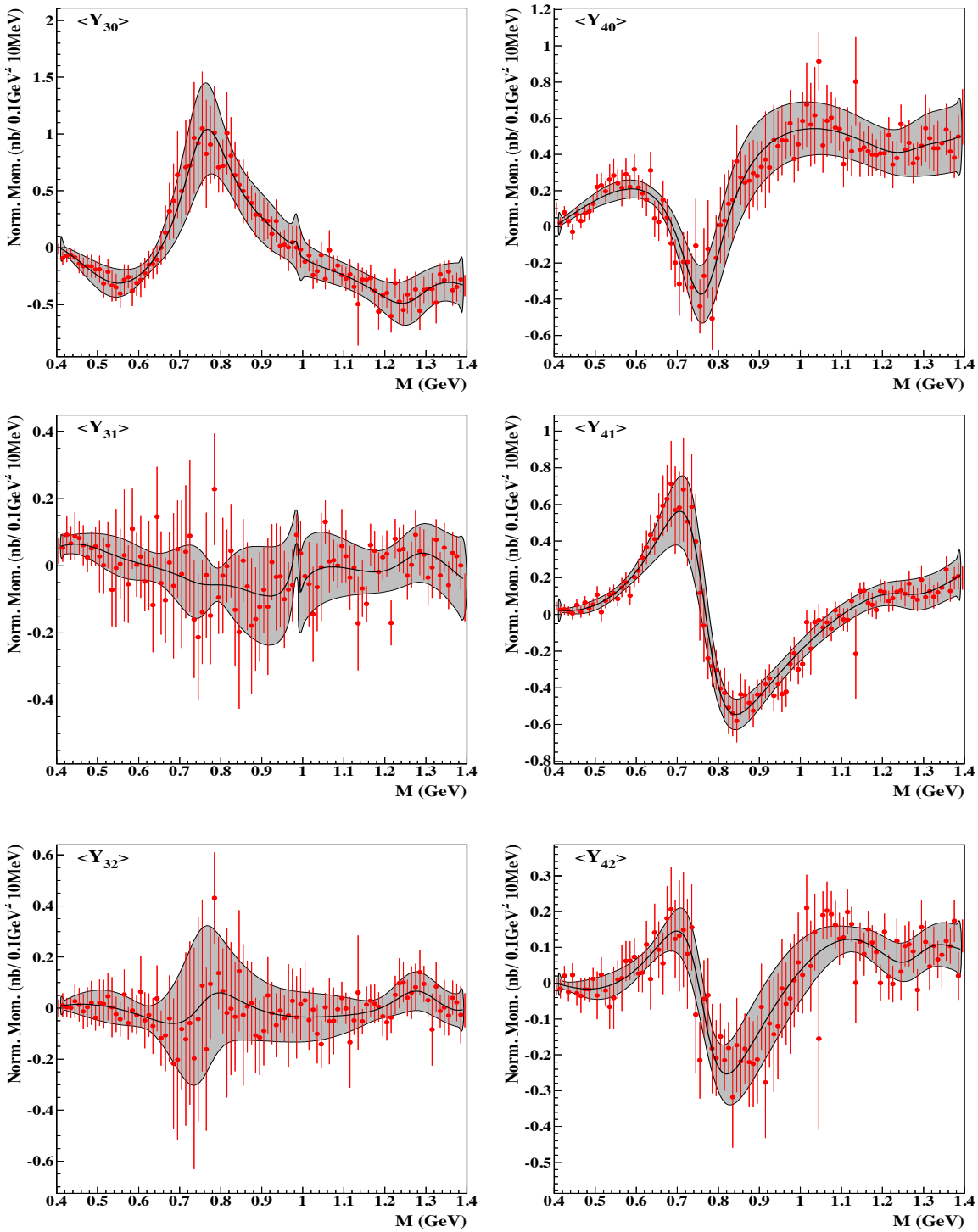

Figure 4.2: Fit result (black line) of the final experimental moments (in red) in $3.4 < E < 3.6$ GeV and $0.5 < -t < 0.6$ GeV^2 bins.

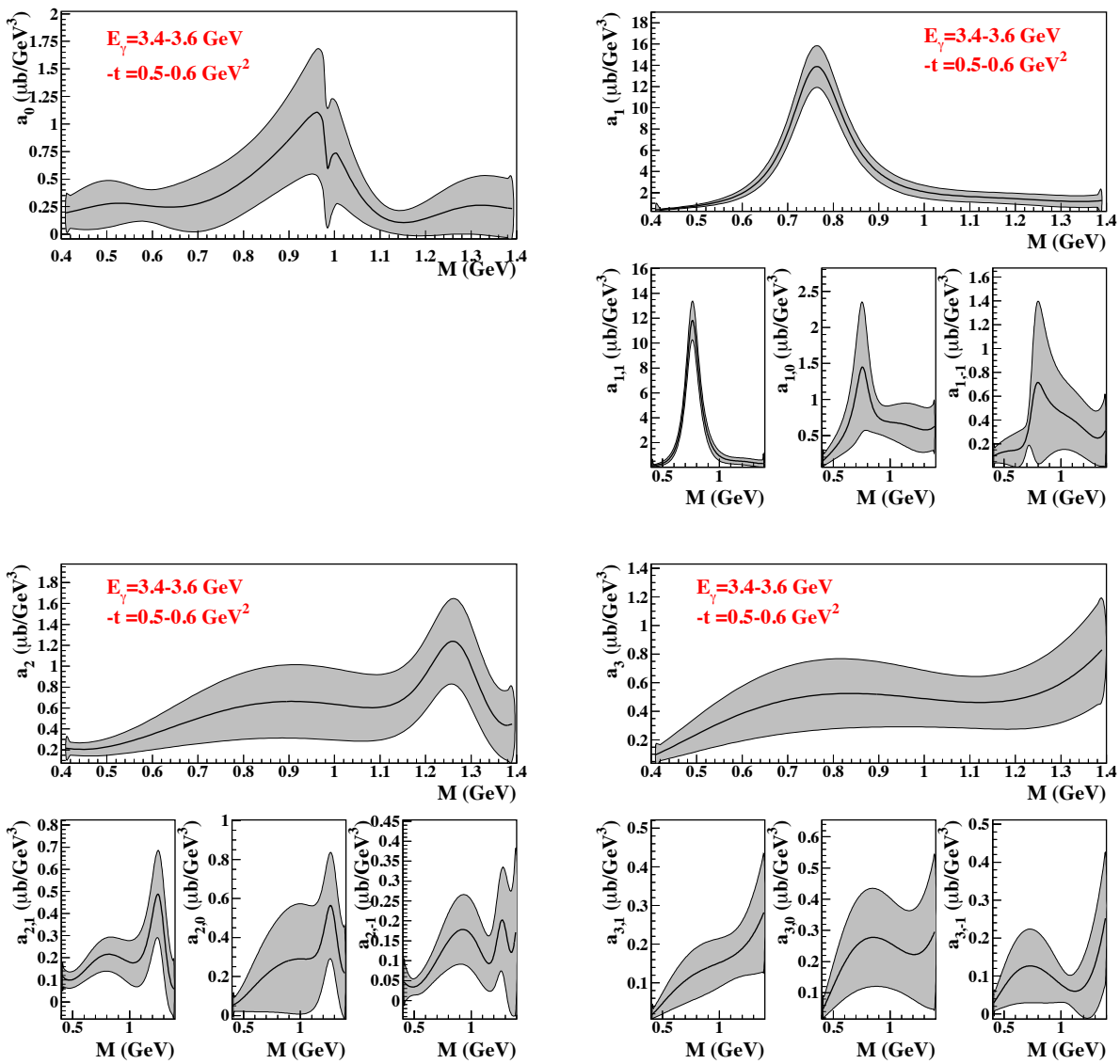

Figure 4.3: Upper plots: magnitude of S, P, D and F partial waves derived by the fit in the $3.4 < E < 3.6$ GeV and $0.5 < -t < 0.6$ GeV^2 bin. Bottom plots: the same amplitudes for the three possible values of $\lambda_{\pi\pi}$ (from left to right +1, 0 and -1).

three helicity amplitudes. The same plots, removing the part of the amplitudes originating from on-shell scattering, as described in Sec. 4.2.1, are shown in Fig. 4.4. As discussed in Appendix A, for the $S - wave$ a detailed study has been done on the effect of truncation to $L_{max} = 4$ to the extracted cross sections (Appendix A.4) and on the separation of the resonant part from the whole wave (Appendix A.5.2). These two sources of systematic uncertainties were estimated to be 25% and 20% respectively. The first was included in the $S - wave$ error bands on squared amplitudes in all energy and $-t$ bins while the latter was added to the error on the resonant part only. It is worth to notice that this systematic error represents a small contribution to the total error, dominated by the systematic error introduced by the difference between the four fit procedures used in the moments extraction.

4.3.3 The spin density-matrix elements

From the production amplitudes derived by the fit we calculated the spin density-matrix elements for the P wave and the interference between P and S waves. Some selected results are shown

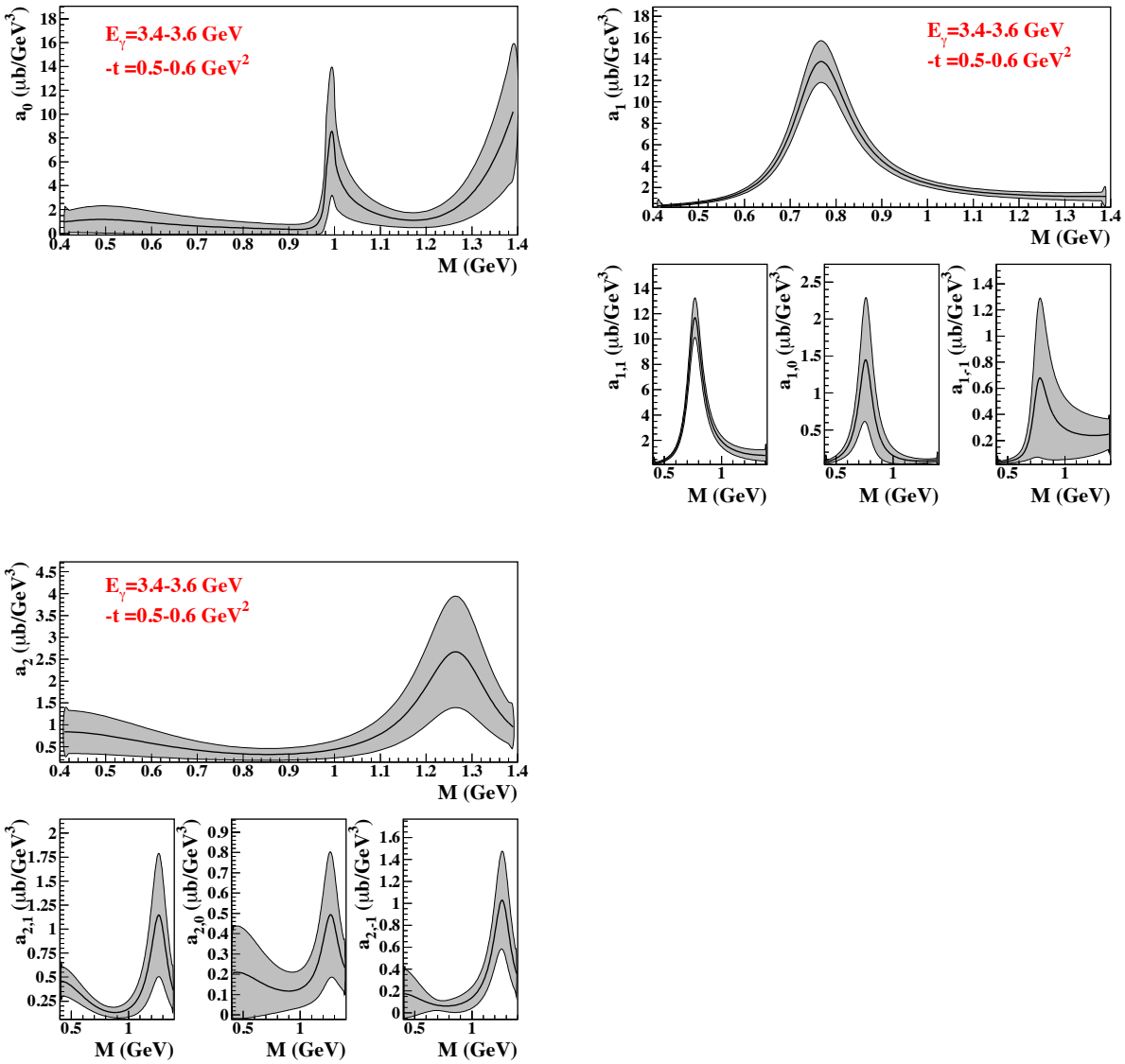

Figure 4.4: The same as in fig. 4.3 without on-shell scattering component.

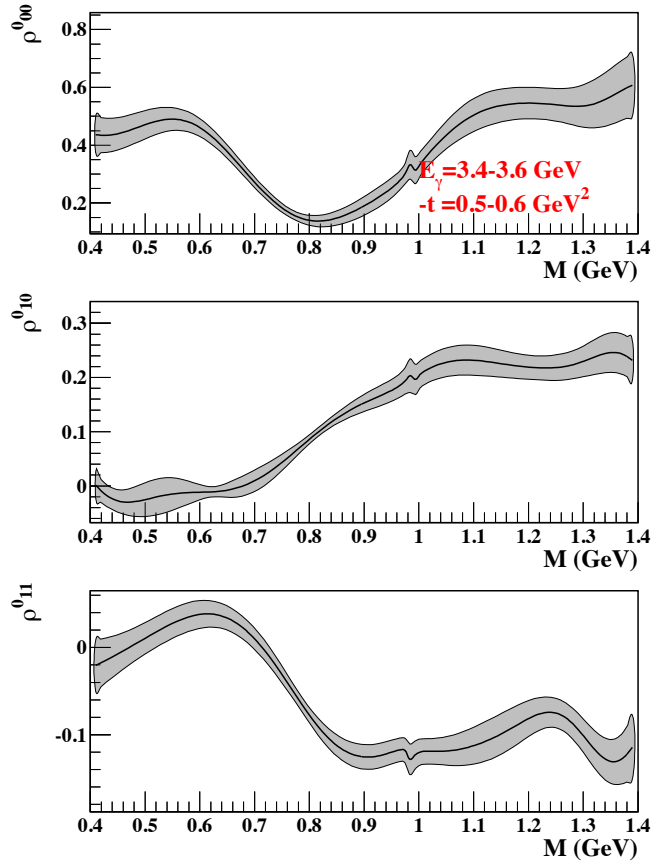

Figure 4.5: Spin density matrix elements for the P wave in the $3.4 < E < 3.6$ GeV and $0.5 < -t < 0.6$ GeV^2 bins.

in figures 4.5 and 4.6. Since these observables do not depend on the photon flux normalization, the error bands do not include the 10% uncertainty mentioned above. Figures 4.7 and 4.8 show the spin density-matrix elements for the P wave measured by Ballam and coauthors in Refs. [16] and [17], in a similar kinematic range ($E_\gamma \sim 2.8, \sim 4.7$ GeV, $0.02 < -t < 0.4$ GeV^2 and $E_\gamma \sim 9.3$ GeV, $0.02 < -t < 0.8$ GeV^2 respectively). Even if different measurement conditions prevent a direct comparison, qualitatively our data show the same behavior with a reduced error. Figure 4.9 shows the superposition of low energy Ballam's data points to our closest kinematic ($3.0 < E < 3.2$ GeV and $0.4 < -t < 0.5$ GeV^2). As expected, the two matrix elements ρ_{10} and ρ_{11} agree very well since they have a weak dependence on $-t$ while ρ_{00} shows a similar behaviour but different values being more sensitive to the momentum transfer. If one compares the larger $-t$ bins we measured, the difference increaseas showing that extrapolating our data to lower $-t$ would probably give a good agreement with previous measurements.
Around $M_{\pi\pi} = 980$ MeV an interference pattern clearly shows up in the S-P wave interference term, corresponding to the contribution from the $f_0(980)$ meson.

4.3.4 Cross-sections

Differential cross-section $d\sigma^l/dt$ for individual waves and mass regions ($Mass \mp \Gamma$) can be obtained integrating the corresponding amplitude. Cross section for $f_0(980)$, ρ and $f_2(1270)$ mesons were obtained integrating the S, P and D waves in the mass range 0.98 ∓ 0.04 GeV, 0.75 ∓ 0.15 GeV, and 1.275 ∓ 0.185 GeV respectively after subtracting the on-shell scattering component. Figures 4.10, 4.11 and 4.12 show the $f_0(980)$, ρ and $f_2(1270)$ cross sections in the 4 energy bins.

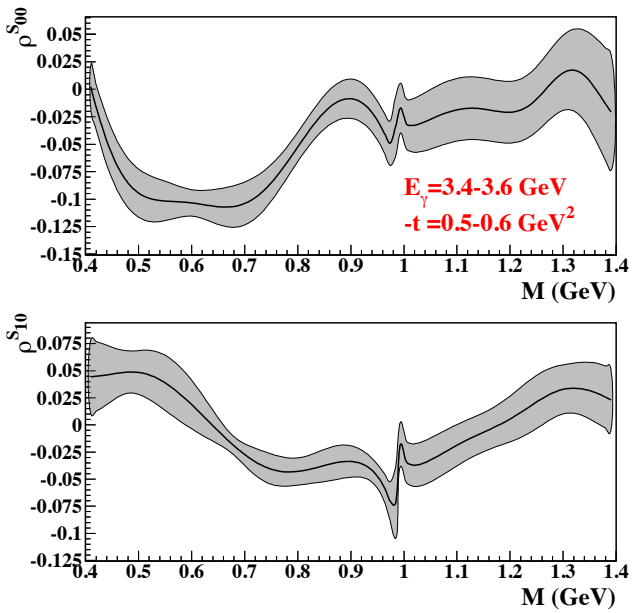

Figure 4.6: Spin density matrix elements for the interference between S and P wave in the $3.4 < E < 3.6$ GeV and $0.5 < -t < 0.6$ GeV^2 bins.

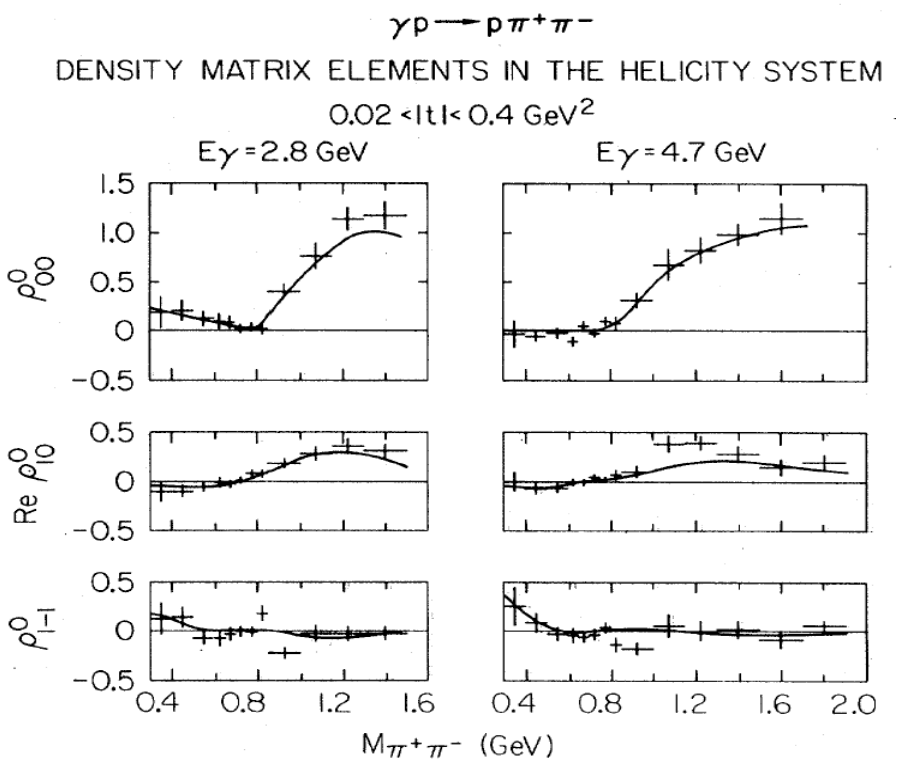

Figure 4.7: Spin density matrix elements for the P wave from Ref. [16].

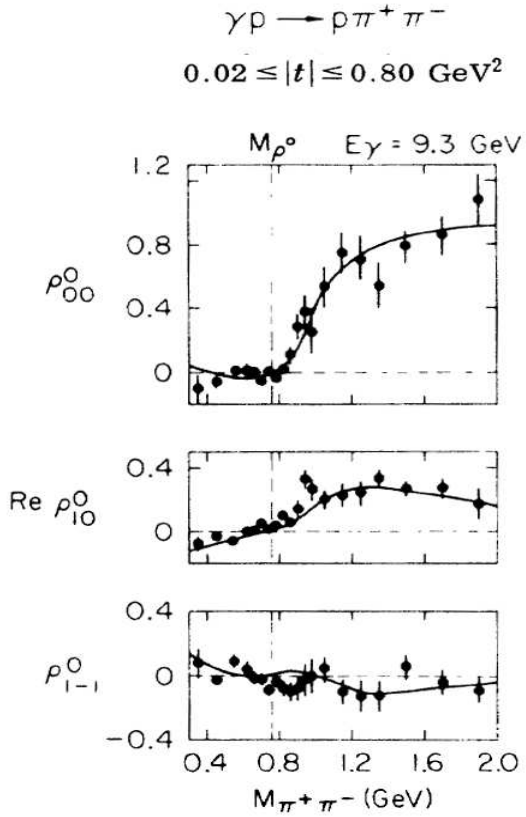

Figure 4.8: Spin density matrix elements for the P wave from Ref. [17].

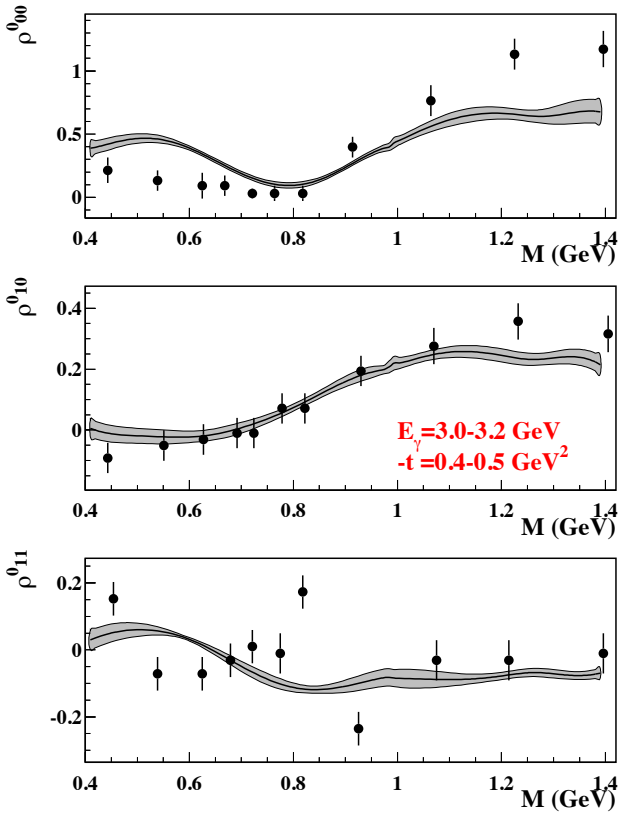

Figure 4.9: Spin density matrix elements for the P wave in the $3.0 < E < 3.2$ GeV and $0.4 < -t < 0.5$ GeV^2 bins. Black dots are data points from Ref. [16], taken in a similar kinematic ($E_\gamma \sim 2.8$, GeV, and $0.02 < -t < 0.4$ GeV^2).

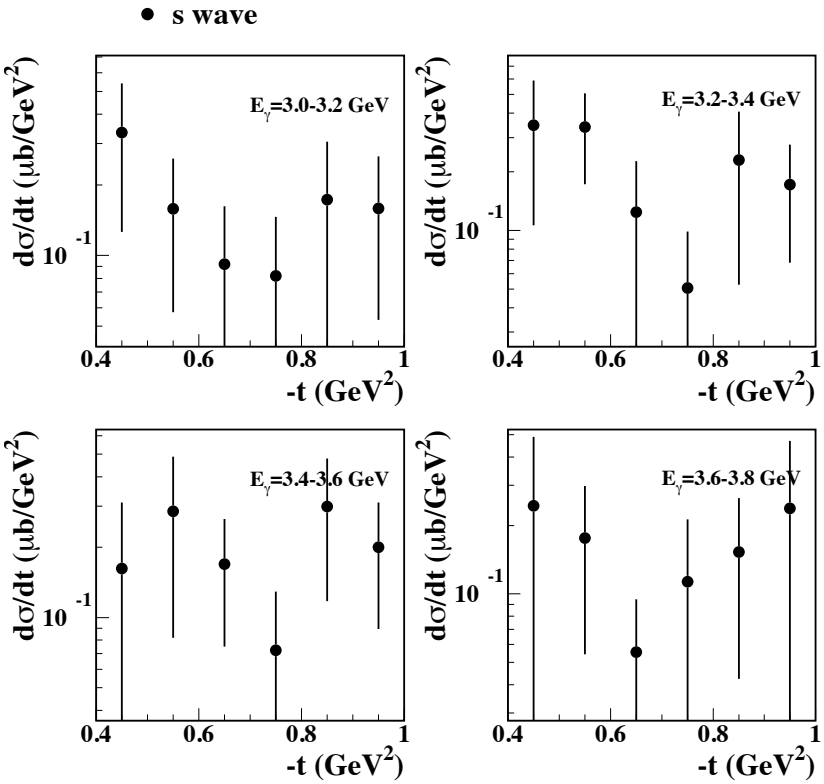

Figure 4.10: Differential cross section $\gamma p \to p f_0(980)$ obtained integrating S wave magnitude in the $M_{\pi\pi}$ range 0.98 ∓ 0.04 GeV without the on-shell scattering component.

As explained before this corresponds to the direct resonance production only disregarding possible contributions from processes where, for example, two pions are photoproduced and rescatter forming an s-channel resonance. Figures 4.13, 4.14 and 4.15, show the cross sections in the $f_0(980)$, ρ and $f_2(1270)$ regions as defined above when the full amplitudes are integrated (direct resonance production + on-shell rescattering processes). These clearly include the background and the interference terms. Errors shown on the plots reflect the systematic error of the fit procedure as described in Par. 4.3.1

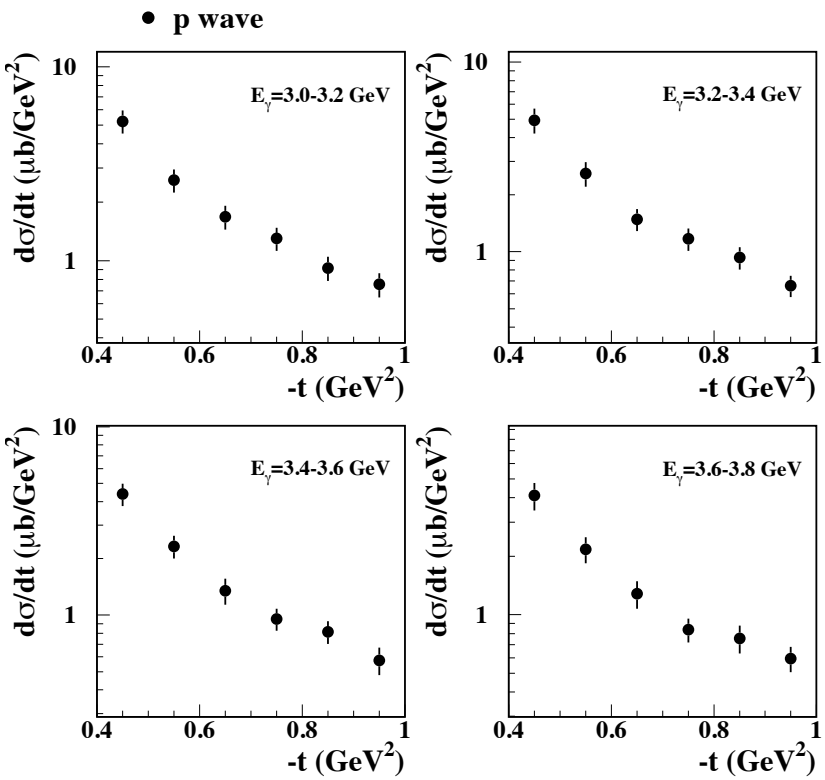

Figure 4.11: Differential cross section $\gamma p \to p\rho$ obtained integrating P wave magnitude in the $M_{\pi\pi}$ range 0.75 ∓ 0.15 GeV without the on-shell scattering component.

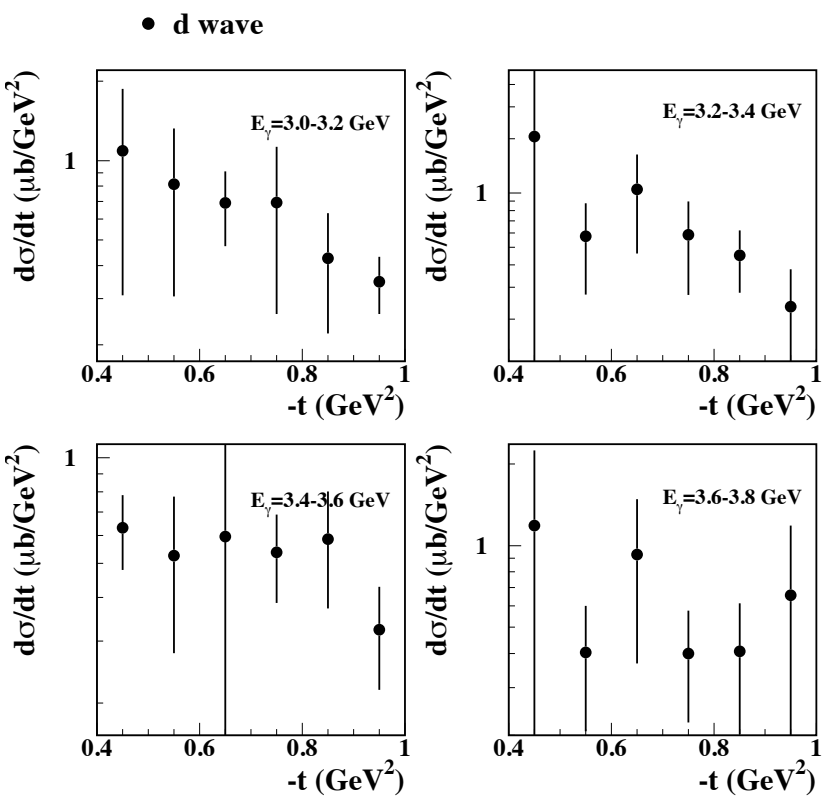

Figure 4.12: Differential cross section $\gamma p \to p f_2(1275)$ obtained integrating P wave magnitude in the $M_{\pi\pi}$ range 1.275 ∓ 0.185 GeV without the on-shell scattering component.

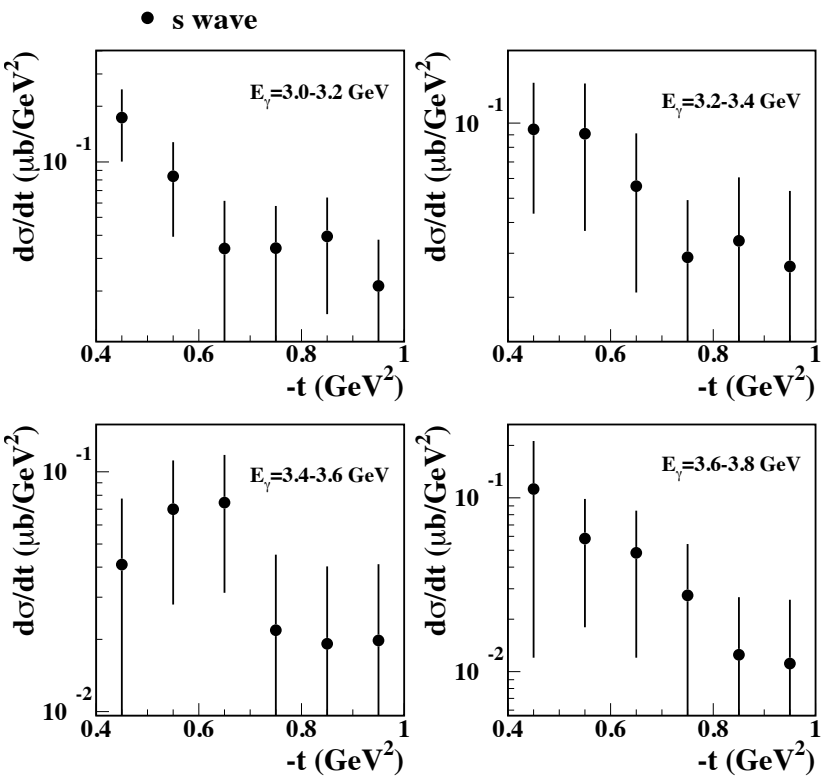

Figure 4.13: Differential cross section associated to the $(L, I) = (0, 0)$ wave integrated in the mass region of the $f_0(980)$ resonance (0.98 ∓ 0.04 GeV).

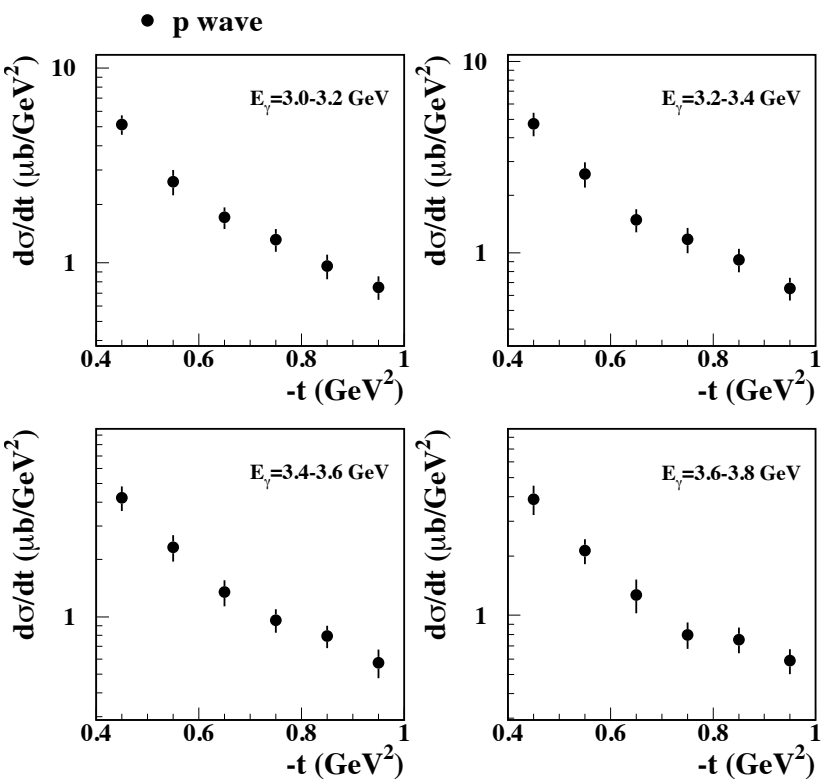

Figure 4.14: Differential cross section associated to the $(L, I) = (1, 1)$ wave integrated in the mass region of the ρ resonance (0.75 ∓ 0.15 GeV).

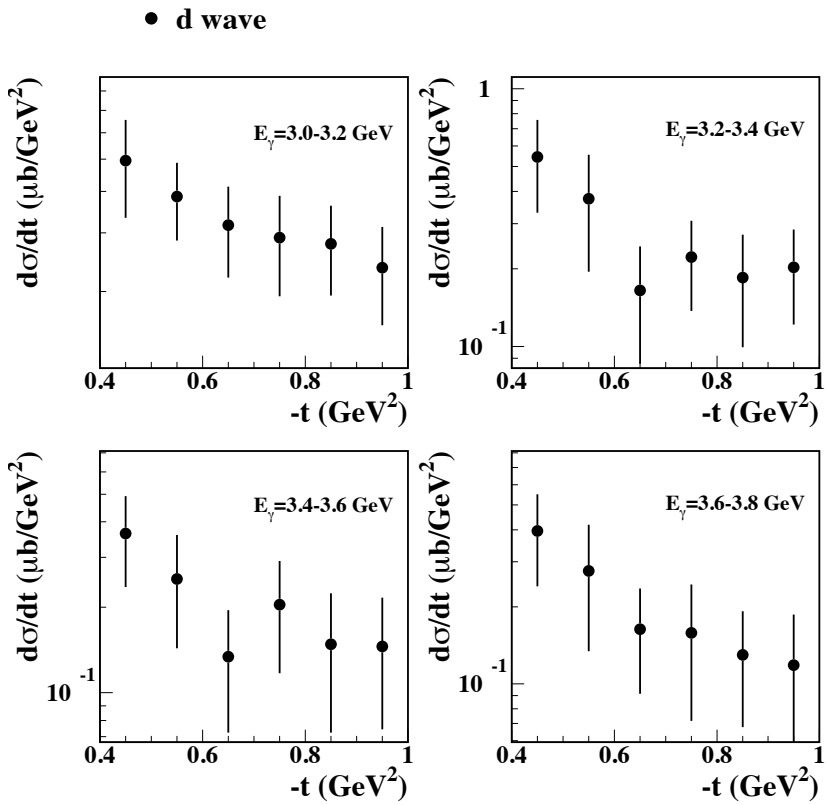

Figure 4.15: Differential cross section associated to the $(L, I) = (2, 0)$ wave integrated in the mass region of the $f_2(1270)$ resonance (1.275 ∓ 0.185 GeV).

Appendix A

Extraction of moments: systematic studies

In this paragraph we show the results obtained varying parameters of the methods used to extract moments of the di-pion angular distribution. All checks and studies reported in the Appendix were made using 50% of the MonteCarlo statistics while final results reported in the main text were made using whole MC events.

A.1 First method: moments of efficiency corrected data

Here we show the results obtained by minimizing the χ^2 defined in eq. 3.15 in one E and t bin, ($3.4 < E < 3.6$, $0.5 < -t < 0.6$). We vary the λ_{max} from 0 up to $\lambda_{max} = 6$. In Figs. A.1 we show the lowest ($\lambda \leq 2$) normalized, acceptance corrected moments $\langle Y_{\lambda\mu} \rangle$ as a function of the di-pion mass for various λ_{max}. We also varied the total number of bins in the helicity angles. Increasing the value of λ_{max} does not improve the fit since higher moments become less constrained. This happens for example for $\lambda_{max} = 6$ when $n_\theta = n_\phi = 10$.

In Fig. A.2, we show the difference between the measured number of events and the number predicted by the fit. The difference is systematically improved as the number of moments in the fit is increased.

Finally in Figs. A.3, A.4 we compare the measured $p\pi$ invariant mass distribution with that predicted by the fit.

A.2 Method 2: parametrization with amplitudes

The results for selected low moments are shown in Fig. A.5, A.6 and A.10. In particular from the difference plots it is clear that this method is superior over the first analysis method described in previous section (moments extracted from efficiency corrected data). For $\lambda_{max} \geq 2$ the low moments are already stable. Clearly, to get the correct $\Delta(1232)$ shape in the $p\pi$ masses, one needs to go to very high $\lambda_{max} \sim 10$ but this is not necessary if we are interested in analyzing the $\pi\pi$ mass to pull out the ρ (P-wave) or $f_0(980)$ (S-wave) signals.

A.3 Method 3: parametrization with moments

The plot of the acceptance corrected moments in shown in Fig. A.8. Looking at the difference plots (fig. A.9), the same conclusion about the goodness of the fit as for the Method 2 are derived. As the number of angular momentum basis states (λ_{max}) is increased the moments with low λ, are unchanged, albeit they become nosier and the fit simply starts populating higher moments.

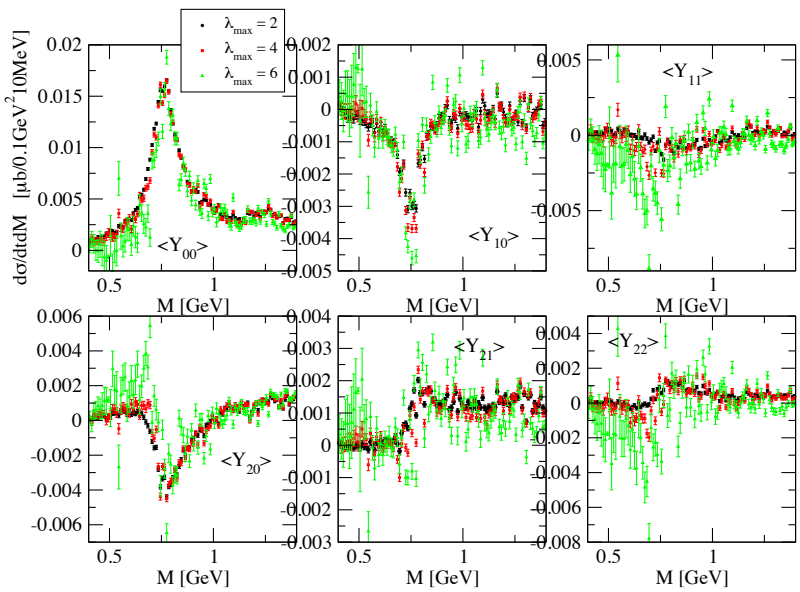

Figure A.1: Acceptance corrected moments $\langle Y_{\lambda\mu} \rangle$ for $3.4 < E < 3.6$, $0.5 < -t < 0.6$ bin as a function of the di-pion mass and varying λ_{max}. The lowest moment $\langle Y_{00} \rangle$ corresponds to the absolute cross section. Angular binning: $n_\theta = 25, n_\phi = 25$. With curse binning in the helicity angles higher moments are not well constrained.

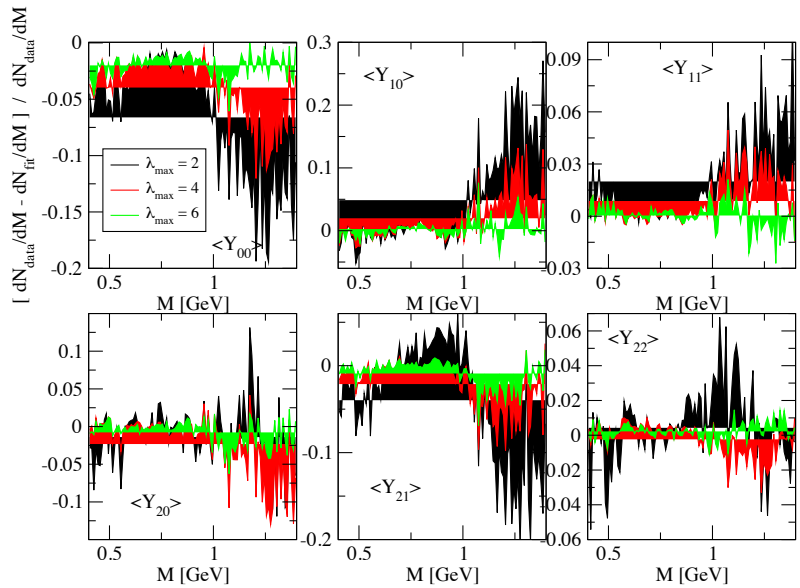

Figure A.2: Difference between measured (acceptance uncorrected) number of events and predicted, acceptance uncorrected number of events computed from the fitted moments weighted with the experimental acceptance, and divided by the measured number of events in each bin. Angular binning: $n_\theta = 25, n_\phi = 25$

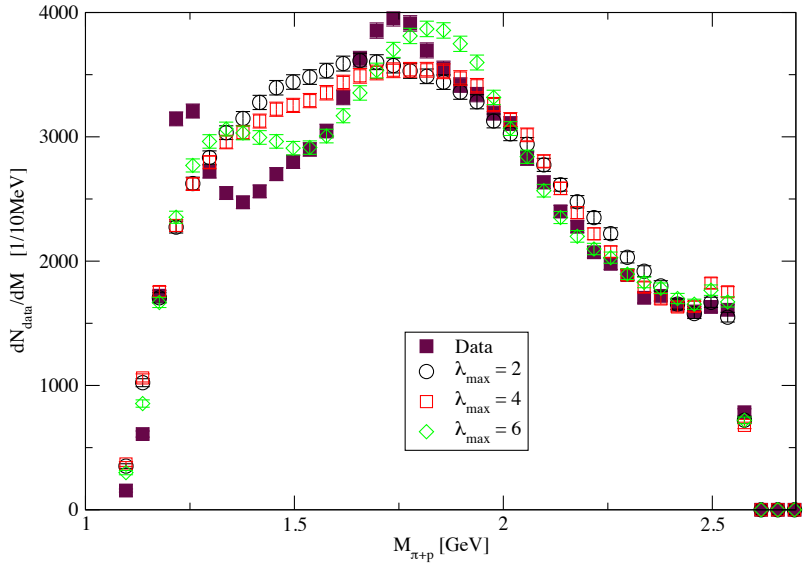

Figure A.3: Measured (acceptance uncorrected) number of events as a function of the $p\pi^+$ invariant mass, compared to the predicted distribution computed used the fitted moments weighted with the experimental acceptance. Angular binning: $n_\theta = 25, n_\phi = 25$.

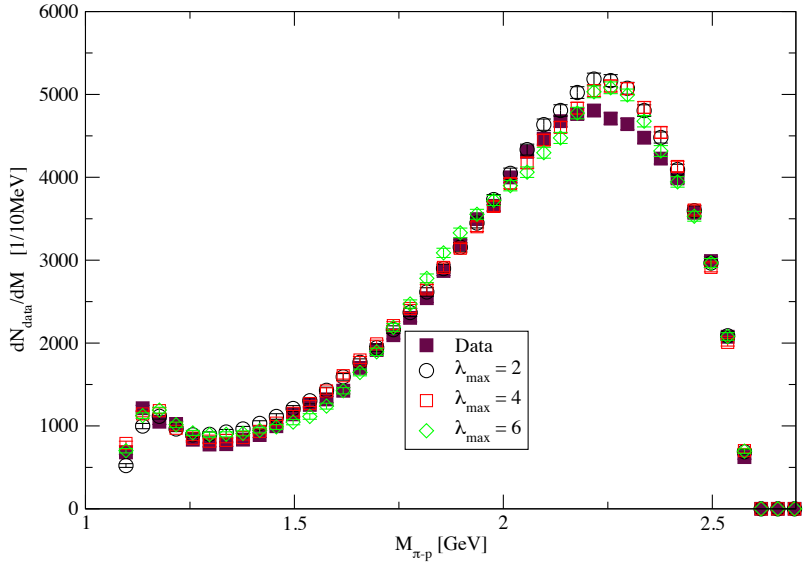

Figure A.4: Measured (acceptance uncorrected) number of events as a function of the $p\pi^-$ invariant mass, compared to the predicted distribution computed used the fitted moments weighted with the experimental acceptance. Angular binning: $n_\theta = 25, n_\phi = 25$.

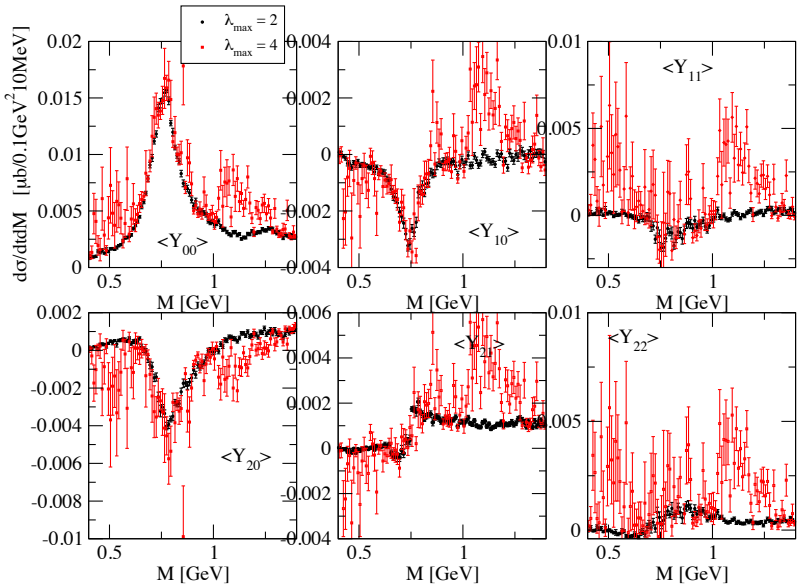

Figure A.5: Acceptance corrected moments $\langle Y_{\lambda\mu} \rangle$ for $3.4 < E < 3.6$, $0.5 < -t < 0.6$ bin computed using log-likelihood fit with the first parametrization as a function of the dipion mass and varying λ_{max}. The lowest moment $\langle Y_{00} \rangle$ corresponds to the absolute number cross section.

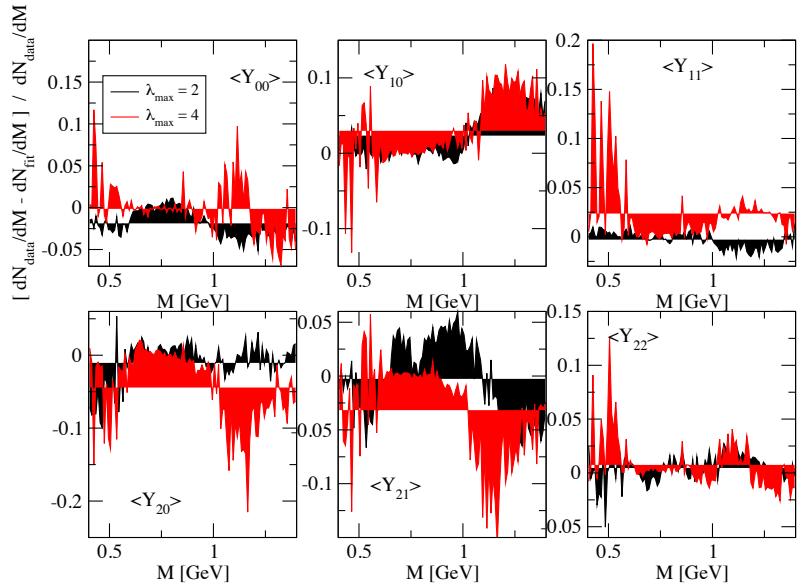

Figure A.6: Difference between measured (acceptance uncorrected) number of events and predicted, acceptance uncorrected number of events computed from the fitted moments weighted with the experimental acceptance, and divided by the measured number of events in each bin. Log likelihood method used.

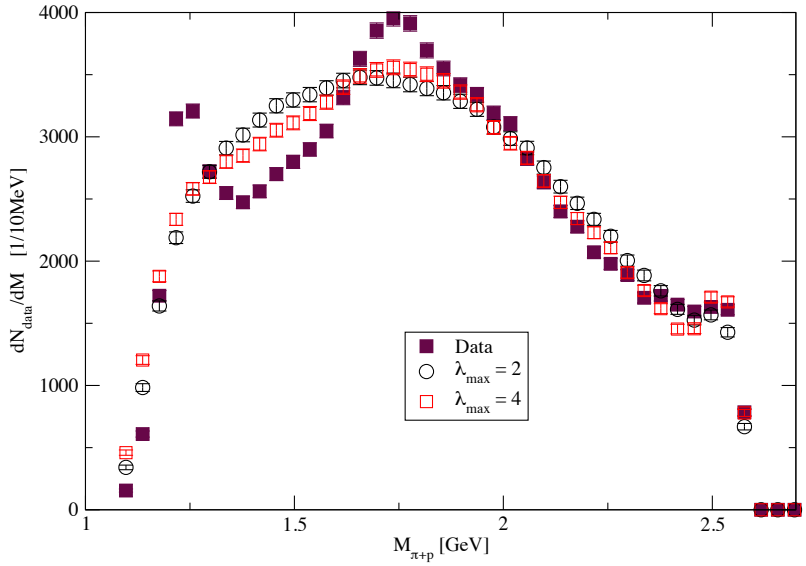

(a)

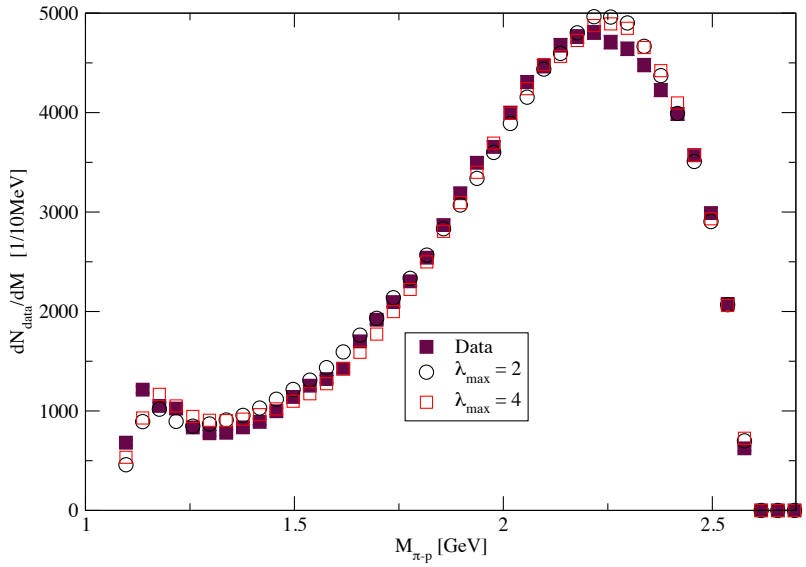

(b)

Figure A.7: Measured (acceptance uncorrected) number of events as a function of the $p\pi^+$ invariant mass, compared to the predicted distribution computed used the fitted moments weighted with the experimental acceptance. Log likelihood method used. a) π^+p b) π^-p

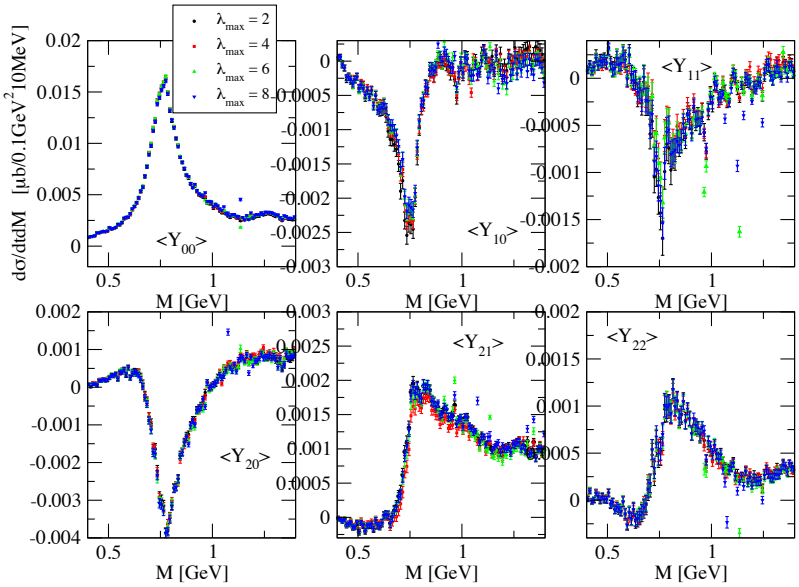

Figure A.8: Acceptance corrected moments $(-1)^{\mu}\langle\tilde{Y}_{\lambda\mu}\rangle$ for $3.4 < E < 3.6$, $0.5 < -t < 0.6$ bin computed using log-likelihood fit with the second parametrization as a function of the peon mass and varying λ_{max}. The lowest moment $\langle Y_{00}\rangle$ corresponds to the absolute cross section.

As already observed, higher moments are mandatory to obtain the correct spectrum of the $p\pi$ systems. To check the sensitivity of the the likelihood fit to the parameter initialization, three different procedures were tested: 1) random initialization, 2) starting with parameters related to $\lambda_{max} = 2$ obtained by the fit using $\lambda_{max} = 2$ (random initialized) and random initialization for λ_{max} from 2 to 4; 3) starting with parameters obtained in 2) and then releasing parameters for moments with $\lambda_{max} = 2$. Results from the three procedures are shown in figures 3.10 and 3.11. Different methods give consistent results. As shown in par. 3.2.5 the difference between the different procedures is used to evaluate the systematic error related to the moment extraction.

A.4 Effect of truncation to $L_{max} = 4$

As discussed in Chap. 3.2.5, we derived the moments of the angular decay distribution using efficiency corrected fitting functions with two different parametrizations and different parameter initialization:

- *Method 1*: fit using parametrization with amplitudes;
- *Method 2a*: fit using parametrization with moments and random initialization of fit parameters;
- *Method 2b*: fit using parametrization with moments and $L < 2$ parameters fixed to the results obtained by using $L_{max} = 2$ fit;
- *Method 2c*: fit using parametrization with moments and $L < 2$ parameters initialized to $L_{max} = 2$ fit.

Independently of the choice of fit parametrization, a truncation in the number of waves (L_{max}) in the fit bases is necessary for practical reasons. All results reported in the note were obtained

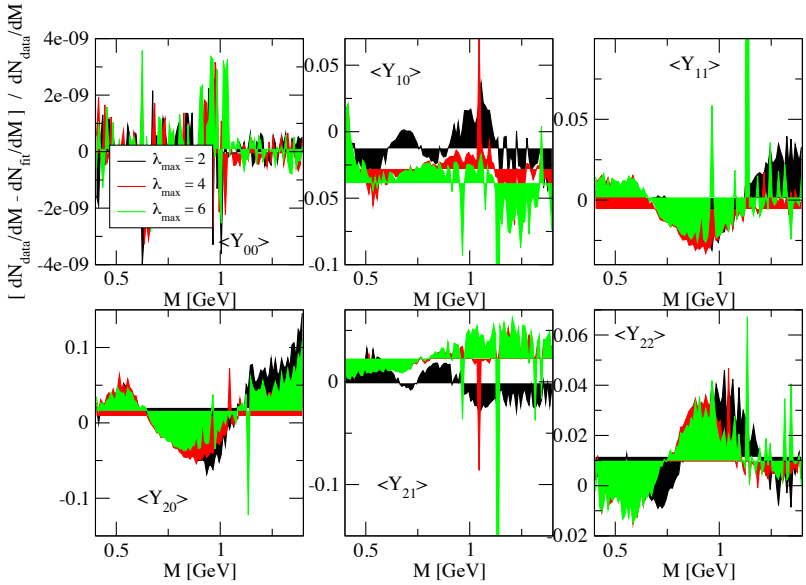

Figure A.9: Difference between measured (acceptance uncorrected) number of events and predicted, acceptance uncorrected number of events computed from the fitted moments weighted with the experimental acceptance, and divided by the measured number of events in each bin. Log likelihood method used.

with $L_{max} = 4$. The rational of this choice is twofold: first the analysis focused on the extraction of low moments that are less affected by this truncation; second, including higher waves leads to larger fluctuation in the extracted moments without significant effect on the extracted moments for $M_{\pi\pi} < 1.1$ GeV. Some systematic studies were performed to evaluate the goodness of this choice and evaluate the error related to the truncation.

A.4.1 Effect on observables

The $L_{max} = 4$ fit reproduces the main features of the data in many observables (when $M_{\pi\pi} < 1.1$ GeV). We compared the measured quantities to the results obtained by the fit:
- helicity angles: see Fig. A.11 where decay angles are plot;
- invariant masses: see Fig. A.12 reporting $M_{p\pi}$ for three different $M_{\pi\pi}$ intervals $M_{\pi\pi} = 0.475 \pm 0.01$, $M_{\pi\pi} = 0.775 \pm 0.01$,$M_{\pi\pi} = 1.295 \pm 0.01$. As shown by the plots above, the data features are well reproduced by the fit results using $L_{max} = 4$. It should be noticed that the discrepancy between the data and $L_{max} = 4$ fit results in the $M_{p\pi}$ spectrum shown for example in fig. A.10 is due to events with $M_{\pi\pi} > 1.3$ GeV, i.e. a range that is not in the main focus of this analysis.

A.4.2 Evaluation of the truncation error on the $S - wave$ using simulations

To have a quantitative estimate of the truncation error we performed a detailed analysis using MC events. We fitted the data with $L_{max} = 8$ using *Method 2a*, we generated events using the fit results and then we extracted moments from the pseudo-data using both $L_{max} = 4$ and $L_{max} = 8$. The latters were analyzed using the same procedure developed for real data up to the extraction of the $f_0(980)$ cross section. At each step we compared the *Generated* and *Reconstructed* ($L_{max} = 4, 8$) observables. All checks were performed on the 'test' bin:

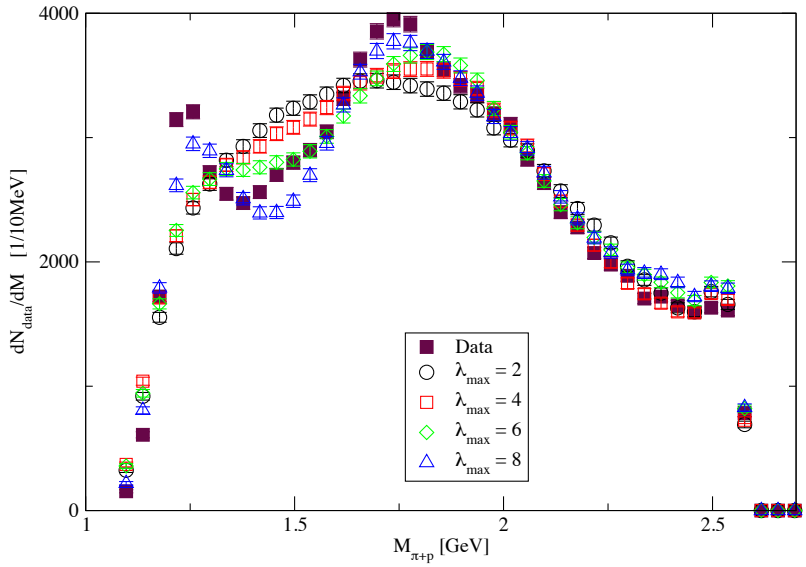

(a)

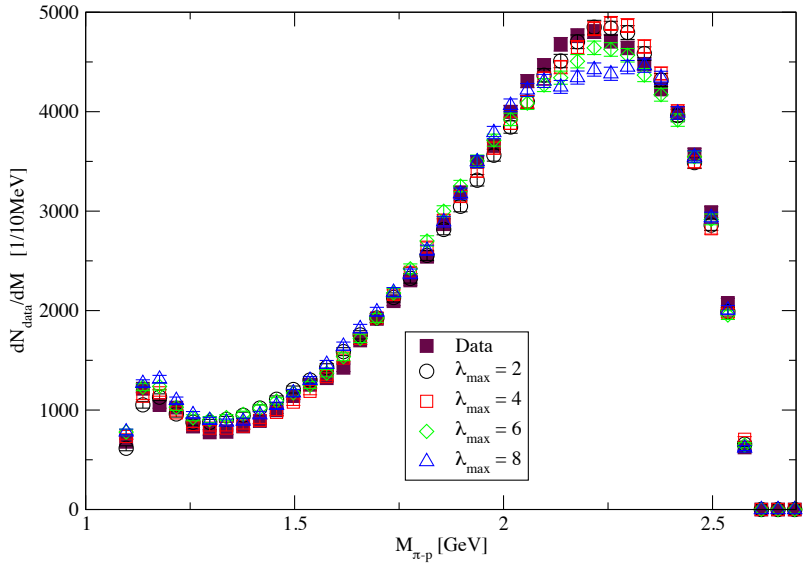

(b)

Figure A.10: Measured (acceptance uncorrected) number of events as a function of the $p\pi^+$ invariant mass, compared to the predicted distribution computed used the fitted moments weighted with the experimental acceptance. Log likelihood with the second parametrization method used. a) π^+p b) π^-p

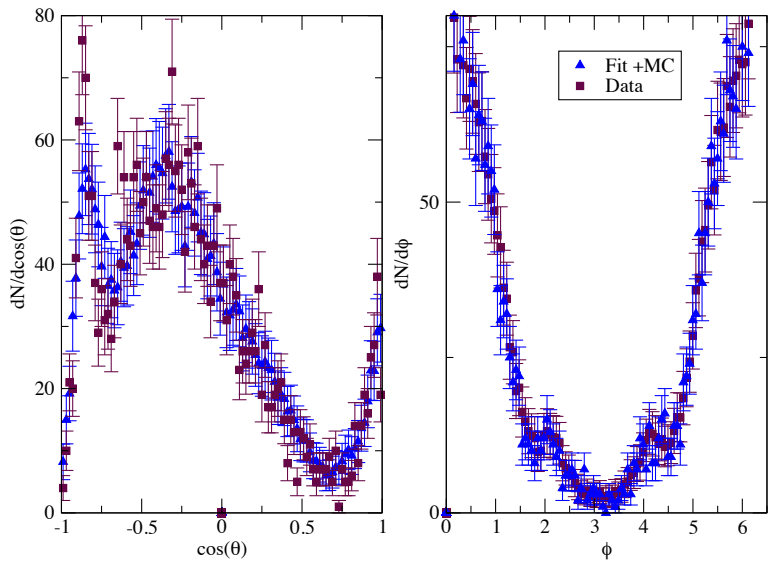

Figure A.11: Comparison of helicity angles in the $f_0(980)$ mass region ($M_{\pi\pi} = 0.985 \pm 0.01$ GeV) as measured (red) and reconstructed by the fit procedure using $L_{max} = 4$ (blue).

$3.4 < E < 3.6$ GeV and $0.5 < -t < 0.6$ GeV^2. Figure A.13 shows generated and reconstructed moments while fig. A.14 shows the resulting (full and resonant) partial waves.

Integrating the bottom left plot in fig. A.14 in the range $M_{p\pi} = 0.98 \pm 0.04$ GeV, we extracted the $f_0(980)$ cross section from generated and reconstructed moments. We used the difference as an estimate of the systematic error associated with the truncation. We found:
- $\sigma = 0.15 \pm 0.02$ μb from generated;
- $\sigma = 0.19 \pm 0.03$ μb from reconstructed using $L_{max} = 4$;
- $\sigma = 0.23 \pm 0.06$ μb from reconstructed using $L_{max} = 8$.

A.4.3 Evaluation of the truncation error on the $S - wave$ using data

With $L_{max} = 4$, all methods converge and we derived four sets of results that were fit to the dispersion relations to extract the partial waves (as presented in Chap. 4). The comparison of the results obtained with these different methods allowed us to estimate the systematic error associated to the analysis procedure. Going to $L_{max} = 8$, *Method 1* does not converge properly due to the noise introduced by higher waves. This can be clearly seen in Fig. A.15 where moments extracted with the two different L_{max} are shown.

These issues with the converge of $L_{max} = 8$ fits are the reason why we have chosen to work with $L_{max} = 4$. In fact fits with $L_{max} = 4$ are stable and converging for all the four methods listed above allowing us to estimate the systematic error associated with the specific analysis procedure.

With , $L_{max} = 8$ *Method 2* shows larger errors and some scattered bins, see Fig. A.16, but still a reasonable convergence allowing a direct comparison to results obtained with $L_{max} = 4$.

To estimate the effect of the L_{max} truncation in the final cross section, for a specific energy and $-t$ bin, we fitted moments extracted with $L_{max} = 8$ (see Fig. A.17) derived the partial waves, total and direct production, (see Fig. A.18) and compare to the results obtained by using $L_{max} = 4$.

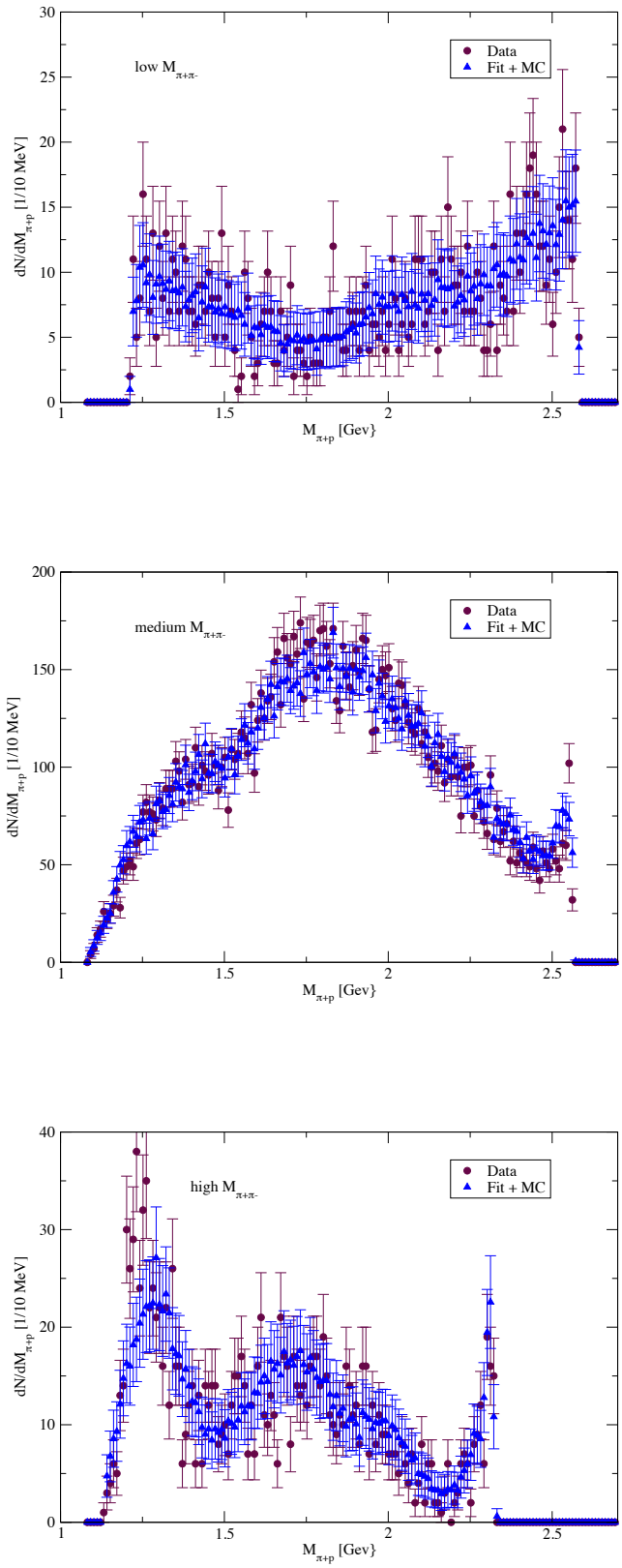

Figure A.12: Comparison of $M_{p\pi}$ in three different $M_{\pi\pi}$ mass regions ($M_{\pi\pi} = 0.475 \pm 0.01$, $M_{\pi\pi} = 0.775 \pm 0.01$,$M_{\pi\pi} = 1.295 \pm 0.01$) as measured (red) and reconstructed by the fit procedure using $L_{max} = 4$ (blue).

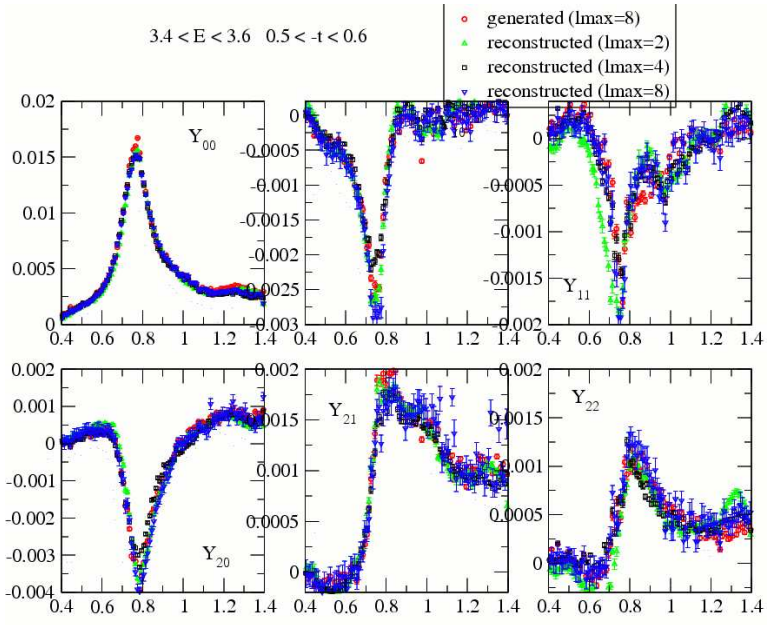

Figure A.13: Moments from generated and reconstructed pseudo-data for $3.4 < E < 3.6$, $0.5 < -t < 0.6$ bin. Red: generated; green:reconstructed with $L_{max} = 2$; black: reconstructed with $L_{max} = 4$; blue: reconstructed with $L_{max} = 8$.

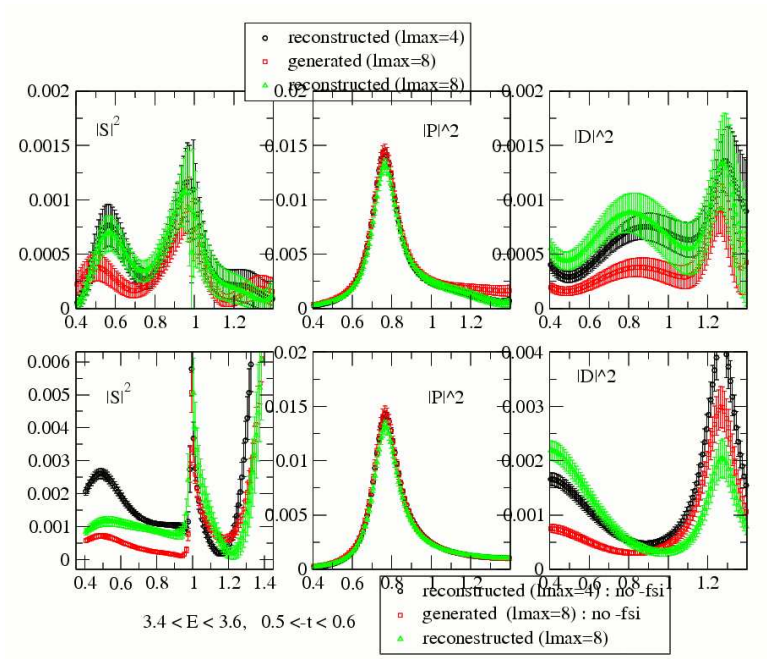

Figure A.14: Partial waves from generated and reconstructed pseudo-data for $3.4 < E < 3.6$, $0.5 < -t < 0.6$ bin. Red: as obtained by the generated events; black: as obtained by reconstructed events ($L_{max} = 4$) green: as obtained by reconstructed events ($L_{max} = 8$). Upper plot: total waves; bottom: resonant part.

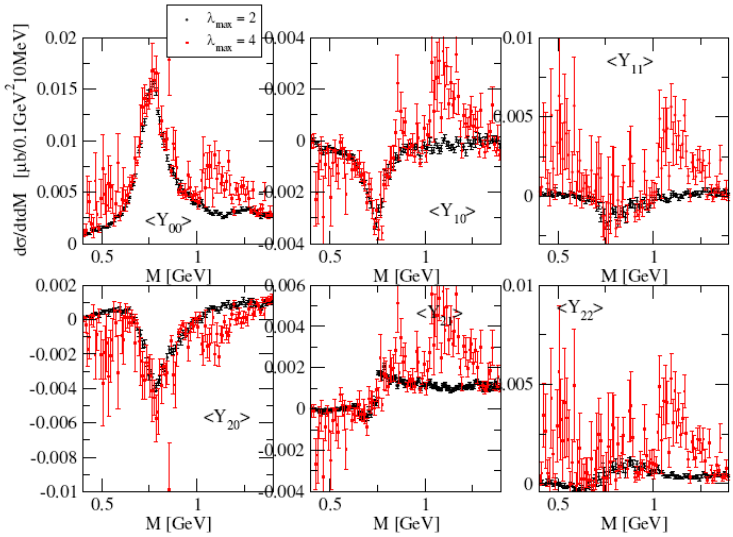

Figure A.15: Acceptance corrected moments $(-1)^{\mu}\langle\tilde{Y}_{\lambda\mu}\rangle$ for $3.4 < E < 3.6$, $0.5 < -t < 0.6$ bin extracted with *Method 1* with different L_{max}. The lowest moment $\langle Y_{00}\rangle$ corresponds to the absolute cross section. Since these are the maximum L entering in the amplitudes, they correspond to $L_{max} = 4$ and 8 in *Method 2*.

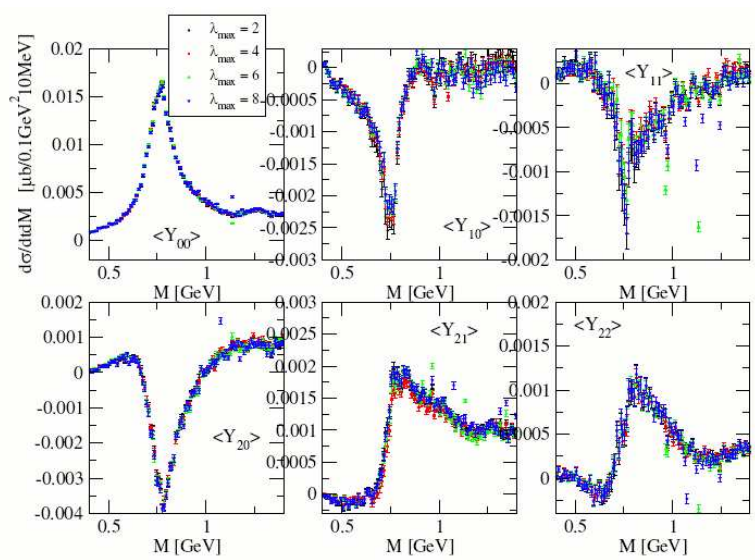

Figure A.16: Acceptance corrected moments $(-1)^{\mu}\langle\tilde{Y}_{\lambda\mu}\rangle$ for $3.4 < E < 3.6$, $0.5 < -t < 0.6$ bin extracted with *Method 2* with different L_{max}. The lowest moment $\langle Y_{00}\rangle$ corresponds to the absolute cross section.

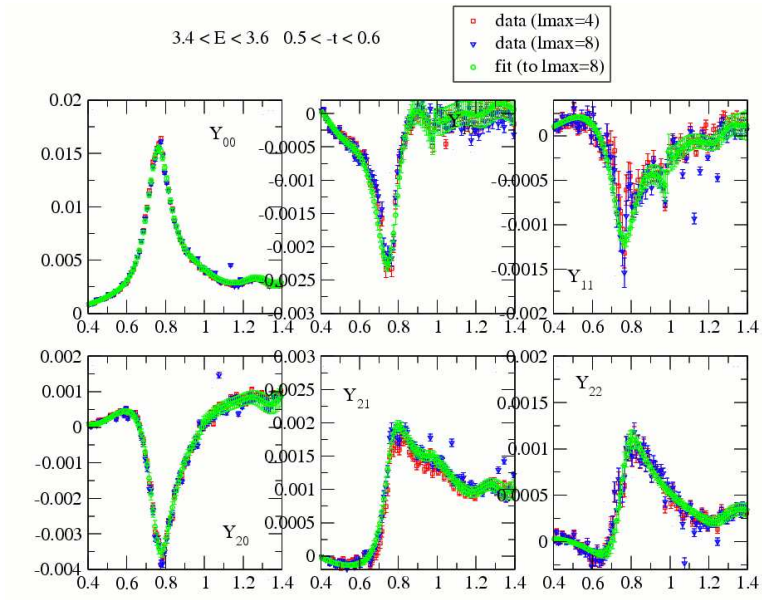

Figure A.17: Comparison of acceptance corrected moments $(-1)^{\mu}\langle\tilde{Y}_{\lambda\mu}\rangle$ for $3.4 < E < 3.6$, $0.5 < -t < 0.6$ bin extracted with *Method 2* with $L_{max} = 4, 8$ and results of the fit for $L_{max} = 8$ moments.

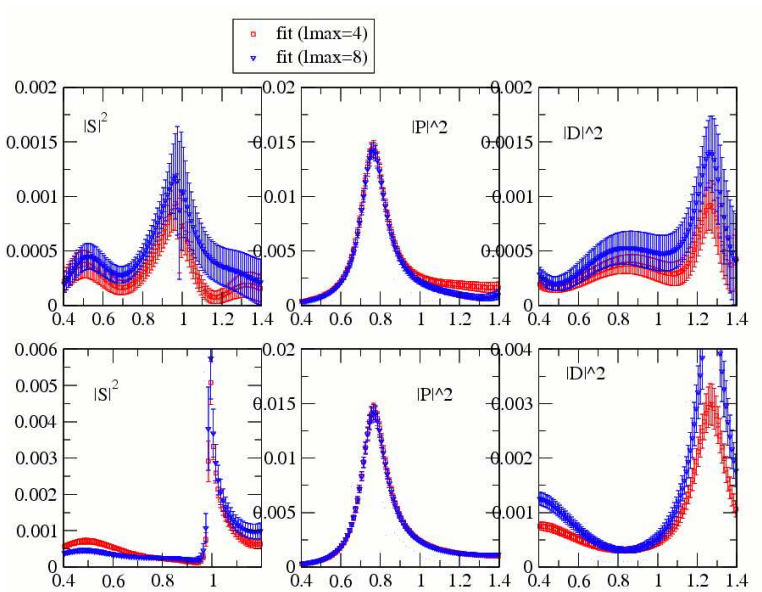

Figure A.18: Comparison of partial waves for $3.4 < E < 3.6$, $0.5 < -t < 0.6$ bin extracted with $L_{max} = 4, 8$. Upper panel: total partial wave; bottom panel: direct production

Integrating the S-wave (resonant part only) in the $f_0(980)$ region, we found:
- $\sigma = 0.18 \pm 0.04$ μb using $L_{max} = 8$;
- $\sigma = 0.15 \pm 0.03$ μb using $L_{max} = 4$;

As expected, the two values are compatible at 1σ and the result obtained with $L_{max} = 8$ has a bigger error. From here we conclude that the observables of interst can be reliably extracted with $L_{max} = 4$ and that there is no evidence of significant effect (within quoted error bars) due to the truncation.

A.4.4 Conclusions

In summary, results obtained using $L_{max} = 8$, when available, are consistent with the results obtained with $L_{max} = 4$ but in general appear to be less stable and reliable due to the fit non converging or to noise introduced by the higher waves. The conservative estimate of the systematic error associated to the truncation at $L_{max} = 4$ was then computed comparing the results obtained by the Monte Carlo simulations (Par. A.4.2). Generated and reconstructed events were compared obtaining:

$$\frac{|(Gen - Rec_{L_{max}=4})|}{2|(Gen + Rec_{L_{max}=4})|} \sim 25\% \tag{A.1}$$

This error was summed in quadrature to all the extracted cross sections to take into account the effect of the truncation in L_{max}.

A.4.5 Other systematic checks

Monte Carlo simulations were also used to perform some more systematic studies in particular we checked the moment extraction procedure and the acceptance of CLAS as a possible source of the signal associated to the $f_0(980)$.

Moment extraction using MC

The same event generator described in Chap. 2.1, used to extract the ρ photoproduction cross section was also used to check the moment extraction. This MC is based on a total different technique, not using a partial wave expansion to generate events but simply summing incoherently many different channels with the same final state. In particular angular distributions of various processes are based on interpolation of available data, without an explicit limitation on the numeber of waves included. Therefore, using this MC we expect to have a real independent check on our capability of extracting moments and see the effect of L_{max} truncation. Figure A.19 shows the comparison between moments calculated directly form the generated events (in black) and moments obtained by using *Method 2b* $L_{max} = 2$ (in red) and $L_{max} = 4$ (in green). The fit reproduces the data up to $M_{\pi\pi}$ ~1.1 GeV and and in particular Y_{10} shows a clear improvement going from $L_{max} = 2$ to $L_{max} = 4$. This is another confirmation that, even in this case, where the comparison to the real data is only qualitative, moments can be reproduced by using a limited number of terms. Noise in moments extracted with $L_{max} = 4$ is mainly due to the poor statistics used for this test. This MC does not include the $f_0(980)$ production channel.

Effect of CLAS acceptance on $M_{\pi\pi}$ mass

One possible issue is related to the distortion introduced by the CLAS acceptance to the $M_{\pi\pi}$ that could mimic a resonance peak. We addressed this problem using Monte Carlo simulations based on the partial wave analysis derived by our own analysis described in Par. A.4.2 of this Appendix with $L_{max} = 4$. Events were generated after removing by hand the $f_0(980)$ signal, and then processing the pseudo-data with the usual analysis chain (*Method 2b* with $L_{max} = 2, 4$).

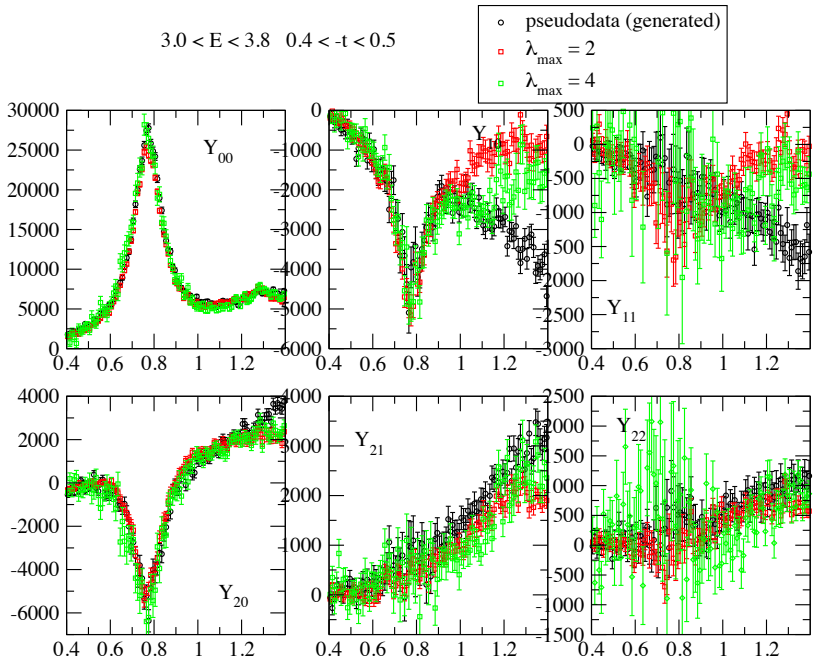

Figure A.19: Moments $(-1)^{\mu}\langle\tilde{Y}_{\lambda\mu}\rangle$ for $3.4 < E < 3.6$, $0.5 < -t < 0.6$ bin computed from pseudo-data obtained by the Monte Carlo program described in Chap. 2.1: moments were computed from generated events (black) and reconstructed events using $L_{max} = 2$ (red) and $L_{max} = 4$ (green).

Results are shown in fig. A.20: when events are generated without the $f_0(980)$, no sharp structure appears due to the CLAS acceptance effect. From here we conclude that, the peak around the $f_0(980)$ mass is not created by the CLAS acceptance.

Effect of $M_{\pi\pi}$ mass binning in the moment extraction

To check the effect of $M_{\pi\pi}$ mass binning we calculated moments using a finer binning (5 MeV in place of standard 10 MeV) and shifting the binning by half the original bin size. As shown in fig A.21, the behavior of moments is unchanged as well as the structures present around M=980 MeV.

A.5 Systematic studies on the truncation of PWA expansion and waves parametrization

A.5.1 Truncation of partial wave expansion of moments

If data gave direct access to $\pi\pi$ amplitudes these would be the only undetermined parameters in the theoretical parametrization. In reality, however, it is the moments and not individual partial waves that can be unambiguously extracted from the data (assuming acceptance corrections are under control). A given $\pi\pi$ moment involves an infinite number of $\pi\pi$ partial waves. For example

$$\langle Y_{00}\rangle = |S|^2 + \sum_{m=0\pm1} |P_m|^2 + \sum_{m=0,\pm1,2} |D_m|^2 + \cdots$$

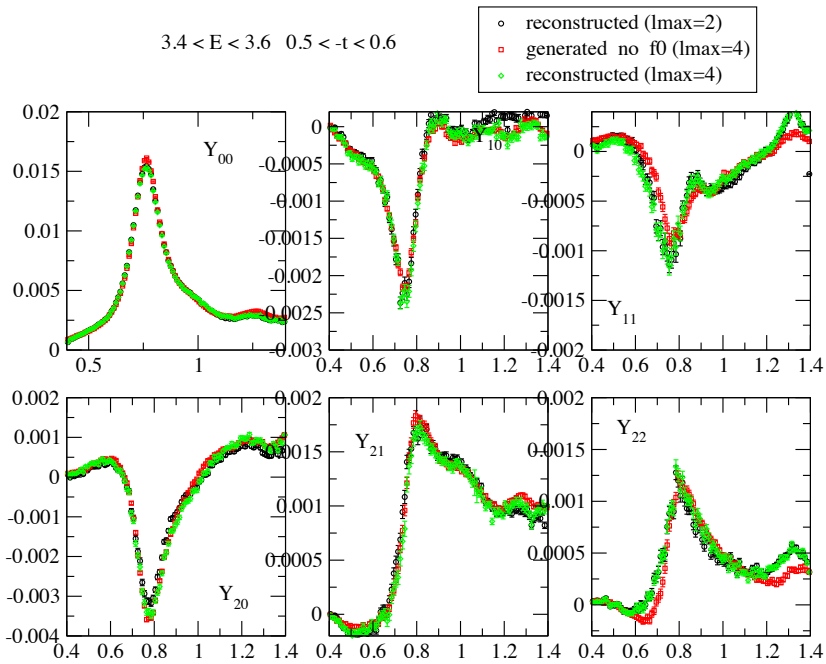

Figure A.20: Moments extracted from generated pseudo-data with no $f_0(980)$ (in red) compared to moments obtained by reconstructed events using *Method 2b* with $L_{max} = 2$ (red) and $L_{max} = 4$ (green). (moments from reconstructed MC events using L max =4 and 2) Moments $(-1)^{\mu}\langle\tilde{Y}_{\lambda\mu}\rangle$ for $3.4 < E < 3.6$, $0.5 < -t < 0.6$ bin computed from pseudo-data obtained by the Monte Carlo program described in Chap. 2.1: moments were computed from generated events (black) and reconstructed events using $L_{max} = 2$ (black) and $L_{max} = 4$ (green).

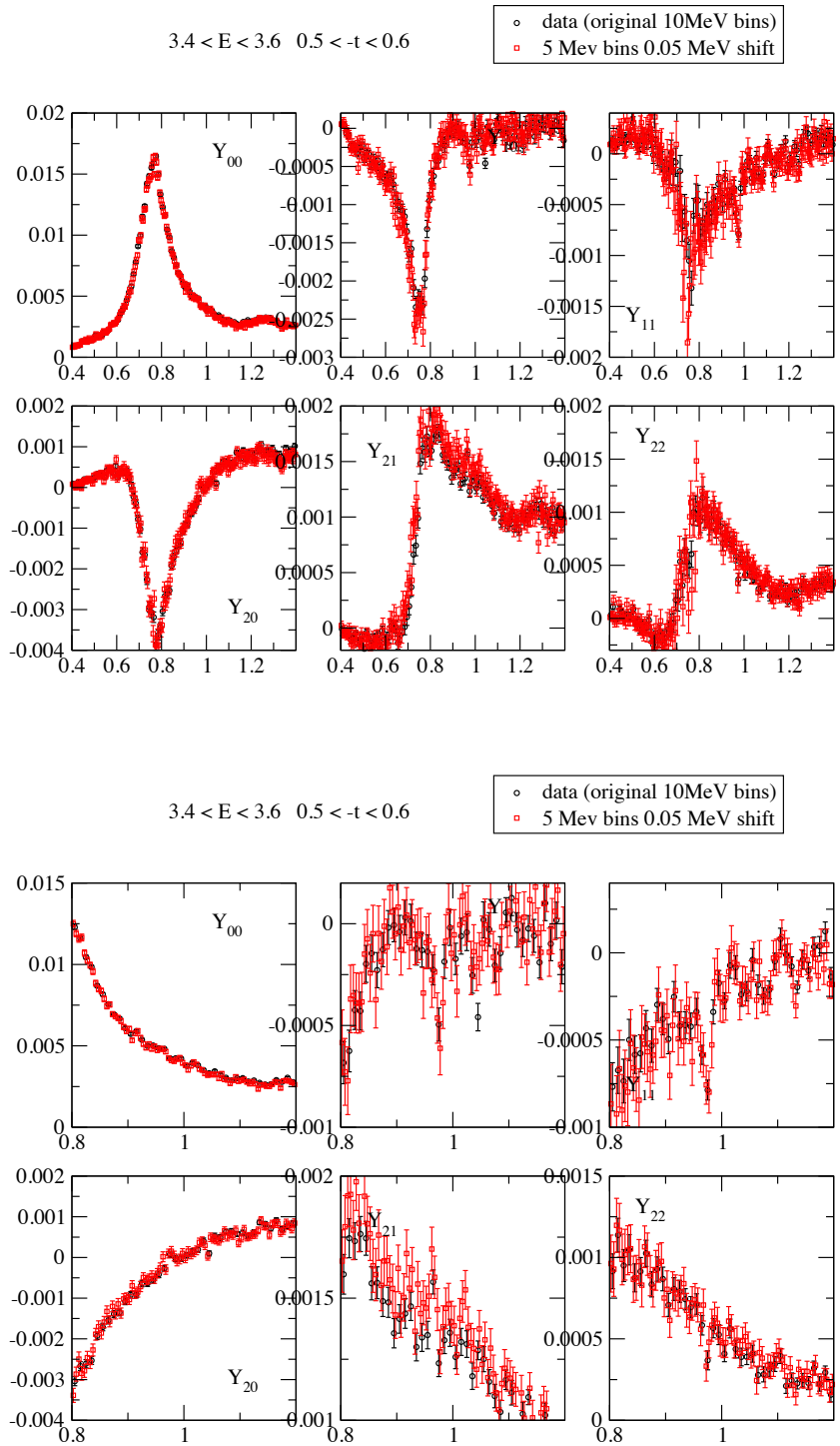

Figure A.21: Comparison of moments extracted with a finer binning (5 MeV) respect to the standard (10 MeV). The bottom figure shows a zoom in the $f_0(980)$ region.

$$\langle Y_{10} \rangle = SP_0^* + S^* P_0 + \sqrt{\frac{3}{5}} P_- D^* - \cdots \tag{A.2}$$

It is clear that any analysis would require a truncation in the number of terms on the right hand side. Nevertheless it should also be obvious that certain features of $\pi\pi$ amplitudes can be reliability extracted even when such truncation is made while other are not. For example the f_0 has a rapid mass dependence, and in $\langle Y_{10} \rangle$ appears in two terms only, through interference with the P wave. All other terms in $\langle Y_{10} \rangle$ add up to a smooth background near the f_0 mass. Similarly, near the ρ (which is much broader but also much stronger) it is the S and D waves only that contribute via interference with the P-wave and produce the ρ-like variation in the moment with all other terms contributing to a background. On the other hand the extraction of other states, as the σ meson, due to the large width may be strongly contaminated by truncation and can not be extracted with this procedure.
In summary the truncation in the number of partial waves used to describe moments is expected to be a good approximation when describing narrow $\pi\pi$ resonances which contribute to individual partial waves. The remaining background can be described with a smooth function.

A.5.2 Extraction of the resonant part of waves

Fitting experimental moments we extracted partial waves using the parametrization described in Appendix C. Using dispersion relations, amplitudes can be written as function of $s = M_{\pi\pi}^2$ for each L-wave, as:

$$a(s) = \frac{1}{2}[I + S(s)]a^L(s) - \frac{1}{\pi} D^{-1}(s) PV \int_{s_{th}} ds' \frac{N(s')\rho(s')a^L(s')}{s' - s} \tag{A.3}$$

where:
- I and S are matrix in multi-channel space ($\pi - \pi$, $K - K$); - $N(s)$ and $D(s)$ can be written in terms of the scattering matrix of $\pi - \pi$ scattering, chosen to reproduce the known phase shift and inelasticities; - $a^L(s)$ represents our ignorance about the production process. Since discontinuities are taken into account by functions N and D, $a^L(s)$, does not have singularities and can be expanded in a polynomial. The polynomial parameters (see Appendix. C of the analysis note for details) are the PWA fit parameters. The imaginary part of the integral in the equation above, represents the production of long-lived two-mesons (on-shell) meson pairs corresponding to the non-resonant part of the scattering process. The Real part of the same integral represents the direct resonant production that, in absence of the on-shell part, would lead to the typical Breit-Wigner shape. This is what we used to derive the resonance (in particular $f_0(980)$) cross sections. It should be noticed that parameters defining the amplitude above, are extracted fitting the whole $M_{\pi\pi}$ spectrum using constraints from hadronic data. The resonant and non-resonant part of the amplitudes are then computed from the fitted parameters. Errors on the parameters are given by MINUIT and propagated to the final amplitude. To propagate the systematic error associated to the experimental moment extraction, the fit was performed independently on the 4 sets of experimental moments described in Par.4.3 of this note. Figures A.22 and A.23 show the individual fit results (top panel), and the combination of the four (bottom) for the whole and resonant part of the $S - wave$.

The four results were combined together as average. The errors were computed combining in quadrature the following contributions:
- the statistical error as it comes from MINUIT;
- the systematic error associated to the fit procedure estimated as variance of the 4 sets of results described above;
- error from photon flux normalization and data analysis estimated to be of the order of 10%.
The dominant contribution to the final error comes from the systematic difference between the four sets of fits. The relation between errors on the full and resonant part of the wave is not trivially related to the parametrization of the amplitude.

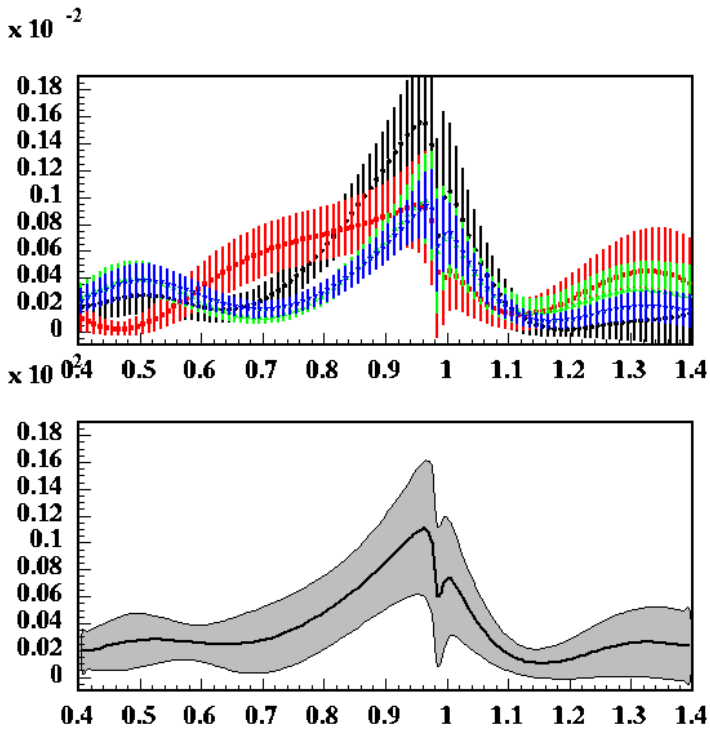

Figure A.22: The whole $S-wave$ obtained by fitting moments extracted with the four methods described in the text. Top panel: fit results obtained using *Method 1* (black), *Method 2a* (red), *Method 2b* (green) and *Method 2c* (blue). Bottom panel: combination of the four fit results.

Final state interaction

The $S-wave$ parametrization used in the fit does include effects beyond $\pi\pi$ scattering, *e.g.* production of baryon resonances or meson-baryon rescattering. Each partial wave amplitude, (S, or P, or D etc.) for given momentum transfer $-t$ and photon energy E_γ is a function of a single variable – the $\pi\pi$ invariant mass, $M_{\pi\pi}$. It is important to realize that a single partial wave amplitude "knows" about all hadronic processes (including baryon resonance production). In the analysis of partial waves one possible approach, would be to build a model of various hadronic processes, project onto a particular $\pi\pi$ partial wave and determine any free parameters in the hadronic model by fitting the $\pi\pi$ moments. In our analysis, however we have taken a route that relies less on the specific model for hadronic process. Our approach can be summarized as follows. Independently on the specifics of the underlying hadronic processes, the $M_{\pi\pi}$ dependence of partial waves is constrained by analyticity and Cauchy theorem leading to a relation between amplitude and its singularities. The singularities are determined by the known $\pi\pi$ phase shifts and unknown functions of $M_{\pi\pi}$ that, for example, contain information about $\pi\pi$ production from various hadronic sources. Another important observation is that these unknown functions have no singularities for physical values of $M_{\pi\pi}$ (where data exists) and thus can be parametrized as regular (*e.g* polynomial) functions. Parameters of these polynomials are determined by fitting moments rather than being specified by any given model.

A.5.3 Conclusions

In summary:

1 The fit parameters in partial waves do account for all hadronic processes that contribute to a given partial wave. Since the functional form is constrained by analyticity the number

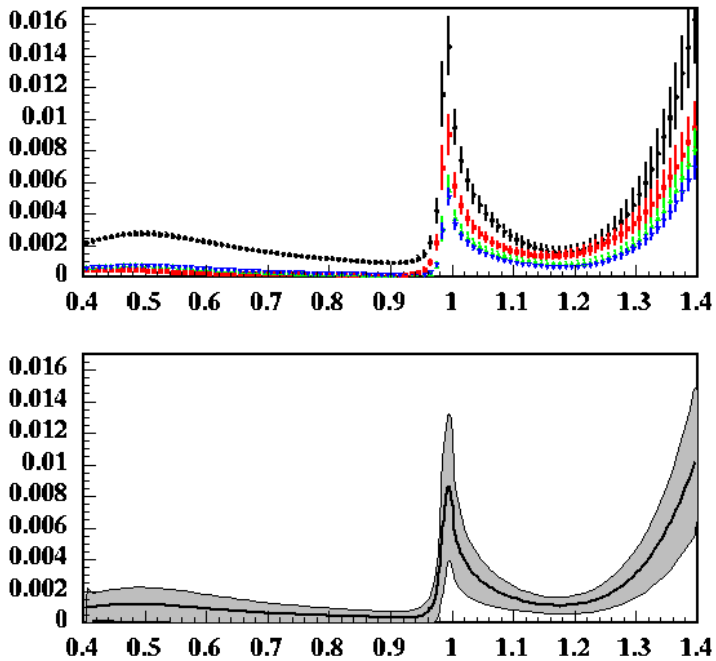

Figure A.23: The resonant part of the $S - wave$ obtained by fitting moments extracted with the four methods described in the text. Top panel: fit results obtained using *Method 1* (black), *Method 2a* (red), *Method 2b* (green) and *Method 2c* (blue). Bottom panel: combination of the four fit results.

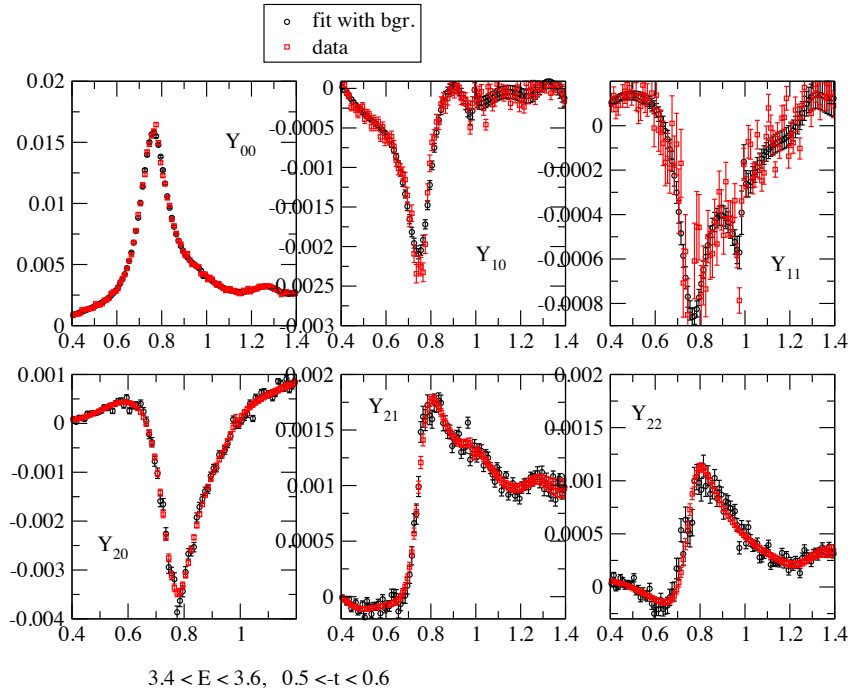

Figure A.24: Fit of the moments when a 2nd order polynomial background has been added to the expansion in partial waves. Experimental moments are plot in black while the fit result is in red.

of parameters can be controlled by a number of terms in a Taylor expansion (order of polynomial).

2 Truncation in the number of partial waves used to describe moments is expected to be a good approximation when describing narrow $\pi\pi$ resonances which contribute to individual partial waves.

We have tested these approximations by

Ad.1 varying the number of parameters in the polynomial expansion. We did fits using 4th order polynomials and 2nd order polynomials.

Ad.2 including incoherent (per Eq. A.2) polynomials in $M_{\pi\pi}$ to describe the effect of eliminated terms in the truncation of the moments.

Figure A.24 shows the results of fit of the moments with polynomial background included. Figure A.25 shows the separated contribution of the polynomial background (in green) and the remaining part (in black). The sum of the two contributions gives the fit result shown in fig. A.24. From this check we conclude that background contribution is small, smooth and does not affect the quality of the fit. Figure A.26 shows the extracted waves when the polynomial background is included in the fit (in black) and the contribution of the waves after background subtraction.

The comparison, for both the full wave and the resonant part only, shows that the $P-wave$ and the $S-wave$ in the $f_0(980)$ region are only slightly affected by the inclusion of this additional background. On the contrary, the low mass $S-wave$, corresponding to the $\sigma(600)$ region, and the $D-wave$, corresponding to the $f_2(1270)$ region, shows a significant variation and therefore

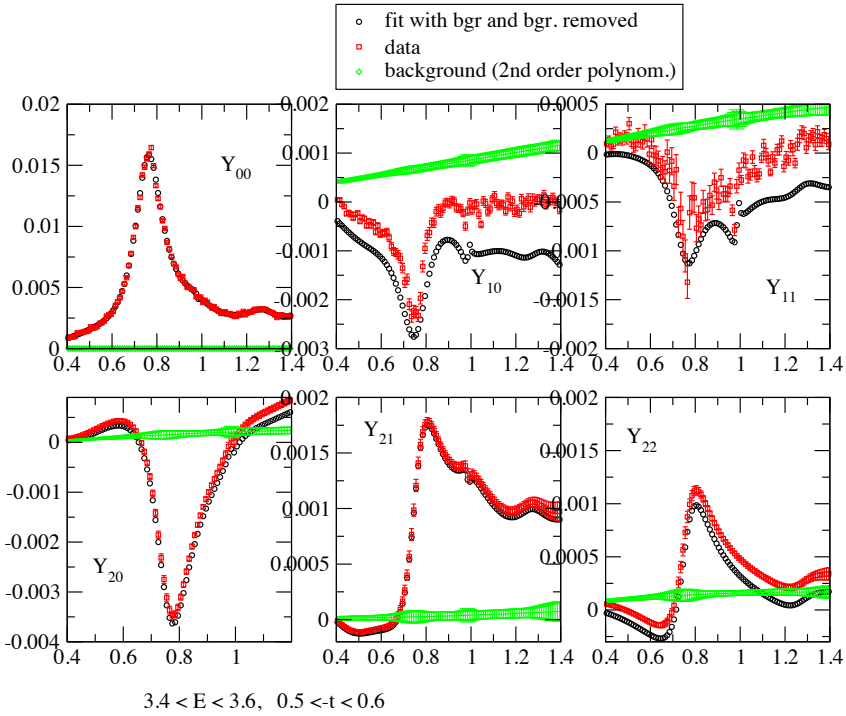

Figure A.25: Separated contribution of the background (green) and partial wave expansion (black). Experimental moments are plot in red.

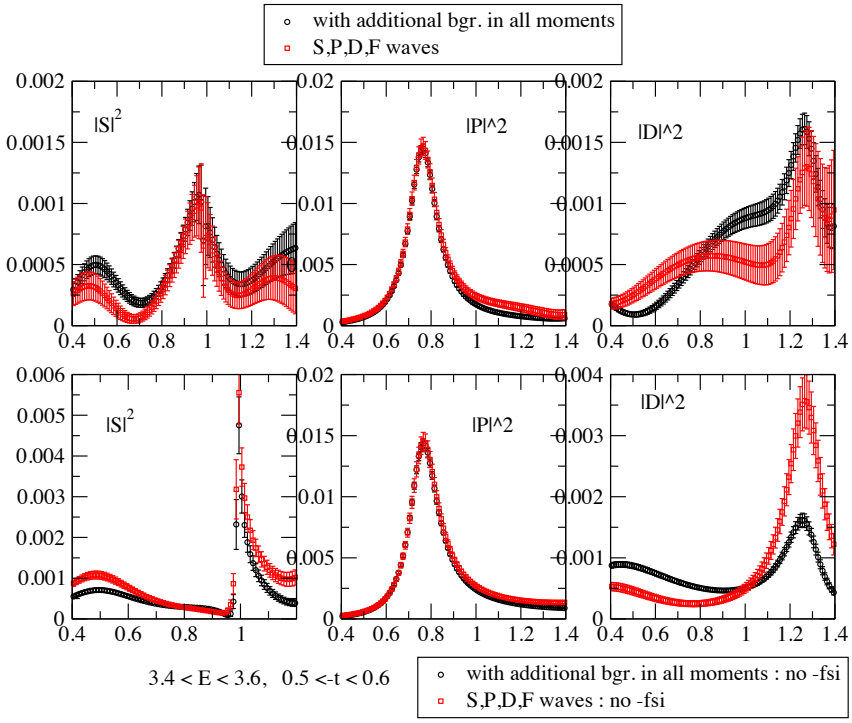

Figure A.26: Extracted $S, P, D - waves$ with the polynomial background included (black) and without (red). In the top panel, the whole waves are shown while in the bottom, only the resonant part.

a more complete analysis should be perform to extract reliable information in these mass ranges.

From the above systematic check we estimated an error on the background subtraction of 20% on the f_0 cross section that will be added in quadrature to the final quoted error.

Appendix B

Higher moments

The explicit expressions for the moments in terms of partial waves are given by

$$\langle Y_{00}\rangle = N\Big[|S|^2 + |P_-|^2 + |P_0|^2 + |P_+|^2 + |D_-|^2 \\ +|D_0|^2 + |D_+|^2 + |F_-|^2 + |F_0|^2 + |F_+|^2\Big] \tag{B.1}$$

$$\langle Y_{10}\rangle = N\Bigg[SP_0^* + P_0S^* + \sqrt{\frac{3}{5}}\left(P_-D_-^* + P_-S^* + P_+D_+^* + D_+P_+^*\right) \\ +\sqrt{\frac{4}{5}}\left(P_0D_0^* + D_0P_0^*\right) + \sqrt{\frac{24}{35}}\left(D_-F_-^* + F_-D_-^* + D_+F_+^* + F_+D_+^*\right) + \sqrt{\frac{216}{280}}\left(D_0F_0^* + F_0D_0^*\right)\Bigg] \tag{B.2}$$

$$\langle Y_{11}\rangle = N\Bigg[\sqrt{\frac{1}{2}}\left(-P_-S^* - SP_-^* + P_+S^* + SP_+^*\right) + \sqrt{\frac{1}{20}}\left(P_-D_0^* + D_0P_-^* - P_+D_0^* - D_0P_+^*\right) \\ +\sqrt{\frac{3}{20}}\left(-P_0D_-^* - D_-P_0^* + P_0D_+^* + D_+P_0^*\right) + \sqrt{\frac{9}{140}}\left(D_-F_0^* + F_0D_-^* - D_+F_0^* - F_0D_+^*\right) \\ +\sqrt{\frac{9}{70}}\left(-D_0F_-^* - F_-D_0^* + D_0F_+^* + F_+D_0^*\right)\Bigg] \tag{B.3}$$

$$\langle Y_{20}\rangle = N\Bigg[SD_0^* + D_0S^* + \sqrt{\frac{1}{5}}\left(2|P_0|^2 - |P_-|^2 - |P_+|^2 + |F_-|^2 + |F_+|^2\right) \\ +\sqrt{\frac{18}{35}}\left(P_-F_-^* + F_-P_-^* + P_+F_+^* + F_+P_+^*\right) + \sqrt{\frac{27}{35}}\left(P_0F_0^* + F_0P_0^*\right) + \sqrt{\frac{5}{49}}\left(|D_-|^2 + |D_+|^2\right) \\ +\sqrt{\frac{20}{49}}|D_0|^2 + \sqrt{\frac{16}{45}}|F_0|^2\Bigg] \tag{B.4}$$

$$\langle Y_{21}\rangle = N\Bigg[\frac{1}{2}\left(SD_+^* + D_+S^* - SD_-^* - D_-S^*\right) + \sqrt{\frac{3}{20}}\left(P_0P_+^* + P_+P_0^* - P_-P_0^* - P_0P_-^*\right) \\ +\sqrt{\frac{9}{140}}\left(P_-F_0^* + F_0P_-^* - P_+F_0^* - F_0P_+^*\right) + \sqrt{\frac{6}{35}}\left(P_0F_+^* + F_+P_0^* - P_0F_-^* - F_-P_0^*\right)$$

$$+\sqrt{\frac{5}{196}}\left(D_0D_+^* + D_+D_0^* - D_0D_-^* - D_-D_0^*\right) + \sqrt{\frac{1}{90}}\left(F_0F_+^* + F_+F_0^* - F_0F_-^* - F_-F_0^*\right)\Bigg] \tag{B.5}$$

$$\langle Y_{22}\rangle = N\Bigg[\sqrt{\frac{3}{10}}\left(P_-P_+^* + P_+P_-^*\right) + \sqrt{\frac{3}{140}}\left(P_-F_+^* + F_+P_-^* + P_+F_-^* + F_-P_+^*\right)$$
$$+\sqrt{\frac{4}{30}}\left(-F_+F_-^* - F_-F_+^*\right) + \sqrt{\frac{3}{196}}\left(-D_-D_+^* - D_+D_-^*\right)\Bigg] \tag{B.6}$$

$$\langle Y_{30}\rangle = N\Bigg[SF_0^* + F_0S^* + \sqrt{\frac{18}{70}}\left(-P_-D_-^* - D_-P_-^* - P_+D_+^* - D_+P_+^*\right) + \sqrt{\frac{108}{140}}\left(P_0D_0^* + D_0P_0^*\right)$$
$$+\sqrt{\frac{2}{45}}\left(D_-F_-^* + F_-D_-^* + D_+F_+^* + F_+D_+^*\right) + \sqrt{\frac{16}{45}}\left(D_0F_0^* + F_0D_0^*\right)\Bigg] \tag{B.7}$$

$$\langle Y_{31}\rangle = N\Bigg[\frac{1}{2}\left(SF_+^* + F_+S^* - SF_-^* - F_-S^*\right) + \sqrt{\frac{18}{140}}\left(P_+D_0^* + D_0P_+^* - P_-D_0^* - D_0P_-^*\right)$$
$$+\sqrt{\frac{6}{35}}\left(P_0D_+^* + D_+P_0^* - P_0D_-^* - D_-P_0^*\right) + \sqrt{\frac{1}{90}}\left(D_+F_0^* + F_0D_+^* - D_-F_0^* - F_0D_-^*\right)$$
$$+\sqrt{\frac{1}{20}}\left(D_0F_+^* + F_+D_0^* - D_0F_-^* - F_-D_0^*\right)\Bigg] \tag{B.8}$$

$$\langle Y_{32}\rangle = N\Bigg[\sqrt{\frac{3}{14}}\left(-P_+D_-^* - D_-P_+^* - P_-D_+^* - D_+P_-^*\right) + \sqrt{\frac{1}{12}}\left(-D_+F_-^* - F_-D_+^* - D_-F_+^* - F_+D_-^*\right)\Bigg] \tag{B.9}$$

$$\langle Y_{40}\rangle = N\Bigg[\sqrt{\frac{2}{7}}\left(-P_+F_+^* - F_+P_+^* - P_-F_-^* - F_-P_-^*\right) + \sqrt{\frac{16}{21}}\left(P_0F_0^* + F_0P_0^*\right) + \sqrt{\frac{16}{49}}\left(-|D_+|^2 - |D_-|^2\right)$$
$$+\sqrt{\frac{36}{49}}|D_0|^2 + \sqrt{\frac{36}{121}}|F_0|^2 + \sqrt{\frac{1}{121}}\left(|F_+|^2 + |F_-|^2\right)\Bigg] \tag{B.10}$$

$$\langle Y_{41}\rangle = N\Bigg[\sqrt{\frac{5}{42}}\left(P_+F_0^* + F_0P_+^* - P_-F_0^* - F_0P_-^*\right) + \sqrt{\frac{5}{28}}\left(P_0F_+^* + F_+P_0^* - P_0F_-^* - F_-P_0^*\right)$$
$$+\sqrt{\frac{30}{196}}\left(D_0D_+^* + D_+D_0^* - D_-D_0^* - D_0D_-^*\right) + \sqrt{\frac{30}{968}}\left(F_0F_+^* + F_+F_0^* - F_0F_-^* - F_-F_0^*\right)\Bigg] \tag{B.11}$$

$$\langle Y_{42}\rangle = N\Bigg[\sqrt{\frac{5}{28}}\left(-P_+F_-^* - F_-P_+^* - P_-F_+^* - F_+P_-^*\right) + \sqrt{\frac{10}{49}}\left(-D_-D_+^* - D_+D_-^*\right)$$
$$+\sqrt{\frac{10}{121}}\left(-F_-F_+^* - F_+F_-^*\right)\Bigg] \tag{B.12}$$

Appendix C

Two-body partial wave amplitudes

Strong interaction $\pi\pi$ amplitude play a central role in determining $\pi\pi$ photoproduction amplitudes. Here we summarize some basic properties of the $\pi\pi$ amplitudes and give specific parametrization for the $D(s)$ and $N(s)$ functions for each partial wave. For a specific partial wave determined by the total isospin-I and angular momentum-l the scattering operator acts in the particle channel space $\alpha, \beta = \pi\pi, K\bar{K}$ and it is given by (including only two-body channels)

$$S_{\alpha,\beta} = \delta_{\alpha,\beta} - 2it_{\alpha,\beta}(s)\rho_\beta(s) \tag{C.1}$$

where $t_{\alpha,\beta} = t^{l,I}(s)_{\alpha,\beta}$ is the scattering amplitude between channels α, β normalized such that

$$\frac{d\sigma_I}{dt} = \frac{1}{64\pi s k_\alpha^2} |\sum_l t^{l,I}(s)(2l+1)P_l(\cos\theta)|^2 \tag{C.2}$$

and $\rho_\beta(s) = k_\beta/8\pi\sqrt{s} = \sigma_\beta(s)/16\pi$, $\sigma_\beta = \sqrt{1 - 4m_\beta^2/s}$ is the phase space in the channel β. Unitarity, $SS^\dagger = 1$ implies (for each l, I),

$$\text{Im } t_{\alpha\beta}(s) = \frac{1}{2i}\left[t_{\alpha\beta}(s) - t^\dagger_{\alpha\beta}(s)\right] = -\sum_\gamma t_{\alpha\gamma}(s)\rho_\gamma(s)t^\dagger_{\gamma\beta}(s) \tag{C.3}$$

or

$$\text{Im } t^{-1}_{\alpha\beta}(s) = \frac{1}{2i}\left[t^{-1}(s)_{\alpha\beta} - t^{-1*}_{\alpha\beta}(s)\right] = \rho_\alpha(s)\delta_{\alpha\beta} \tag{C.4}$$

When amplitudes are analytically continued to complex s-plane, the physical amplitudes are defined as the limit $a_{phys}(s) = a(s + i\epsilon) \equiv a(s^+)$. Reflection positivity of analytical functions, $a(s^*) = a^*(s)$ than relates the phase space factor to the discontinuity in the analytical functions representing scattering amplitudes across the right hand cut

$$t^{-1}(s) - t^{-1*}(s) = t^{-1}(s + i\epsilon) - t^{-1}(s - i\epsilon) \equiv t^{-1}(s^+) - t^{-1}(s^-) = 2i\rho(s) \tag{C.5}$$

It is convenient to separate the right hand from left hand singularities by introducing a parametrization (for each l, I),

$$t_{\alpha\beta}(s) = [D^{-1}(s)N(s)]_{\alpha\beta} \tag{C.6}$$

where $D, (N)$ are matrices in the channel space that have only right (left) hand cut singularity. From unitarity it than follows,

$$N^{-1}(s^+)D(s^+) - N^{-1}(s^-)D(s^-) = 2i\rho \tag{C.7}$$

Since N has no cuts for positive s, $N(s^+) = N(s^-) = N(s)$ and

$$D(s^+) - D(s^-) = 2iN(s)\rho(s) = 2iD(s^+)t(s)\rho(s) = D(s^+)\left[1 - S(s)\right] \tag{C.8}$$

which enables to relate the discontinuity of the denominator function D across the right hand cut to the S-matrix,

$$S(s) = D^{-1}(s^+)D(s^-) \tag{C.9}$$

Since $D(s)$ has only the right hand cut, Cauchy theorem leads to a dispersion relation

$$D(s) = \frac{1}{2\pi i}\int_{s_{th}} ds' \frac{D(s'^+) - D(s'^-)}{s' - s} = \frac{1}{\pi}\int_{s_{th}} ds' \frac{D(s')t(s')\rho(s')}{s' - s} = \frac{1}{\pi}\int_{s_{th}} ds' \frac{N(s')\rho(s')}{s' - s} \tag{C.10}$$

possibly with subtractions and it is understood that the functions in numerator under the integral are to be taken on the upper lip of the positive s' line, *i.e.* with $s' + i\epsilon$. The lower limit of integration is given by the starting point of the right hand cut (*e.g.* $s_{th} = 4m_\pi^2$ for $\pi\pi$) The role of subtractions is to remove high-s' component of the integral. This is necessary if the S-matrix elements do not decrease fast enough with energy which is the case in diffractive scattering. However even if the integral is finite subtractions are effective in improving convergence. Finally in theoretical based on low-energy expansion motivated by effective field theory methods the function N is known for low s' only and subtractions are introduced to remove the region of integration where N is not known. For example with one subtraction

$$D(s) = D(s_0) + \frac{s - s_0}{\pi}\int_{s_{th}} ds' \frac{D(s')t(s')\rho(s')}{(s' - s)(s' - s_0)} = \frac{s - s_0}{\pi}\int_{s_{th}} ds' \frac{N(s')\rho(s')}{(s' - s)(s' - s_0)} \tag{C.11}$$

Since $D(s_0)$ is a constant it can be absorbed by re-scaling D and N and it is allows possible to write

$$D(s) = 1 + \frac{s - s_0}{\pi}\int_{s_{th}} ds' \frac{D(s')t(s')\rho(s')}{(s' - s)(s' - s_0)} = 1 + \frac{s - s_0}{\pi}\int_{s_{th}} ds' \frac{N(s')\rho(s')}{(s' - s)(s' - s_0)} \tag{C.12}$$

The crucial point here is that this expresses D entirely in terms of measurable quantities determined by phase shifts and inelasticities via the S matrix. The solution to Eq. C.8 can found from Eq. C.9

$$\ln D(s^+) - \ln D(s^-) = -\ln S(s) \tag{C.13}$$

Defining $F(s) \equiv \ln D(s)$ which has the same cuts as D one can write a dispersion relation,

$$F(s) = -\frac{1}{2\pi i}\int_{s_{th}} ds' \frac{\ln S(s')}{s - s'} \tag{C.14}$$

(possibly with subtractions), and therefore obtain an explicit solution for D in terms of S,

$$D(s) = \exp\left(-\frac{1}{2\pi i}\int_{s_{th}} ds' \frac{\ln S(s')}{s - s'}.\right) \tag{C.15}$$

If one subtraction is used, with D given by Eq. C.12 we have instead

$$\begin{aligned} F(s) &= F(s_0) - \frac{(s - s_0)}{2\pi i}\int_{s_{th}} ds' \frac{\ln S(s')}{(s' - s)(s' - s_0)} \\ D(s) &= D(s_0)\exp\left(-\frac{s - s_0}{2\pi i}\int_{s_{th}} ds' \frac{\ln S(s')}{(s' - s)(s' - s_0)}\right) \end{aligned} \tag{C.16}$$

with $D(s_0) = 1$ according to the normalization in Eq. C.12. In summary, the discontinuity across the right hand cut in the partial waves can be determined from data, *i.e* phase shifts and inelasticities. The complete partial wave amplitude $t(s) = t^{l,I}(s)$ involves also the function $N(s) = N^{l,I}(s)$ which can can in principle be determined, using Couchy relations, through its discontinuity on the left hand cut. This in general is related to physical thresholds in crossed channel reactions. Fr example in the case of $\pi\pi \to \pi\pi$ amplitudes cross channels involve the same

amplitudes and cuts of N can also be related to the same phase shifts and inelasticities albeit involving all partial waves. This is leads to the so called Roy equations. In practice one does not know the S-matrix elements for all partial waves and all energies and the Omnes integrals (Eq. C.15, C.16) are often computed using an analytical approximations/parametrization of the S-matrix elements.

In our analysis we will use a parametrization from for D that fits the $\pi\pi$ data to constrain $\pi\pi$ photo-production amplitudes. In particular we will employ the parametrization of Oset *et al.* [7] which leads to simple analytical expressions. In Appendix B is reported the explicit parametrization of the $\pi\pi$ scattering and the photo-production amplitudes in the isospin basis as a function of s.

C.1 Parametrization of individual $\pi\pi$ amplitudes

The parametrization of the low energy $\pi\pi$ amplitudes is often made based on the low energy expansion controlled by chiral symmetry. In particular in Ref. [**?**], lowest order chiral langrangian was used to construct the function $N(s)$ representing effectively the $\pi\pi$ potential,

$$N(s) = A + Bs + Cs^4 + \cdots, \tag{C.17}$$

where $A, B, C, \cdots$ are s-independent matrix in the channel space, *i.e* $A = A_{\alpha\beta}$ with $\alpha = 1$ corresponding to $\pi\pi$ $\alpha = 2$ to $K\bar{K}$ which are sufficient for energies below 1.4 GeV. As discussed earlier subtractions can be used to rome the integration region for large energies, where N is not known. Below we discuss the individual partial waves

C.1.1 $(l, I) = (0, 0)$

In this case N, and D are 2×2 matrices and C and higher order terms in the expansion of N were ignored . With $N(s)$ being a first order polynomial in s subtractions are introduces in a somewhat different albeit equivalent fashion to that described in Sec. C. The D -matrix given by Eq. C.10,

$$D(s^{\pm}) = 1 + I(s^{\pm}) \tag{C.18}$$

with

$$\begin{aligned} I(s^{\pm}) &\equiv \frac{1}{\pi}\int_{s_{th}} ds' \frac{N(s')\rho(s')}{s' - s^{\pm}} - 1 \\ &= -1 + \frac{1}{\pi}\int_{s_{th}} ds' \frac{B(s'-s)\rho(s')}{s'-s} + (A + Bs)\frac{1}{\pi}\int_{s_{th}} ds' \frac{\rho(s')}{s' - s^{\pm}} \\ &\equiv a(s_0) + b(s_0)s + N(s)G(s, s_0) \pm iN(s)\rho(s) \end{aligned} \tag{C.19}$$

where G is the Chew-Mandelstam (matrix) function given by

$$\begin{aligned} G(s, s_0) &= \frac{(s - s_0)}{\pi} P.V. \int_{s_{th}} ds' \frac{\rho(s')}{(s'-s)(s'-s_0)} \\ &= -\frac{1}{(4\pi)^2} \begin{cases} \sqrt{1 - \frac{4s_{th}}{s}} \ln \frac{1+\sqrt{1+\frac{4s_{th}}{s}}}{1-\sqrt{1-\frac{4s_{th}}{s}}} & \text{for } s > s_{th} \\ 2\sqrt{\frac{4s_{th}}{s} - 1} \arctan\left(\frac{1}{\sqrt{\frac{4s_{th}}{s}-1}}\right) & \text{for } s_{th} > s > 0 \\ \sqrt{1 - \frac{4s_{th}}{s}} \ln \frac{\sqrt{1-\frac{4s_{th}}{s}}+1}{\sqrt{1-\frac{4s_{th}}{s}}-1} & \text{for } 0 > s \end{cases} \\ &- (s \to s_0) \end{aligned} \tag{C.20}$$

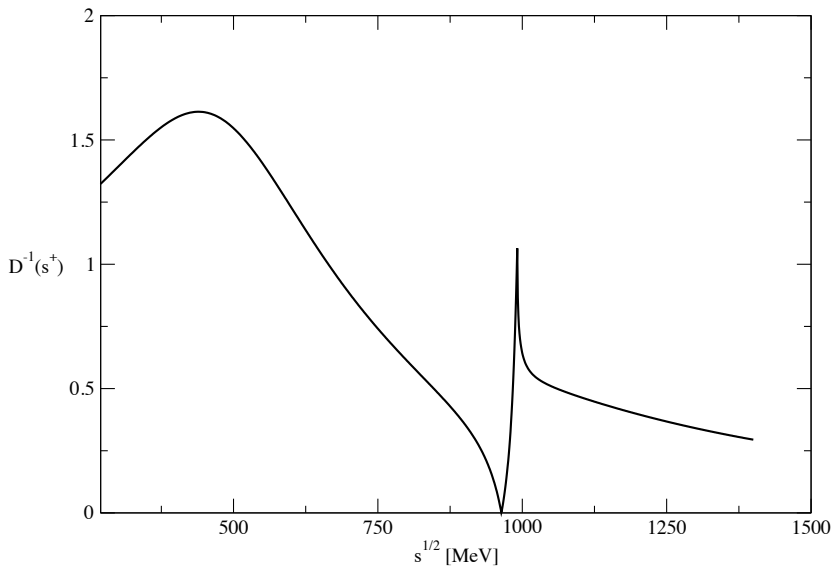

Figure C.1: $\pi\pi$ components of the magnitude of the inverse of the denominator function for isoscalar S wave.

and $a(s_0)$ and $b(s_0)$ are constants (matrix) given by

$$\begin{aligned} a(s_0) &= -1 + \frac{B}{\pi}\text{P.V.} \int_{s_{th}} ds' \rho(s') + \frac{A}{\pi}\text{P.V.} \int_{s_{th}} ds' \frac{\rho(s')}{s' - s_0} \\ b(s_0) &= \frac{B}{\pi}\text{P.V.} \int_{s_{th}} ds' \frac{\rho(s')}{s' - s_0} \end{aligned} \tag{C.21}$$

These constants are infinite thus two subtractions are needed to make D finite, δa and δbs As discussed earlier, the s-independent term $a_(s_0)+\delta a$ in the dispersion equation for D, is irrelevant and can be set to one by re-scaling D and N. The other constant matrix $b(s_0) + \delta b$ can be used as a free parameter to be fitted to data. This leaves two (without counting the numerical A, B matrices) parameters, the matrix $b(s_0) + \delta b$ and s_0 to be determined from data. In the model of Oset *et al.* a somewhat different path was taken. For the isoscalar S- wave the numerical matrices A and B are fixed from isoscalar S-wave projection of the amplitudes calculated from the chiral Lagrangian,

$$A = \frac{1}{2f_\pi^2}\begin{pmatrix} m_\pi^2 & 0 \\ 0 & 0 \end{pmatrix} = O(1), \quad B = \frac{1}{2f_\pi^2}\begin{pmatrix} -2 & -\frac{\sqrt{3}}{2} \\ -\frac{\sqrt{3}}{2} & -\frac{3}{2} \end{pmatrix} = O(10^2 \text{ GeV}^{-2}) \tag{C.22}$$

and the matrices $a(s_0) + \delta a$ and $b(s_0) + \delta b$ were fitted to the data at a fixed value of s_0 chosen as $s_0 m_\rho^2$. Furthermore a constraint between $a(s_0) + \delta$ and $b_(s_0) + \delta b$ was imposed so that

$$a(s_0) + \delta a + [b(s_0) + \delta b]s = const. \times (A + Bs) + O(m_\pi/m_K) \tag{C.23}$$

with the correction term originating from a difference in thresholds in the $\pi\pi$ and $K\bar{K}$ channels. From fitting to the data one finds,

$$a(m_\rho^2) = \frac{10^{-2}}{2f_\pi^2}\begin{pmatrix} 1.27m_\pi^2 & 0 \\ 0 & 0 \end{pmatrix} = O(10^{-2})A,$$

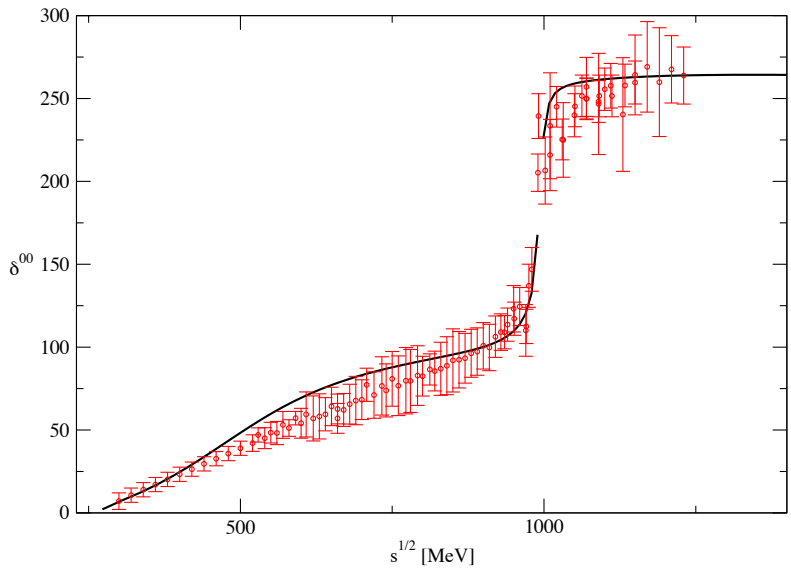

Figure C.2: $\pi\pi$ scalar-isoscalar phase shift

$$b(m_\rho^2) = \frac{10^{-2}}{2f_\pi^2}\begin{pmatrix} -2\times 1.27 & -\frac{\sqrt{3}}{2}\times 0.73 \\ -\frac{\sqrt{3}}{2}\times 1.27 & -\frac{3}{2}\times 0.73 \end{pmatrix} = O(10^{-2})B \tag{C.24}$$

The modulus of $D^{-1}(s^+)$ is shown in Fig. C.1 and the $\pi\pi$ phase shift given in terms of the S matrix by

$$S = \begin{bmatrix} \eta e^{2i\delta_{\pi\pi}} & i(1-\eta^2)^{1/2}e^{i(\delta_{\pi\pi}+\delta_{K\bar{K}})} \\ i(1-\eta^2)^{1/2}e^{i(\delta_{\pi\pi}+\delta_{K\bar{K}})} & \eta e^{2i\delta_{K\bar{K}}} \end{bmatrix} \tag{C.25}$$

is compared to data in Fig. C.2 One might argue that the model of Oset *et al.* is somewhat *ad hoc*, for example one could fix (a and fit b as discussed earlier) It is important to realize that as far as determining D any parametrization that reproduces the cross section is equally acceptable.

C.1.2 $(l, I) = (1, 1)$

It is well known that to represent the main feature – the ρ meson of the isovector P-wave it is necessary to consider terms at least up to order s^2 in the expansion in Eq. C.17,

$$N(s) = A + Bs + Cs^2 \tag{C.26}$$

Furthermore the ρ primality to the $\pi\pi$ channel and is sufficient to consider N and D as single functions. To implement this in the dispersion relation for D requires two subtractions

$$D(s^\pm) = a_0 + b_0 s + c_0 s^2 + N(s)G(s, s_0) \pm iN(s)\rho(s) \tag{C.27}$$

where

$$\begin{aligned} a_0 &= \frac{A}{\pi}\int ds' \frac{\rho(s')}{s-s_0} + \frac{B}{\pi}\int ds'\rho(s') + \frac{C}{\pi}\int ds' s'\rho(s') \\ b_0 &= \frac{B}{\pi}\int ds' \frac{\rho(s')}{s-s_0} + \frac{C}{\pi}\int ds'\rho(s') \end{aligned}$$

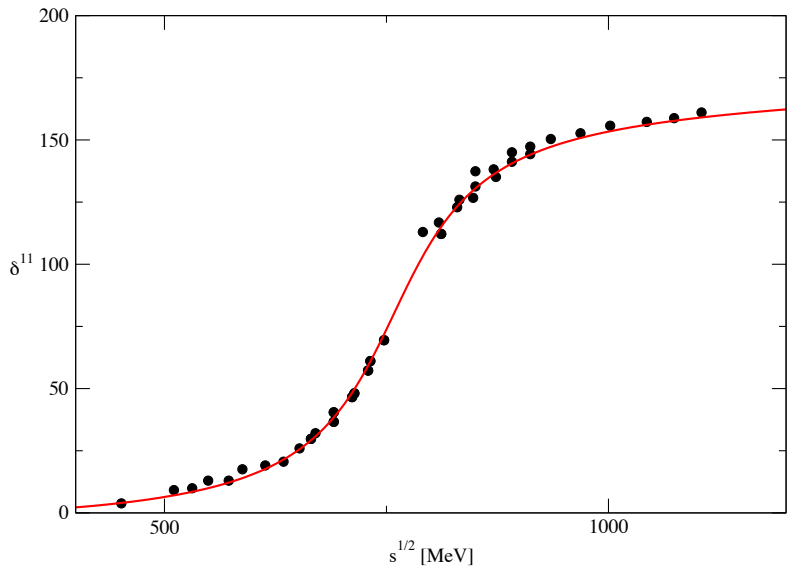

Figure C.3: $\pi\pi$ vector-isovector phase shift

$$c_0 = \frac{C}{\pi}\int ds' \frac{\rho(s')}{s-s_0} \tag{C.28}$$

Again it is convenient to normalize D so that in the chiral limit at low energies ($A \to 0$, $s \to 0$), $D = 1$ which amounts to resealing by a_0. Fitting to P - wave data gives

$$\begin{aligned} &A = 1.57, \quad B = -22.20 \text{ GeV}^{-2}, C = 4.47 \text{ GeV}^{-4} \\ &a_0 = 1.0, b_0 = -1.68 \text{ GeV}^{-2}, \quad c_0 = -1.79 \times 10^{-3} \text{ GeV}^{-4} \end{aligned} \tag{C.29}$$

We note, that just like in S-wave case, $A = O(1)$ *i.e* consistent with being of the order of m_π^2/f_π^2. B is of the order $O(10-100)$ GeV^2 consistent with being of the order of $1/f_\pi^2$. Finally C is consistent with being of the order of $1/f_\pi^2 m_\rho^2$ expected for interaction originating from physics at the QCD scale, $\Lambda \sim m_\rho$. The comparison of the P-wave phase shift with the one obtained from the D function given above,

$$\delta^{(1,1)}(s) = \frac{1}{2i}\ln\frac{D(s^-)}{D(s^+)} \tag{C.30}$$

is shown in Fig. C.3.

C.1.3 $(l, I) = (2, 0)$

The isoscalar D-wave is dominated by the f_2 resonance and will be parametrized using the BW approximation,

$$D(s^\pm) = 1 + b_0 s + c_0 s^2 + d_0 s^3 + N(s)G(s, s_{,0}) \pm iN(s)\rho(s), \quad N(s) = D(s - 4m_\pi^2)^2 \tag{C.31}$$

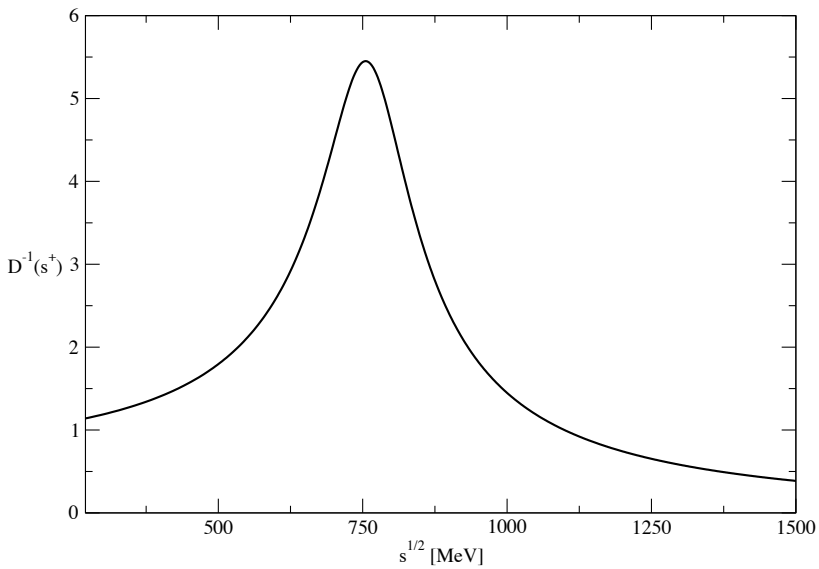

Figure C.4: Magnitude of the inverse of the denominator function for isovector P wave.

with $D = -52.74$ GeV$^{-4} = O(1/f_\pi^2\Lambda^2)$,

$$b_0 = 2.00 \text{ GeV}^{-2}, \;\; c_0 = 2.83 \text{ GeV}^{-4}, \;\; d_0 = -3.61 \text{ GeV}^{-6} \tag{C.32}$$

The plot of the phase shift is given in Fig. C.5

C.1.4 $(l, I) = (0, 2)$

The D function for the scalar-isotensor is parametrized as using one-channel chiral amplitude – the same as used to generate S -wave isoscalar but now projected onto isotensor

$$N(s) = -\frac{m_\pi^2}{f_\pi^2} + \frac{s}{2f_\pi^2} = A + Bs \tag{C.33}$$

$A = -2.37$, $B = 66.06$ GeV$^{-2} = O(1/f_\pi^2)$

$$D(s^\pm) = 1 + a_0 + b_0 s + N(s)G(s, s_0) \pm iN(s)\rho(s) \tag{C.34}$$

with $s_0 = m_\rho^2$, $a_0 = -7.93 \times 10^{-2}$, $b_0 = 2.21$ GeV$^{-2} = O(1/\Lambda^2)$ The phase shift is shown in Fig. C.7

C.1.5 Higher partial waves

In the analysis of the photoproduction data we will also use F waves. The non-trivial structure is due to the $\rho_3(1690)$ (isovector) which is outside of the $\pi\pi$ mass considered. Thus we set set $D = 1$.

C.2 Photo-production amplitudes

In Sec. 4.2.1 we derived the general, dispersion relation representation for partial waves of given spin and isospin which are valid independently for each projection of nucleon spin. Below give

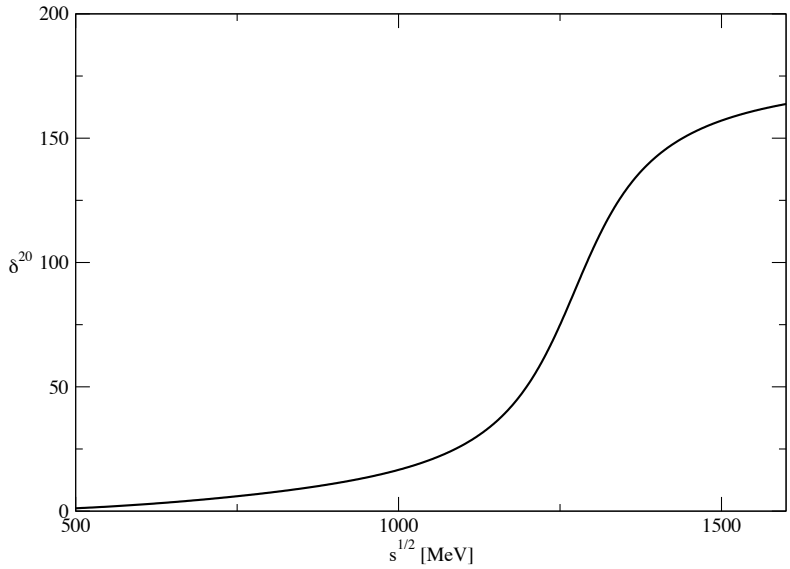

Figure C.5: $\pi\pi$ tensor-isoscalar phase shift

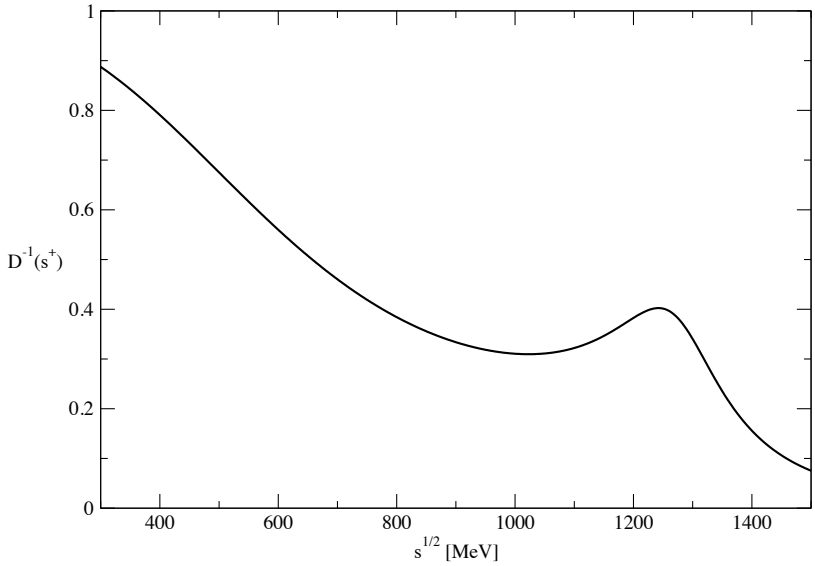

Figure C.6: Magnitude of the inverse of the denominator function for isoscalar D wave.

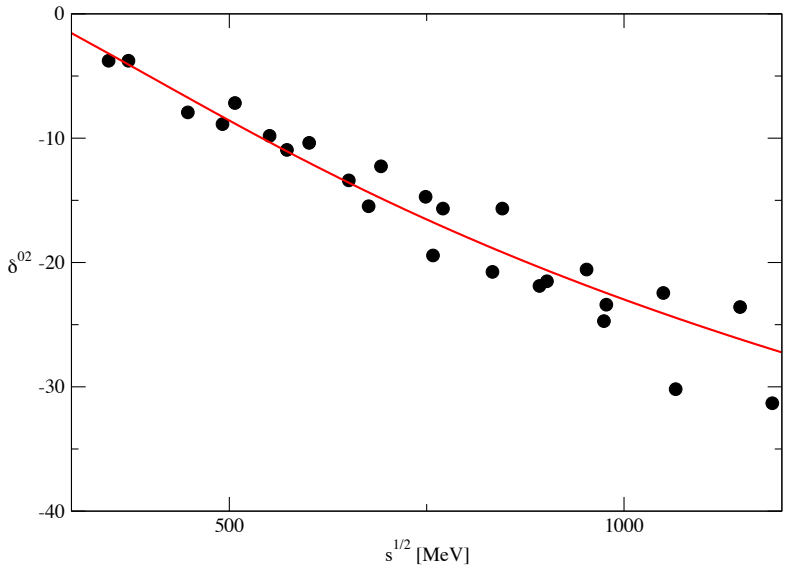

Figure C.7: $\pi\pi$ scalar-isotensor phase shift

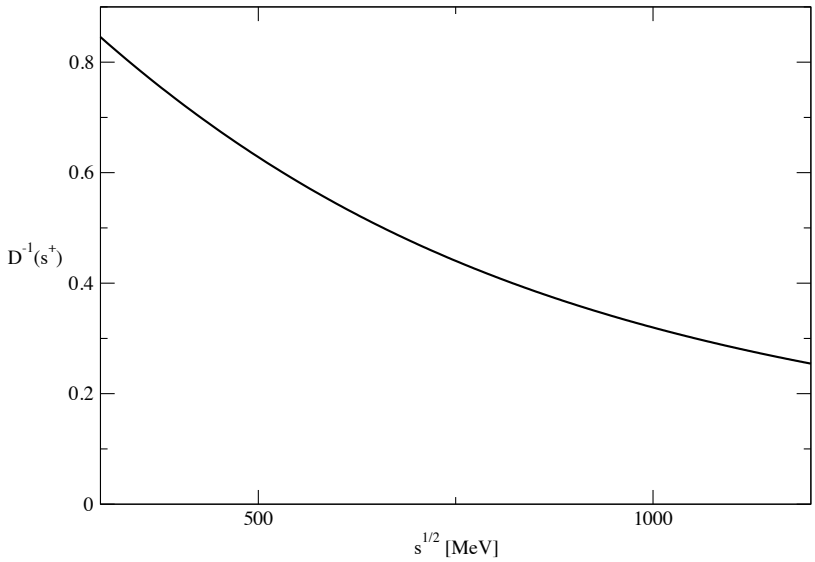

Figure C.8: Magnitude of the inverse of the denominator function for isotensor S wave.

specific formulas for individual partial waves which adopt specific parametrization of two-body amplitudes discussed above. In the following we use label $\alpha = 1, 2$ to denote the $\pi\pi, K\bar{K}$ channels, respectively. To maintain consistency with the chiral expansion used to constrain the N function in the $\pi\pi$ amplitudes, we expand the production amplitudes $\tilde{a}^L(s)$ in powers of s up to order s^2.

C.2.1 Isospin relations

The data corresponds to the $\pi^+\pi^-$ final state while the amplitudes discussed so far have well defined isospin. The correct partial waves to be compared to that data for given angular momentum and nucleon helicity are given by, for even partial waves:

$$a_{l,m,i} = \frac{1}{\sqrt{3}} a^{I=0}_{l,m,i} + \frac{1}{\sqrt{6}} a^{I=2}_{l,m,i} \tag{C.35}$$

and for odd partial waves:

$$a_{l,m,i} = \frac{1}{\sqrt{2}} a^{I=1}_{l,m,i} \tag{C.36}$$

C.2.2 (l,I) = (0,0)

With N and D corresponding the the scalar-isoscalar partial wave and $a^L(s)$ written as a second order polynomial the dispersion relation in Eq. 4.22 needs four subtractions and can be written as

$$\begin{aligned}
a(s) &= \tilde{a}^L(s) - \frac{D^{-1}(s)}{\pi} \int ds' \frac{(A + Bs')\rho(s')(\mathcal{A} + \mathcal{B}s' + \mathcal{D}s'^2)}{s' - s} \\
&= D^{-1}(s)\left[\alpha_0 + \beta_0 s + \gamma_0 s^2 + \delta_0 s^3\right] + \left[\tilde{a}^L(s) - D^{-1}(s)N(s)G(s,s_0)a^L(s) - iD^{-1}(s)N(s)\rho(s)\tilde{a}^L(s)\right] \\
&= D^{-1}(s)\left[\alpha_0 + \beta_0 s + \gamma_0 s^2 + \delta_0 s^3\right] + \left[\frac{1}{2}(S(s)+1) - t(s)G(s,s_0)\right]\tilde{a}^L(s) \\
&= D^{-1}(s)\left[\alpha_0 + \beta_0 s + \gamma_0 s^2 + \delta_0 s^3\right] + \left[\frac{1}{2}(1+S(s)) + \frac{i}{2}(1-S(s))\rho^{-1}(s)G(s,s_0)\right]\tilde{a}^L(s)
\end{aligned} \tag{C.37}$$

with

$$\tilde{a}^L(s) = \mathcal{A} + \mathcal{B}s + \mathcal{C}s^2 \tag{C.38}$$

and S and t being the S-matrix and t-matrix for the scalar-isoscalar case.

The amplitudes $a, \tilde{a}^L$ are vectors in the channel space, $a = a_\alpha$, with $\alpha = 1$ corresponding to the $\pi\pi$ and $\alpha = 2$ to the $K\bar{K}$ channel,respectively. We are interested in the $\alpha = 1$ element which is explicitly given by

$$\begin{aligned}
a_1^{(0,0)}(s) &= D^{-1}_{11}(s)\left[\alpha_{0,1} + \beta_{0,1}s + \gamma_{0,1}s^2 + \delta_{0,1}s^3\right] \\
&+ D^{-1}_{12}(s)\left[\alpha_{0,2} + \beta_{0,2}s + \gamma_{0,2}s^2 + \delta_{0,2}s^3\right] \\
&+ \left[\frac{1}{2}(1+S_{11}(s)) - t_{11}(s)G_1(s,s_0)\right](\mathcal{A}_1 + \mathcal{B}_1 s + \mathcal{C}_1 s^2) \\
&+ \left[\frac{1}{2}S_{12}(s) - t_{12}(s)G_2(s,s_0)\right](\mathcal{A}_2 + \mathcal{B}_2 s + \mathcal{C}_2 s^2) \\
&= D^{-1}_{11}(s)\left[\alpha_{0,1} + \beta_{0,1}s + \gamma_{0,1}s^2 + \delta_{0,1}s^3\right] \\
&+ D^{-1}_{12}(s)\left[\alpha_{0,2} + \beta_{0,2}s + \gamma_{0,2}s^2 + \delta_{0,2}s^3\right] \\
&+ \left[\frac{1}{2}(1+S_{11}(s)) + \frac{i}{2}(1-S(s))_{11}\rho_1^{-1}(s)G_1(s,s_0)\right](\mathcal{A}_1 + \mathcal{B}_1 s + \mathcal{C}_1 s^2) \\
&+ \left[\frac{1}{2}S_{12}(s) - \frac{i}{2}S_{12}(s)\rho_2^{-1}(s)G_2(s,s_0)\right](\mathcal{A}_2 + \mathcal{B}_2 s + \mathcal{C}_2 s^2)
\end{aligned} \tag{C.39}$$

The 14 complex parameters, $\alpha's, \beta's, \gamma', \delta's$ and $\mathcal{A}_{1,2}, \mathcal{B}_{1,2}, \mathcal{C}_{1,2}$ are 2×2 are to be determined by the fit, one set for each nucleon spin projection. Leading to a total of 56 real parameters for this wave. Note half of them represent $\pi\pi$ production through and intermediate $\pi\pi$ (subscript-1) and half through an intermediate $K\bar{K}$ (subscript-2) state.

C.2.3 (l,I) = (1,1)

The production amplitude now has a structure

$$\tilde{a}^L(s) = \left(\mathcal{A} + \mathcal{B}s + \mathcal{C}s^2\right) \tag{C.40}$$

and $[k]^l = \sqrt{1 - 4m_\pi^2/s}$. In this case N is a second order polynomial thus we need five subtractions

$$\begin{aligned} a^{(1,1)}(s) &= D^{-1}(s)\left(\alpha_0 + \beta_0 s + \gamma_0 s^2 + \delta_0 s^3 + \epsilon_0 s^4\right) \\ &+ \left[\frac{1}{2}(1+S(s)) + \frac{i}{2\rho(s)}(1-S(s))G(s,s_0)\right]\sqrt{1-\frac{4m_\pi^2}{s}}(\mathcal{A}+\mathcal{B}s+\mathcal{C}s^2) \end{aligned} \tag{C.41}$$

There a 8 complex parameters in this amplitude for each nucleon helicity state and each one of the $l = 1$, $m = \pm 1, 0$ helicity projection of the di-pion system leading to 96 real fit parameters.

C.2.4 (l,I) = (2,0)

The production amplitude now has a structure

$$\tilde{a}^L(s) = \left(\mathcal{A} + \mathcal{B}s + \mathcal{C}s^2\right) \tag{C.42}$$

$[k]^2 = (1 - 4m_\pi^2/s)$. In this case N is a second order polynomial thus we again need five subtractions

$$\begin{aligned} a^{(2,0)}(s) &= D^{-1}(s)\left(\alpha_0 + \beta_0 s + \gamma_0 s^2 + \delta_0 s^3 + \epsilon_0 s^4\right) \\ &+ \left[\frac{1}{2}(1+S(s)) + \frac{i}{2\rho(s)}(1-S(s))G(s,s_0)\right]\left(1-\frac{4m_\pi^2}{s}\right)(\mathcal{A}+\mathcal{B}s+\mathcal{C}s^2) \end{aligned} \tag{C.43}$$

leading to 96 (8 complex parameters for each one of the two nucleon helicities and $m = \pm 1, 0$ helicity projections in the di-pion system) real fit parameters.

C.2.5 (l,I) = (0,2)

The production amplitude now has a structure

$$\tilde{a}^L(s) = \left(\mathcal{A} + \mathcal{B}s + \mathcal{C}s^2\right) \tag{C.44}$$

In this case N is a first polynomial thus we again need four subtractions

$$\begin{aligned} a^{(0,2)}(s) &= D^{-1}(s)\left(\alpha_0 + \beta_0 s + \gamma_0 s^2 + \delta_0 s^3\right) \\ &+ \left[\frac{1}{2}(1+S(s)) + \frac{i}{2\rho(s)}(1-S(s))G(s,s_0)\right]\left(\mathcal{A}+\mathcal{B}s+\mathcal{C}s^2\right) \end{aligned} \tag{C.45}$$

leading to 28 fit parameters.

C.2.6 Higher partial wave

For completeness we consider $(l, I) = (2, 2)$ and $(3, 1)$ partial waves, assuming no $\pi\pi$ interactions in these channels. The amplitudes are therefore given by the a^L terms alone which we expand o second order

$$a^{(2,2)} = \left(1 - \frac{4m_\pi^2}{s}\right)\left(\mathcal{A} + \mathcal{B}s + \mathcal{C}s^2\right) \tag{C.46}$$

$$a^{(3,1)} = \left(1 - \frac{4m_\pi^2}{s}\right)^{3/2}\left(\mathcal{A} + \mathcal{B}s + \mathcal{C}s^2\right) \tag{C.47}$$

leading to 72 real fit parameters.

C.2.7 Fit parameters

So far we have introduced 348 parameters in the partial waves which describe the photoproduction of either $\pi\pi$ or $K\bar{K}$ intermediate states. We have found than many of them, especially those multiplying higher powers of the invariant mass squared, s are small, thus in the final fits have reduced the number of terms in Eq. C.39, C.41, C.43, C.45, C.46, C.47. For $(l, I) = (0, 0)$ wave we kept only first order polynomial in the subtraction terms ($i.e$ set $\gamma = \delta = 0$) which leads to 40 real parameters for this wave. For $(l, I) = (1, 1)$ we set $\gamma = \delta = \epsilon = 0$) which reduces the number of parameters to 60. For $(l, I) = (2, 0)$ we eliminate $\gamma = \delta = \epsilon = 0$ leading to 60 real parameters. For $(l, I) = (0, 2)$ we eliminate $\gamma = \delta = 0$ leaving 20 real parameters. For $(l, I) = (2, 2)$ and $(l, I) = (3, 1)$ which do not involve final state interactions we keep set $\mathcal{C} =$ and reduce the number of parameters to 24 for each wave. The final total number of fit parameters is 228.

Bibliography

[1] J. Ballam *et al.*, Phys. Rev. D **7**, 3150 (1973).

[2] D. Aston *et al.*, Nucl. Phys. B **172**, 1 (1980).

[3] D. C. Fries *et al.*, Nucl. Phys. B **143**, 408 (1978).

[4] A. C. Irving and R. P. Worden, Phys. Rept. **34**, 117 (1977).

[5] L. Bibrzycki, L. Lesniak and A. P. Szczepaniak, Eur. Phys. J. C **34**, 335 (2004) [arXiv:hep-ph/0308267].

[6] C. R. Ji, R. Kaminski, L. Lesniak, A. Szczepaniak and R. Williams, Phys. Rev. C **58**, 1205 (1998) [arXiv:hep-ph/9710510].

[7] J. A. Oller, E. Oset and J. R. Pelaez, Phys. Rev. D **59**, 074001 (1999) [Erratum-ibid. D **60**, 099906 (1999)] [arXiv:hep-ph/9804209].

[8] S. U. Chung, Phys. Rev. D **56**, 7299 (1997).

[9] H. -J. Behrend *et al.*, Nucl. Phys. **B 144**, 22 (1978)

[10] D. P. Barber *et al.*, Z. Phys **C 12**, 1 (1982)

[11] Ł. Bibrzycki, L. Leśniak, A. P. Szczepaniak, Eur. Phys. J. **C 34**, 335 (2004)

[12] M. Battaglieri *et al.* (CLAS Collaboration), Phys. Rev. Lett. **87**, 172002 (2001)

[13] G. Grayer *et al.*, Nucl. Phys. **B 75**, 189 (1974)

[14] H. Becker *et al.*, Nucl. Phys. **B 151**, 46 (1979)

[15] C. Amsler *et al.* (Crystal Barrel Collaboration), Phys. Lett. **B 342**, 433, (1995)

[16] J. Ballam *et al.*, Phys. Rev **D 5**, 545 (1972)

[17] J. Ballam *et al.*, Phys. Rev **D 7**, 3150 (1973)

[18] R. Erbe *et al.*, Phys. Rev **175**, 1669 (1968)

[19] W. Struczinski *et al.*, Nucl. Phys. **B 108**, 45 (1976)

[20] P. Söding, Phys. Lett. **19**, 702 (1966)

[21] A. S. Krass, Phys. Rev. **159**, 1496 (1967)

[22] G. Kramer, J. L. Uretsky, Phys. Rev. **181**, 1918 (1969)

[23] J. Pumplin, Phys. Rev. **D 2**, 1859 (1970)

[24] T. Bauer, Phys. Rev. Lett. **25**, 485 (1970)

[25] C. Wu *et al.*, Eur. Phys. J. **A 23**, 317 (2005)

[26] A. Airapetian *et al.* (HERMES Collaboration), Phys. Lett. **B 599**, 212 (2004)

[27] C-R. Ji, R. Kamiński, L. Leśniak, A. Szczepaniak, R. Williams, Phys. Rev **C 58**, 1205 (1998)

[28] J. A. Gómez Tejedor, E. Oset, Nucl. Phys. **A 571**, 667 (1994)

[29] R. Kamiński, L. Leśniak, J. -P. Maillet, Phys. Rev. **D 50**, 3145 (1994)

[30] R. Kamiński, L. Leśniak, Phys. Rev. **C 51**, 2264 (1995)

[31] L. Leśniak, Acta. Phys. Pol. **B 27**, 1835 (1996)

[32] A. Furman, L. Leśniak, Phys. Lett. **B 538**, 266 (2002)

[33] ABBHHM Collaboration Phys. Rev. **175**, 1669 (1968).

[34] ZEUS Collaboration Eur. Phys. J. **C14**, 213 (2000).

[35] J. D. Jackson, Il Nuovo Cimento **34**,1644 (1964).

[36] M.Battaglieri *The reaction $\gamma p \to p\pi^+\pi^-$: data analysis procedure.*, CLAS-Note 2001-002.

[37] Y. Oh, H. Kim, and S. H. Lee Phys. Rev. **D69**, 014009 (2004).

[38] G. J. Feldman and R. D. Cousins, Phys. Rev. **D57**, 3873 (1998).

[39] See *http://www.jlab.org/Hall-B/secure/g11/mwill.*

[40] M.Battaglieri and R. De Vita, *The $\gamma p \to p\omega$ and $\gamma p \to K^+\Lambda(1115)$ differential and total cross sections: a check of the $g11$ reconstruction efficiency and photon flux normalization*, http://www.jlab.org/Hall-B/secure/g11/analysis_archive/analysis/genova/notes/g11xsec_note.ps.

[41] M.Battaglieri and R. De Vita, *The g11 fiducial cuts*, http://www.jlab.org/Hall-B/secure/g11/analysis_archive/analysis/genova/notes/g11fiducial_note.ps.

[42] J. D. Jackson, Il Nuovo Cimento **34**,1644 (1964).

[43] M.Battaglieri and R. De Vita, CLAS ANALYSIS-Note 03-XX

[44] J Barth *et al*, Phys. Lett. **B527** 123 (2003); M. Ostrick, Prog. Part. Nucl. Phys. **55**, 337 (2005).

[45] M. Ungaro *et al.*, G_{11} *data processing*, CLAS-NOTE 2005-014.

[46] M.Taiuti *et al.*, *About the Resolution in Θ^+ Mass Reconstruction A Montecarlo Simulation*, CLAS-Note 2004-010.

[47] M.Battaglieri and R. De Vita, G_{11} *hardware trigger and software reconstruction efficiency*, http://www.jlab.org/Hall-B/secure/g11/analysis_archive/analysis/genova/notes/g11trigger_note.ps.

[48] M.Williams XXX